UNIVERSITY OF CALIFORNIA,
IRVINE

Investigations of tropical rainfall biases and climate dynamics in the era of convection-permitting global climate models

DISSERTATION

submitted in partial satisfaction of the requirements
for the degree of

DOCTOR OF PHILOSOPHY

in Earth System Science

by

Sungduk Yu

Dissertation Committee:
Assistant Professor Michael S. Pritchard, Chair
Distinguished Professor Michael J. Prather
Professor François W. Primeau
Professor Jin-Yi Yu

2018

DEDICATION

I dedicate this dissertation to my parents and sister.

TABLE OF CONTENTS

LIST OF FIGURES

LIST OF TABLES

ACKNOWLEDGMENTS

First and foremost, I immensely thank my advisor, Mike Pritchard. Amongst great many things he has given to me, his constant encouragement was what enabled me to go through the long and winding road of the graduate school and to eventually become a Ph.D. I am very grateful to have someone who I can look up to as a great role model as my advisor for the past five years. I will forever be thankful for your mentorship and kindness.

I thank my committee members, Michael Prather, François Primeau, and Jin-Yi Yu who provided invaluable feedbacks and suggestions over the course of this dissertation research. They have always been available and spared their time out of the busy schedules, whenever I need to talk to them. I, in particular, acknowledge that a series of discussions with François Primeau considerably helped Chapter 4.

Chapter 2 was greatly improved by inputs from a handful of external researchers. I thank Brian Mapes for his original framing idea and Christopher Bretherton for much insightful feedback. In addition, I am grateful to Stefan Tulich, David Randall, and Robert Pincus for helpful discussions and to Gabriel Kooperman for providing me with precipitation analysis codes.

Chapter 3 was a collaboration research project with the University of Washington. I thank my collaborators, Christopher Bretherton and Matthew Woelfle, for insightful discussions over the entire research process. I also thank Steve Yeager for providing CESM datasets for hindcast initialization.

I thank many friends for heartfelt camaraderie as well as formal and informal academic discussions over the course of my time in Irvine: Paul Levine, Chris Terai, Hossein Parishani, Meg Fowler, Hongchen Qin, Galen Yacalis, Jian Sun, Yu-Chiao Liang, Liz Wiggins, Scot Parker, Lucas Baltzell, Rachel Smith, Baird Langenbrunner, Wenshan Wang, Guo Liu, Yi Yin, Moonsuk Her, Jihwan Myung, Chris McGuire, Shih-Wei Fang, Mike Muglia, and Eunkyu Park. Besides, I gratefully acknowledge the administrative support of Jaycee Chu and Elliot McCollum, without whom I would have struggled with the complicated paperworks required for graduation.

I must also thank my former advisor Brian White and former committee members, Carol Arnosti, John Bane, Roberto Camassa, Richard McLaughlin, Harvey Seim at the University of North Carolina at Chapel Hill (UNC), where I obtained my M.Sc. degree. They patiently nurtured my passion of science and eventually led me to pursue a Ph.D. I thank the former lab members at the UNC—especially, Shilpa Khatri, Elaine Monbureau, and Jennifer Prairie—for their help in and out of school.

Finally, I thank my parents for giving me the world and letting me freely explore.

Funding for this dissertation was provided by the Department of Energy under DE-SC0012152 and DE-SC0012548, the National Science Foundation (NSF) under AGS-1419518, and the Department of Earth System Science at the University of California, Irvine. Computational

resources were provided by the Extreme Science and Engineering Discovery Environment (Stampede and Stampede2) and by National Center for Atmospheric Research's Computational and Information Systems Laboratory (Yellowstone and Cheyenne), both sponsored by the NSF.

CURRICULUM VITAE

Sungduk Yu

EDUCATION

Doctor of Philosophy in Earth System Science **2018**
University of California, Irvine *Irvine, California*

- Advisor: Dr. Michael S. Pritchard
- Dissertation title: Investigations of tropical rainfall biases and climate dynamics in the era of convection-permitting global climate models

Master of Science in Earth System Science **2016**
University of California, Irvine *Irvine, California*

Master of Science in Marine Sciences **2013**
University of North Carolina at Chapel Hill *Chapel Hill, North Carolina*

- Advisor: Dr. Brian L. White
- Thesis title: Settling of porous spheres, as a proxy for marine snow, through density stratification

Bachelor of Science in Mechanical Engineering **2006**
Bachelor of Science in Life Science
Pohang University of Science and Technology *Pohang, Korea*

PUBLICATIONS

Yu, S. and M.S. Pritchard (2018). Is oceanic buffering of forced ITCZ shifts controlled by an underappreciated Atlantic meridional overturning circulation pathway? Submitted to *Journal of Climate*.

Woelfle, M. D., **S. Yu**, C. S. Bretherton, M. S. Pritchard (2018). Sensitivity of Coupled Tropical Pacific Model Biases to Convective Parameterization in CESM1, *Journal of Advances in Modeling Earth Systems*, 10, 126–144.

Elliott, E., **S. Yu**, G. J. Kooperman, H. Morrison, M. Wang, and M. S. Pritchard (2016). Sensitivity of summer ensembles of fledgling superparameterized US mesoscale convective systems to cloud resolving model microphysics and grid configuration, *Journal of Advances in Modeling Earth Systems*, 8, 634–649.

Yu, S. and M. S. Pritchard (2015). The effect of large-scale model time step and multi-scale coupling frequency on cloud climatology, vertical structure, and rainfall extremes in a superparameterized GCM, *Journal of Advances in Modeling Earth Systems*, 7, 1977–1996.

Camassa, R., S. Khatri, R. M. McLaughlin, J. C. Prairie, B. L. White, and **S. Yu** (2013). Retention and entrainment effects: Experiments and theory for porous spheres settling in sharply stratified fluids, *Physics of Fluids*, 25(8), 081701.

Prairie J. C., K. Ziervogel, C. Arnosti, R. Camassa, C. Falcon, S. Khatri, R. McLaughlin, B. L. White, and **S. Yu** (2013). Delayed settling of marine snow at sharp density transitions driven by fluid entrainment and diffusion-limited retention, *Marine Ecology Progress Series*, 487, 185–199.

ORAL PRESENTATION

Yu, S., M. S. Pritchard, M. Woelfle, and C. S. Bretherton (2017). Robustness of Double ITCZ Biases to the Use of Explicit Convection in the Superparameterized Community Earth System Model. *The 97th American Meteorological Society (AMS) Annual Meeting*, Seattle, WA.

Yu, S. and M. S. Pritchard (2016). More frequent GCM-CRM coupling leads to more bottom-heavy convection. *The 20th Center for Multiscale Modeling of Atmospheric Processes (CMMAP) Team meeting*, Boulder, CO.

Yu, S. and M. S. Pritchard (2015). Effect of Scale Coupling Frequency on Simulated Climatology in the Uncoupled SPCAM 3.0. *The 18th CMMAP Team Meeting*, San Diego, CA.

POSTER PRESENTATION

Yu, S. and M. S. Pritchard (2017). Thoughts on why in CESM a more poleward TOA energy imbalance favors more ocean-centric energy transport and weaker ITCZ shift responses. *2017 American Geophysical Union (AGU) Annual Meeting*, New Orleans, LA.

Yu, S. and M. S. Pritchard (2017). Atmospheric vs. oceanic meridional energy transport partitioning response to zonally-confined top-of-atmosphere solar forcing in a fully coupled earth system model. *2017 Radiation and Climate Gordon Research Conference*, Lewiston, ME.

Yu, S. and M. S. Pritchard (2017). ITCZ shift dynamics may be muted by a hemispheric rearrangement of surface fluxes that thermodynamically promote the ocean's efficiency to mediate asymmetric top-of-atmosphere forcing. *The 21st Conference on Atmospheric and Oceanic Fluid Dynamics*, Portland, Or.

Yu, S. and M. S. Pritchard (2016). Oceanic versus atmospheric meridional energy transport response to interhemispherically-asymmetric solar forcing in the CESM. *2016 AGU Fall Meeting*, San Francisco, CA.

Yu, S., M. S. Pritchard, and C. S. Bretherton (2016). Sensitivities of the double-ITCZ

rainfall bias in the Superparameterized Community Earth System Model. *The 96th AMS Annual Meeting*, New Orleans, LA.

Yu, S. and M. S. Pritchard (2015). Effects of scale coupling frequency on convective organization in the superparameterized Community Atmospehre Model. *2015 AGU Fall Meeting*, San Francisco, CA.

Yu, S. and M. S. Pritchard (2015). Response of the double ITCZ / cold tongue bias to varying the orientation and extent of embedded cloud resolving models in the SuperParameterized CESM. *Workshop on Monsoons & ITCZ: the annual cycle in the Holocene and the future*, New York City, NY.

Yu, S. and M. S. Pritchard (2015). The double-ITCZ bias in the Superparameterized Community Earth System Model and its sensitivities to the embedded cloud resolving model configurations. *The 3rd EaSM PI Meeting*, Bethesda, DC.

Yu, S. and M. S. Pritchard (2014). Effect of Scale Coupling Frequency on Simulated Climatology in the Uncoupled Superparameterized Community Atmosphere Model v. 3.0. *2014 AGU Fall Meeting*, San Francisco, CA.

Yu, S., and M. S. Pritchard (2014). Effect of Scale Coupling Frequency on Simulated Climatology in the Uncoupled SPCAM3. *The 17th CMMAP Team Meeting*, Ft. Collins, CO.

Yu, S., B. L. White, C Arnosti, R Camassa, R. M. McLaughlin, and J. C. Prairie (2012). Settling of Porous Particle Clouds in Stratification: a Proxy for Marine Snow. *2012 Ocean Science Meeting*, Salt Lake City, UT.

TEACHING EXPERIENCE

Teaching Assistant **2014–2017**
University of California, Irvine *Irvine, California*

- ESS116 Data Analysis (2014 Fall)
- ESS15 Climate Change (2015 Winter)
- ESS7 Physical Geology (2015 Spring)
- ESS19 Introduction to Modeling the Earth System (2016 Winter)
- ESS27 Sustainable Ocean (2016 Spring)
- ESS55 Earth's Atmosphere (2017 Spring)

Teaching Assistant **2010–2011**
University of North Carolina at Chapel Hill *Chapel Hill, North Carolina*

- MASC101 Marine Environment (2010 Fall)
- MASC401 Oceanography (2011 Spring)

OTHER EXPERIENCE

Les Houches Summer School on Fundamental Aspects of Turbulent Flows in Climate Dynamics (July–August, 2017), *Ecole d'Ete de Physique Theorique*, Les Houches, France.

Dynamical Core Model Intercomparision Project Summer School 2016 (June, 2016), *National Center for Atmospheric Research*, Boulder, CO.

2015 Community Earth System Model Tutorial Workshop (August, 2015), *National Center for Atmospheric Research*, Boulder, CO.

The 1st WCRP Summer School on Climate Model Development: Atmospheric Moist Processes (June, 2015), *Max Planck Institute for Meteorology*, Hamburg, Germany.

Research cruise surveying the Mid-Atlantic Bight, *R/V Cape Hatteras* (November, 2010).

ABSTRACT OF THE DISSERTATION

Investigations of tropical rainfall biases and climate dynamics in the era of convection-permitting global climate models

By

Sungduk Yu

Doctor of Philosophy in Earth System Science

University of California, Irvine, 2018

Assistant Professor Michael S. Pritchard, Chair

Tropical precipitation in modern global climate models (GCMs) still shows large errors in both spatial and temporal patterns, despite notable improvement of GCMs over past decades. As tropical precipitation biases are linked to large scale circulation errors and in turn have global impacts in simulated climate, tropical precipitation bias is one of the primary issues to be tackled to improve the accuracy of GCM output. This dissertation addresses key issues in the underlying model dynamics and physics responsible for tropical precipitation biases in modern, state-of-art GCMs.

The first of the three research projects presented in this dissertation systematically tests the time step sensitivity of a superparameterized (SP) GCM to better understand the physical essence of superparameterized convection and its impact on global climatology. The time step in an SPGCM dictates the frequency of information exchange between two scales (between the GCM and the cloud resolving model (CRM) embedded in each grid cell), and, accordingly, a different time step artificially imposes a constraint on model behavior. In an SP version of the Community Atmosphere Model 3.0, several important sensitivities in the tropical climatology are identified, e.g. a faster scale coupling causes weaker cloud forcing,

boosted extreme precipitation frequency, more bottom-heavy updraft profiles, and weaker temperature gradients. These sensitivities are distinct from the time step sensitivities of conventionally parameterized GCMs and have implications for understanding emergent behaviors of multiscale deep convective organization in superparameterized GCMs.

The second research project examines the impact of superparameterization on the initial growth of the double ITCZ (Intertropical Convergence Zone) bias in a dynamic ocean coupled GCM, with the initial intention to test if superparameterization can be a useful tool to mitigate this long-standing model problem by avoiding convective parameterizations that have been known as one of major double ITCZ bias sources. In an SP version of Community Earth System Model (CESM) 1.1, a fast bias growth, e.g. days for precipitation biases and weeks for sea surface temperature biases (also known as the cold tongue SST bias), is observed and validates our novel approach using short, ensemble hindcast simulations. The SP simulations show weaker double ITCZ biases than non-SP simulations, but this improvement is due to non-physical causes. A key discovery is that the historical neglect of convective momentum transport in SP-CESM causes unrealistically strong zonal wind shear near the surface that effectively suppresses the increase of zonal surface wind stress even when stronger overlying easterlies are present. The results highlight a less-appreciated role of convective momentum transport as a potential double ITCZ bias source, providing a new perspective to ITCZ dynamics and also suggesting future model development strategies.

The third research project focuses on a marquee issue of modern tropical climate dynamics by exploring how oceanic circulation response buffers forced ITCZ shift when a top-of-atmosphere solar flux perturbation is present at the different latitudinal bands. Particular attention is paid to heat transport associated with Atlantic meridional overturning circulation (AMOC) that, unlike subtropical cell, does not have mechanical constraints coupled to Hadley circulation allowing potentially more efficient ITCZ shift buffering. A set of 200-year simulations using CESM 1.2 shows that the heat transport partitioning becomes more ocean

centric as the solar forcing is located at higher latitudes and that such sensitivity is indeed driven by the AMOC responses. On the other hand, a previously identified STC (subtropical cell) damping mechanism does not respond sensitively to the solar forcing locations, as a result of compensating circulation strength and depth responses. The findings demand the inclusion of the previously underappreciated AMOC heat transport to the current ITCZ migration framework to fully capture the atmosphere-ocean coupling. Besides, the results have some practical implication in GCM development strategy suggesting fixing tropical bias would be more effective to alleviate tropical precipitation biases in GCMs than fixing extratropical biases.

Chapter 1

Introduction and Synthesis

Without precipitation, the earth would have been a much different planet. All terrestrial life, including human life, relies on precipitation in a certain, but indispensable way. Even marine organisms indirectly depend on it since river runoff is an important source of biogeochemical cycles of the ocean. Hence, understanding the physical process behind precipitation and being able to simulate the future changes of precipitation using computer models has critical implications for socioeconomic and ecological well-being, especially in the context of anthropogenic global warming. Besides, precipitation itself is a great metric to measure the advance of GCMs since it involves multiple processes at vastly different scales, from microphysics (10^{-3} m) to midlatitude frontal system (10^{6} m).

The changes in global precipitation due to a warming climate have been predicted by theories (*Allen and Ingram*, 2002; *Held and Soden*, 2006; *O'Gorman et al.*, 2012) and have also been observed (*Wentz et al.*, 2007; *Zhang et al.*, 2007a; *Allan and Soden*, 2008). However, the capability of global climate models to simulate precipitation remains somewhat limited, especially in the tropics (figure 1.1), eroding the creditability of the global climate model (GCM) projected rainfall changes.

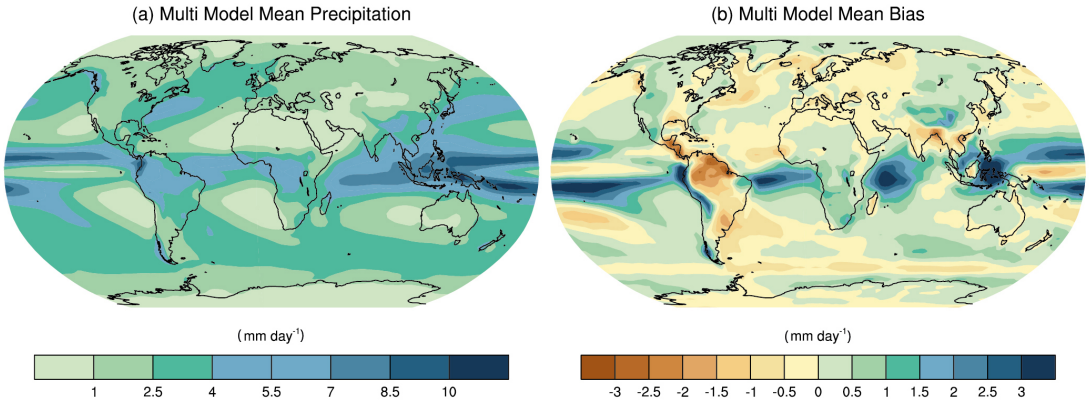

Figure 1.1: Modern-day annual-mean precipitation. (a) the multi model mean (MMM) of the CMIP5 historial experiment and (b) bias against the Global Precipitation Climatology Project (GPCP) observation dataset (*Adler et al.*, 2003). Averaging period is 1980–2005. Images are adapted from figure 9.4 of the 5th Intergovernmental Panel on Climate Change (IPCC) Assessment Report (*IPCC*, 2013).

One infamous example of tropical precipitation bias existing in virtually all GCMs is that the intertropical convergence zone (ITCZ)—a band of intense precipitation and cloud cover encircling the tropics and one of the most pronounced features of the earth climate system—has one extra band to the south of the equator which does not exist in the observation (figure 1.1b). Such bias is also known as the *double ITCZ bias*. Because ITCZ is so sharp, a small migration can cause a large impact on local precipitation. Furthermore, the impact is not confined to the Tropics. Recent studies showed that the position of the ITCZ can cause changes in the frequency of tropical cyclone occurrence (*Dunstone et al.*, 2013; *Merlis et al.*, 2013) and in the locations of the mid-latitude jets (*Ceppi et al.*, 2013; *Cvijanovic et al.*, 2013). Even after two decades since the identification of the double ITCZ bias (*Mechoso et al.*, 1995), it remains as major challenge for modern (CMIP3 and 5 generation) GCMs (*Zhang et al.*, 2015). Accordingly, better understanding the physical mechanism of the model biases is of first-order importance to reliably project tropical climate change.

This dissertation will examine the different aspects of the tropical precipitation bias present in modern GCMs so as to learn about the model dynamics and physics underlying such tropical biases. The following section overviews the three research projects that comprise

this dissertation.

1.1 Research overview

This dissertation includes three distinct studies (Chapters 2–4), which are all under the umbrella of the tropical precipitation problem. In this section, the motivation and goal of each study are outlined.

1.1.1 Chapter 2 overview

Climate model simulations are numerically non-convergent in the sense that a handful of key climate variables can be sensitive to a GCM time step. For example, in the Community Atmosphere Model (CAM), the partitioning of precipitation paths between large-scale processes versus cumulus parameterization—which is interconnected to the different aspects of tropical climate in a model (*Lin et al.*, 2013)—is sensitive to a GCM time step (*Mishra et al.*, 2008a; *Williamson*, 2008; *Mishra and Sahany*, 2011a). The geographic structure of zonal mean precipitation is also sensitive to a GCM time step, even switching between single and double intertropical convergence zone states (*Mishra et al.*, 2008a; *Williamson*, 2008; *Li et al.*, 2011). Furthermore, these studies also found the tropical-mean precipitation is also somewhat sensitive to a GCM time step (e.g. higher mean precipitation rate with a shorter time step).

Understanding these issues is important for intelligently interpreting GCM climate projections. *Williamson* (2013) argued that many of these sensitivities are a manifestation of deep and shallow convective parameterizations failing to effectively remove moist instability by vertical redistribution and associated condensation—especially when the adjustment timescales assumed in convective parameterizations are longer than a GCM time step.

Consistent with this view, they showed convective precipitation (precipitation produced by convective parameterization scheme) decreases with a reduced GCM time step in a high-resolution aqua-planet version of CAM4. In other words, when convective parameterizations do not have sufficient time to remove a substantial amount of moist instability in between GCM time steps, a feedback with the large-scale circulation may occur, either because of differences in the latent heating profile leading to different circulations and increased moisture convergence (and gross moist stability) or because it may be easier for the large-scale precipitation scheme to convert moisture convergence to precipitation than for a convection scheme (or is realistic in a convecting environment). These sorts of mechanisms can result in coarse grid-scale overturning, generating heavy precipitation events, and so-called "grid-point storms"—unrealistically intense, short-lived precipitation events occurring at the GCM grid scale. This, in turn, limits the usefulness of modern GCM for predicting extreme rain rate changes with global warming (*Pendergrass and Hartmann*, 2014a).

As climate simulations begin to enter the convection-permitting era, it is essential to know whether superparameterized (SP) GCMs—in which cumulus parameterizations are replaced with cyclic two-dimensional cloud resolving models (CRMs) in each grid column—exhibit similarly important sensitivities or artificial behaviors controlled by the time step of the exterior model. Although the answer is not apparent, one would expect insensitivity to a GCM time step might be expected in SPGCMs—due to the absence of rigid assumptions on convective instability depletion timescales that most GCMs with cumulus parameterizations have. On the other hand, there are also logical reasons to think the GCM time step may matter to SPGCM simulations: after all, the scale separation between GCM and CRM that is intrinsic to SP models is more artificial than natural, and information is only allowed to be exchanged between the two resolved scales at each GCM time step. From this view, the global model time step may have an even bigger impact in an SPGCM than it does in a conventional GCM.

Chapter 2 addresses systematic testing needed to better understand the physical essence of superparameterized convection in SPGCMs by examining their time step sensitivity. Via a set of SP-CAM simulations with four different time steps, I will attempt to test the above-mentioned ideas of the time step sensitivity (or insensitivity). A narrow CRM domain (8×1 columns) will be used for computational efficiency and for testing a hypothesis that initially motivated this study: a faster scale coupling would eliminate 'convective throttling' (i.e. artificially limited mixing efficiency of deep convection) due to a limited CRM domain (*Pritchard et al.*, 2014). The outcome of this study will reveal a new aspect of the SP model physics and also provide a perspective to interpret the previous SP simulation results—in terms of scale coupling frequency—and design experiment using SP models in the future.

Objectives

Time step (scale coupling frequency) sensitivity of a superparameterized GCM will be systematically assessed in order to learn about emergent multiscale convection physics in a superparameterized GCM. Specific questions include:

- Are SPGCM simulations sensitive to their time steps and their associated scale coupling frequencies?
- If so, are there climatologically important effects of the choice of GCM time step in SPGCMs that should inform their use and interpretation?
- What are the underlying model physics—unique to superparameterized GCMs—that are responsible for the time step sensitivity? Do these findings have any implications for the current understanding of tropical dynamics that are new in the era of global cloud resolving simulation?

1.1.2 Chapter 3 overview

Most modern ocean-atmosphere coupled global climate models (GCMs) produce a spurious precipitation band to the south of the equator in the Pacific (and also in the Atlantic for some models) in their annual mean precipitation. It is usually associated with sea surface temperature (SST) errors (e.g. too cold temperature and excessively westward elongation of the equatorial SST cold tongue). These errors are together called *the double ITCZ bias*, which have posed a major challenge to climate modeling since they were identified about two decades ago (*Mechoso et al.*, 1995). A recent paper showed that no improvement in the double ITCZ problem has been made in CMIP5 models compared to CMIP3 models (*Zhang et al.*, 2015). Biases in precipitation and SST working with circulation rapidly develop within a month to a few years (*Liu et al.*, 2012; *Song and Mapes*, 2012), and they eventually overwhelm physically correct signals and deteriorate the credibility of climate simulations, especially in the tropics. Accordingly, a better understanding of the physical mechanisms underlying this model problem is of immediate importance to make reliable projections of tropical climate change.

While there is no complete theory on the causes and underlying physical mechanisms that lead to the double-ITCZ biases, traditional cumulus parameterizations have been implicated as one of the more likely sources of such bias. For example, modifications to convective parameterizations can induce transitions from single to double ITCZ states in idealized atmospheric GCMs (*Möbis and Stevens*, 2012). Several studies have revealed the double ITCZ bias sensitivity to convective parameterization schemes, e.g. rain evaporation parameter (*Bacmeister et al.*, 2006), SST threshold to trigger deep convection (*Bellucci et al.*, 2010), entrainment parameter (*Chikira*, 2010; *Hirota et al.*, 2011; *Oueslati and Bellon*, 2013). However, these attempts have yielded only limited improvements suggesting that the double ITCZ problem may be an unavoidable consequence of all convective parameterization schemes and/or that leading bias sources originate from Earth System components other

than convective parameterization schemes.

In this context, it is interesting to consider whether avoiding parameterization of moist convection might alter the nature of the double ITCZ bias. While one may predict that SP would improve the double ITCZ bias because of explicitly resolved deep convection, previous studies suggest the answer may not be so straightforward. An SP version of a legacy NCAR GCM (Community Climate System Model) showed notable improvement in the double ITCZ bias during summer and winter seasons (*Stan et al.*, 2010), but a recent study using an SP version of up-to-date NCAR GCM (Community Earth System Model) showed only marginal reduction of the double ITCZ biases in the annual mean precipitation (*Kooperman et al.*, 2016). Hence, the systematic assessment of the effect of SP on the double ITCZ problem is clearly required to test if SP can be a useful tool to mitigate this long-standing model problem.

Chapter 3 contains a systematic assessment of the initial growth of the double ITCZ bias in the CESM and how superparameterization alters the bias. Based on *Song and Mapes* (2012), who showed a fast development of precipitation bias (∼days) and SST bias (∼months), initial transient responses will be analyzed using short hindcast simulations rather than steady-state responses that most previous studies focused on. Upon successful validation of fast bias development, I will test how a radically different parameterization (superparameterization) influences the double ITCZ bias in terms of both precipitation and SST. The results from the superparameterized simulations will be a valuable addition to the previous studies focused on the role of convective parameterization to the double ITCZ bias, and, practically speaking, the short ensemble hindcast approach will provide a new, efficient way to study the double ITCZ bias in the future.

Objectives

The details of the initial double-ITCZ bias evolution in ensemble, hindcast experiments will be examined using fully-coupled superparameterized (SP) GCMs in order to highlight the role of explicit deep convection. In addition, a new experimental strategy to approach the double ITCZ problem (short, ensemble hindcast simulations) will be tested. The specific questions include:

- How quickly does the double ITCZ bias become established in the fully-coupled CESM? Is a set of short, ensemble hindcast simulations a viable way to study the double ITCZ bias?
- Does SP act to improve the double ITCZ problem? What is the physical mechanism underlying the improvement (i.e. atmosphere-ocean process chain), and to what extent are compensating errors involved?
- Does confronting effects of explicit convection on the ITCZ reveal any underappreciated pathways in its underlying climate dynamics?

1.1.3 Chapter 4 overview

Although traditionally local (tropical) processes have been examined to better understand tropical precipitation biases (e.g. Chapter 3), more recent studies suggest that extratropical biases can cause tropical precipitation biases. These studies were inspired by paleoclimate records that show a synchronization of tropical precipitation and interhemispheric temperature changes. For example, warmer temperature anomalies over Greenland are correlated to the increased precipitation of the Cariaco Basin (located at about 10°N) during the Last Glacial Period and Holocene (*Chiang and Friedman*, 2012; *Schneider et al.*, 2014). Since

Chiang et al. (2003) and *Chiang and Bitz* (2005) showed that the high latitude LGM boundary condition (imposed as land ice cover) can shift the ITCZ southward, such extratropical influence to tropical precipitation has been demonstrated with different climate models and with various hemispherically-asymmetric heating sources, e.g. radiative forcing (including carbon dioxide, solar flux, tropospheric ozone, black carbon, sulfate aerosols) (e.g. *Yoshimori and Broccoli*, 2008; *Frierson and Hwang*, 2012; *Hwang et al.*, 2013; *Haywood et al.*, 2016), vegetation change in boreal forests (e.g. *Swann et al.*, 2012; *MP et al.*, 2012; *Kang et al.*, 2015), and Southern Ocean heat uptake (e.g. *Hwang et al.*, 2017).

Building on the earlier studies suggesting potential atmospheric mechanisms that connect extratropical forcing to tropical responses (*Chiang and Bitz*, 2005; *Broccoli et al.*, 2006; *Yoshimori and Broccoli*, 2008), *Kang et al.* (2009, 2008) provided a comprehensive, theoretical explanation on how a such extratropics-to-tropics teleconnection operates. Based on the so-called energetics framework, the ITCZ must move towards a differentially heated hemisphere in order to transport heat to a differentially cooled hemisphere since the cross-equatorial atmospheric heat transport follows the direction of the upper branch of the Hadley cell at the equator (i.e., the converging lower branch contains less energy than the diverging upper branch). This assumes that (a) the heat transport by transient and stationary eddies is much weaker than that by the mean meridional circulation (namely the Hadley Circulation), and (b) the gross moist stability (*Neelin et al.*, 1987), which is a measure of heat transport efficiency of unit circulation strength, does not change much. Observational analysis indicated that the first assumption is plausible (*Oort*, 1971; *Trenberth and Stepaniak*, 2003); however, the second assumption might be broken in a special cases, e.g. CO_2 forcing (*Hill et al.*, 2015; *Seo et al.*, 2017) or different boundary conditions (*Roberts et al.*, 2016).

However, recent studies using dynamic ocean coupled global climate models (GCMs) have questioned the tightness of the relationship between the ITCZ shift and hemispherically asymmetric forcing. The ITCZ does not always shift sensitively in response to hemispheri-

cally asymmetric extratropical forcing, but rather cross-equatorial oceanic energy transport can provide a dominant balance in fully-coupled GCMs (e.g. brightening the Southern Ocean by increasing low clouds or increasing albedo and darkening the tropics by altering low clouds or decreasing albedo, see *Kay et al.* (2016); *Hawcroft et al.* (2016)). Such responses which are not predicted from the energetics framework are due to an extra degree of freedom in the cross-equatorial heat transport response—namely, oceanic heat transport—in coupled GCMs. A popular explanation of damped ITCZ responses in fully coupled simulations is that an anomalous Hadley cell should cause an anomalous subtropical cell (STC; a shallow overturning cell confined within subtropics), since the atmospheric and oceanic overturning circulations are mechanically coupled via surface wind stresses that causes Ekman drift in opposite directions with respect to each other (*Held*, 2001; *Schneider et al.*, 2014; *Green and Marshall*, 2017). However, the role of the Atlantic meridional overturning circulation (AMOC) in the ITCZ damping is rather unclear, despite the fact that the AMOC heat transport can displace the position of ITCZ—for example, the northward heat transport of AMOC is the main contributor to making the zonal mean ITCZ position north of equator (*Frierson et al.*, 2013; *Marshall et al.*, 2014), and a slowdown of AMOC in response to artificial freshening of the high-latitude North Atlantic can shift ITCZ (*Vellinga and Wood*, 2002; *Zhang and Delworth*, 2005).

Chapter 4 explores the less appreciated role of AMOC in the ITCZ positioning dynamics using a state-of-art GCM with a fully dynamic ocean component. I hypothesize that AMOC responses may provide a more efficient ITCZ damping than STC responses since they lack a mechanical constraint such as the Ekman coupling that limits STC responses. To probe this hypothesis, a set of simulations is conducted with a top-of-atmosphere (TOA) solar flux perturbation at four different latitudinal bands occupying an equal area. Particular attention will be given to the comparison between AMOC and STC responses to contrast ITCZ shift buffering mechanisms between the two distinct overturning circulations. The Outcome of this study will advance our current understanding of the ITCZ positioning dynamics by

explicitly showing the role of AMOC and may suggest strategies for GCM development and possibly geoengineering, because the idealized TOA forcing can be interpreted as regionally confined GCM bias or a type of geoengineering (e.g. regionally-confined solar radiation management).

Objectives

The role of AMOC as a potential ITCZ shift buffering mechanism will be tested through a set of state-of-art, fully-coupled GCM simulations with a perturbed top-of-atmosphere solar flux at different latitudes. Detailed questions include:

- How does the partitioning between atmospheric and oceanic heat transports respond to the solar forcing latitude in radiatively forced ITCZ migration experiments? Do Atlantic and Pacific oceanic heat transport responses show different sensitivities to the forcing locations?
- How do the top-of-atmosphere radiative feedbacks to the solar perturbation change with the forcing latitude? Are there any dominant feedback components controlling total heat transport responses?
- If AMOC effectively buffers ITCZ shift responses, what is the relevant timescale for its buffering mechanism?

1.2 Organization

Chapters 2, 3, and 4 are the main research chapters that are outlined in the previous section. Each is based on a manuscript that has been either published or submitted to a peer-reviewed

journal of which publication information is shown on the first page of each chapter. Chapter 5 concludes with brief summaries and suggested future works.

Chapter 2

The effect of large-scale model timestep and multiscale coupling frequency on cloud climatology, vertical structure, and rainfall extremes in a superparameterized GCM

As appears in:

Yu, S., and M. S. Pritchard (2015), The effect of large-scale model time step and multi-scale coupling frequency on cloud climatology, vertical structure, and rainfall extremes in a superparameterized GCM, Journal of Advances in Modeling Earth Systems, 7, 1977–1996, doi:10.1002/2015MS000493.

Abstract

The effect of global climate model (GCM) time step—which also controls how frequently global and embedded cloud resolving scales are coupled—is examined in the Superparameterized Community Atmosphere Model ver 3.0. Systematic bias reductions of time-mean shortwave cloud forcing ($\sim$10 W/m^2) and longwave cloud forcing ($\sim$5 W/m^2) occur as scale coupling frequency increases, but with systematically increasing rainfall variance and extremes throughout the tropics. An overarching change in the vertical structure of deep tropical convection, favoring more bottom-heavy deep convection as a global model time step is reduced may help orchestrate these responses. The weak temperature gradient approximation is more faithfully satisfied when a high scale coupling frequency (a short global model time step) is used. These findings are distinct from the global model time step sensitivities of conventionally parameterized GCMs and have implications for understanding emergent behaviors of multiscale deep convective organization in superparameterized GCMs. The results may also be useful for helping to tune them.

2.1 Introduction

It is well known that in global climate models (GCMs) using cumulus parameterizations, key aspects of the simulation performance can depend sensitively on the GCM time step. The partitioning between precipitation determined by large-scale dynamics versus cumulus parameterization is sensitive to model time step, with implications for rainfall extremes (*Williamson*, 2008; *Mishra et al.*, 2008b; *Mishra and Sahany*, 2011b). In addition, the geographic structure of zonal mean precipitation structures can also be sensitive to the GCM time step, even switching between either single- or double- intertropical convergence zone states depending on the GCM time step and dynamical core used in aqua-planet simulations

with the Community Atmosphere Model ver 3.0 (CAM3) (*Williamson*, 2008; *Mishra et al.*, 2008b; *Li et al.*, 2011) and its preceding version (*Williamson and Olson*, 2003). These studies also found tropical mean precipitation can also be somewhat sensitive to the GCM time step with mean precipitation rate increasing with a shorter time step.

Williamson (2013) argued many of these sensitivities may be a manifestation of deep and shallow convective parameterization schemes failing to effectively eliminate moist instability by vertical redistribution and associated condensation when the adjustment timescales assumed in convective parameterizations are longer than a GCM time step. Consistent with this view, they showed convective precipitation decreases with a reduced GCM time step in a high-resolution aqua-planet version of CAM4. One way to think of their physical idea is that when convective parameterizations do not have enough time to remove a substantial amount of moist instability in between GCM time steps, a feedback with the large-scale circulation may occur, either because of differences in the latent heating profile leading to different circulations and increased moisture convergence (and gross moist stability) or because it may be easier for the large-scale precipitation scheme to convert moisture convergence to precipitation than for a convection scheme (or is realistic in a convecting environment). These sorts of mechanisms can result in coarse grid-scale overturning, generating heavy precipitation events and so-called 'grid-point storms'—unrealistically intense, short-lived precipitation events occurring at the GCM grid scale.

It is unknown whether superparameterized (SP) GCMs—in which cumulus paramterizations are replaced with cyclic 2-dimensional cloud resolving models (CRMs) in each grid column—exhibit similar sensitivities to the time step of the exterior model, namely the GCM. This is the problem we will address.

As a null hypothesis (H0) it is logical to predict that the exterior model time step sensitivities of SPGCMs should be much less striking than normal GCMs since SPGCMs do not rely on rigid assumptions about convective instability depletion timescales, unlike most conventional

cumulus parameterizations. Thus theoretically, convective instabilities exposed to embedded CRMs should always efficiently be removed as they develop, leading to expectations of reduced grid-point storm sensitivities in SPGCMs [D. Randall, personal communication]. Hypothesis H0 predicts SPGCMs should be mostly *insensitive* to large-scale model time step, unlike normal GCMs.

However, there are also logical reasons to think the global model time step may matter to SPGCM simulations in new and important ways. After all, the scale separation between GCM and CRM intrinsic to SP models is more artificial than natural, and information is only allowed to be exchanged between the two resolved scales at each GCM time step. That is, the global model time step can actually represent more in a SPGCM than it does in a conventional GCM—it is also the primary control on the *scale coupling frequency*, f_{scale}. In this capacity, the global model time step may affect the simulations of SPGCMs in ways that are unfamiliar, and to emphasize this point we will refer to the global model time step as f_{scale} in subsequent discussion.

Specifically, we propose an alternative working hypothesis (H1; B. Mapes, personal communication) based on recent ideas about *convective throttling* in SPGCM simulations by *Pritchard et al.* (2014) (PBD14 hereafter). PBD14 argued that the number of grid columns in a SPGCM's embedded CRMs may artificially limit the efficiency of deep convective mixing in a way that has important consequences for simulated cloud climatology, such as overly strong shortwave cloud forcing from too dense liquid clouds when small CRMs are used. This view is consistent with a variety of quasi-linear biases observed to develop as the horizontal extent and number of grid columns in embedded CRMs are reduced.

The implications of these physics might imply scale-coupling sensitivities in SPGCMs. Since the convective throttling effect is purely local and internal to the embedded CRM in each GCM grid cell, it is natural to wonder if it may be buffered through exposure to large-scale dynamics—which have the capacity to remove CRM-extent-throttled instability through

interactions with large-scale wave modes and large-scale advection at the GCM scale. Thus our alternative convective throttling hypothesis (H1) predicts more frequent scaling coupling should unwind the mean state cloud biases that develop with reduced CRM extent. That is, hypothesis H1 predicts SPGCMs should be *sensitive* to decreased global model time steps in a fashion that is reverse to the sensitivities previously documented as a function of CRM extent in PBD14.

Beyond H0 and H1, there are other exploratory hypotheses that could be conceived for how—especially through its effect on scale coupling frequency—the GCM model time step might impact the vertical diabatic heating profile or mean state climatology of clouds in super-parameterized models. In short, it is not obvious how to predict what the impact of scale coupling on SP simulations should be, or how default GCM model time step settings may have constrained previous SP simulations. Clearly, systematic testing is needed— primarily as a strategy to inform better understanding of the physical essence of emergent multi-scale organized convection physics in SPGCMs. A secondary practical goal is to see if the scale coupling frequency is a useful tuning knob in SPGCMs that might help improve the fidelity of climate simulations with explicit convection.

This chapter documents the effects of global model time step (and consequently scale coupling frequency f_{scale}) on the simulated climate in the Superparameterized Community Atmospheric Model 3. Several interesting sensitivities, many of which are monotonic to f_{scale}, are discovered. Section 2.2 describes the model and the experimental designs. Section 2.3 shows the major findings. Section 2.4 contains further discussion and some ideas for future work. Section 2.5 concludes.

2.2 Methodology

2.2.1 Model description

The Superparameterized Community Atmospheric Model ver 3.0 (SPCAM3) is used for all simulations in this study. Its exterior large-scale model is a version of Community Atmospheric Model 3.0 that uses a semi-Lagrangian dynamical core with T42 spectral resolution and 30 vertical levels. Over eight thousand 2-D CRMs with 4km horizontal grid spacing are embedded to replace deep and shallow cloud and boundary layer turbulence parameterizations in each grid cell (superparameterization; *Grabowski and Smolarkiewicz* (1999); *Grabowski* (2001)). The embedded CRM is a legacy version of the System of Atmospheric Model (*Khairoutdinov and Randall*, 2003). This essence of this version of SPCAM3 has been widely used by *Khairoutdinov et al.* (2005), *Khairoutdinov et al.* (2008), *Benedict and Randall* (2009), and *Thayer-Calder and Randall* (2009). We use a somewhat unusual 'micro-CRM (8×1 column)' configuration of superparameterization used by PBD14, in which the micro-CRM is one quarter the size of the conventional CRM setup of 32×1 columns. This is chosen for two practical reasons. First, it usefully enforces a baseline model configuration that is already known to be highly "throttled", with results that can be directly compared to that study. We view this as helpful for testing the expectation of H1: that increasing f_{scale} could decrease the effect of throttled deep convection due to a limited CRM domain extent. Second, it is also a useful model configuration for computational efficiency, enabling $4\times$ faster simulations in a computationally demanding GCM. The specific code version of SPCAM3 that was used for integrations is archived by the Center for Multiscale Modeling for Atmospheric Processes at: https://svn.sdsc.edu/repo/cmmap/cam3_sp/branches/pritchard (rev. 304).

2.2.2 Experimental design

Our experiment includes four cases with different values of the host GCM (CAM3) model time step, and hence f_{scale}. The control case uses a GCM time step of 1800 seconds, which has been a convention of SPCAM3 simulations at T42 resolution (e.g. *Khairoutdinov et al.*, 2005; *Wyant et al.*, 2006; *Khairoutdinov et al.*, 2008; *Benedict and Randall*, 2009; *Pritchard et al.*, 2011; *Goswami et al.*, 2011; *Pritchard et al.*, 2014). The experimental cases have GCM time steps of 600, 900, and 3600 seconds (f_{scale} is higher with a smaller time step). Table 2.1 summarizes the simulations performed. In all cases, regardless of global model time step, the CRM time step is 20 seconds, and the radiative transfer calculation is generally done every 900 seconds. The one exception is the 600 s time step case, in which the radiative transfer calculation is done every 600 seconds due to technical eccentricities of the SPCAM3 code. The simulation period is from September 1980 to December 1990. The first four months of spin-up period are discarded, and a complete decade of output (1981–1990) is used for climatological analysis. Sea surface temperature are prescribed based on time-varying monthly mean observed sea surface temperatures (*Hurrell et al.*, 2008).

Simulation	dtime600	dtime900	dtime1800	dtime3600
Time step [s]	600	900	1800	3600
f_{scale} [1/hr]	6	4	2	1

Table 2.1: The summary of SPCAM simulations performed in this study.

2.3 Results

2.3.1 Cloud forcing bias reduction with a higher f_{scale}

Figure 2.1 shows zonally-averaged annual top-of-atmosphere cloud forcings of model simulations and satellite observation. In all simulations (thin lines) clouds are optically too thick, especially in the shortwave compared to CERES-EBAF ed 2.8 (*Loeb et al.*, 2009) observations (thick lines). Inconsistent with hypothesis H0, several sensitivities to f_{scale} are immediately apparent. Interestingly, both the zonally-averaged annual short wave cloud forcing bias (SWCF; blue) and long wave cloud forcing bias (LWCF; red) improve with a higher f_{scale}. This suggests that f_{scale} can be a useful tuning knob for slightly reducing cloud radiative effect biases in SP models, with a reduced GCM time step producing improved cloud climatology. While the responses of zonally-averaged SWCF and LWCF are both monotonic to f_{scale}, the magnitude of the SWCF response is about twice as large as that of the LWCF response. This suggests low, liquid clouds respond more sensitively to f_{scale} than high, ice clouds do.

It is natural to wonder whether the reduction in cloud radiative forcing is simply driven by a fundamental reduction in precipitation, or deep convection in general. Zonally-averaged annual precipitation (figure 2.2) shows that this is not the case because the zonally-averaged annual precipitation both increases and decreases with increasing f_{scale} in the tropics, where the zonally-averaged annual cloud radiative forcings systematically decrease with increasing f_{scale}. The precipitation response to f_{scale} is clearly less systematic and less sensitive (at least for the 600–1800 s time step regime) than the cloud radiative response.

We hone in on the SWCF responses, since they are found to be the most significant sensitivity to f_{scale} (magnitude of $\sim$10 W/m^2). Figure 2.3a shows their global structure. This demonstrates that the zonal mean annual SWCF response is predominantly from the equa-

torial deep convective regions. As we will discuss in Section 2.3.4, this could be viewed as consistent with our working hypothesis H1, which predicts convective mixing efficiency is sensitive to f_{scale} due to the convective throttling effects. The sensitivity of SWCF to f_{scale} is geographically consistent with liquid water path (LWP) responses (figure 2.3b), i.e. with increasing f_{scale} SWCF reduces in regions of deep convection consistent with less liquid cloud in the same regions.

The LWCF response to f_{scale} is not expected from our working hypothesis (H1) because such a systematic response in LWCF was unseen in the CRM-domain restriction experiments of PBD14. We note that although the LWCF responses do show a systematic sensitivity to f_{scale}, the magnitude of this response is only half that of the SWCF sensitivity ($\sim$5 W/m^2), such that this is a secondary response. Figure 2.4a shows the global map of LWCF responses to f_{scale}. The LWCF responses are geographically more complex than the SWCF responses. The largest responses are still from the active convective regions—particularly Indo-Pacific Warm Pool region—as the SWCF responses are. But unlike the SWCF responses, the LWCF responses are not primarily concentrated in regions of the deepest tropical convection; there is an extratropical signal component that is more noticeable compared to the SWCF responses. Unsurprisingly, the LWCF responses are geographically consistent with ice water path (IWP) responses (figure 2.4b), i.e. with increasing f_{scale} the LWCF responses weaken in many regions, consistent with less ice cloud, though many regional anomalies are apparent. Clearly, f_{scale} affects the mean condensate amount in SPCAM3.

The nature of the overall sensitivity to f_{scale} seems geographically distinct for the longest time step analyzed (3600 s). In this case both SWCF and LWCF responses shift northward in the tropics, consistent with a bifurcation of the preferred mode of tropical mean state rainfall climatology (figure 2.5). Such meridional shifts are not observed in the other tests, in which the geographic responses looks more scattered rather than a systematic shift. This contextual difference is useful to keep in mind.

2.3.2 Amplification of tropical rain extremes with increasing f_{scale}

An unexpected finding in our simulations is that the tail of the tropical precipitation rate distribution (viewed from the perspective of the amount distribution, following *Pendergrass and Hartmann* (2014b,c)) intensifies as f_{scale} increases (figure 2.6a, c). Interestingly, this does not occur in the extratropics, where the precipitation distribution is virtually insensitive to f_{scale} (figure 2.6b, d). This is an unfavorable sensitivity, amplifying pre-existing biases against daily observations from GPCP 1DD ver 1.2 (*Huffman et al.*, 2001) and TRMM 3B42 ver 7 (*Huffman et al.*, 2007). This exacerbates the pre-existing bias of an overly intense extreme rainfall tail when using the 'micro-CRM' configuration of SPCAM3 as noted in PBD14. We acknowledge that current gridded estimates of surface precipitation derived from gauge-calibrated, IR-filled, microwave satellite merged products do not produce convergence of extreme rainfall rate magnitudes on sub-pentad timescales (*Liu and Allan*, 2012), such that it is difficult to select between either GPCP 1DD ver 1.2 or TRMM 3B42 ver 7 as "truth" in this analysis. TRMM 3B42 ver 7 tends to produce better agreement with rain gauge measurements in the tropics (*Tan et al.*, 2015) and incorporates more microwave data streams than GPCP 1DD (*Rossow et al.*, 2013). Accordingly, TRMM 3B42 ver 7 might be viewed as a more plausible baseline given raw microwave agreement with ground-based radar (*Wolff and Fisher*, 2009).

The precipitation distribution response to f_{scale} is mostly a shift of precipitation regimes from mid- to heavy-precipitation events in the tropics (figure 2.6a, c). While the dry rain frequency (< 1 mm/day) is relatively insensitive to f_{scale}, the mid-rain band (1–50 mm/day) is suppressed and the heavy-rain band (> 50 mm/day) boosts systematically with increasing f_{scale}. Whereas maps (figure 2.5) of the geographic structure of the mean precipitation response to f_{scale} suggest a regional redistribution, maps (not shown) of the precipitation variance response to f_{scale} show a tropics-wide systematic response—e.g. boosting precipitation variance monotonically with f_{scale} throughout the climatologically-active precipitation

centers in the tropics. This suggests that the tropical precipitation tail responses are probably due to a shift in some fundamental character of tropical convection and not a systematic change in the mean rainfall rate.

Is the striking sensitivity of the tropical rainfall tail associated with amplification of a particular mode of equatorial wave variability? Zonal wavenumber–frequency power spectra (e.g. *Wheeler and Kiladis* (1999)) are shown to examine the equatorial wave response to f_{scale}. Figure 2.7a–d shows the log power of zonal wavenumber–frequency spectra of equatorially symmetric daily precipitation rate from 10°S to 10°N. Figure 2.7e–g show the log ratios of responses of the experimental simulations to the control simulation.

No obvious mode of variability has responded to f_{scale}. Rather, the first-order response to f_{scale} is a shift of spectral power to higher frequencies at all zonal wavenumbers as f_{scale} increases; this is not as obvious in precipitation at low f_{scale} simulation (3600 s time step) whose spectral power decreases through a whole domain with a high frequency domain showing the largest reduction. There is a subtle sign that the moist Kelvin wave modes speed up (figure 2.7a–d) and strengthen (figure 2.8e–g) as f_{scale} increases. Although from this perspective it appears unlikely that a particular mode dominates the tail response, we acknowledge that a closer analysis of the association between extremes and variability would be needed to fully verify this, which is beyond the scope of this study. Meanwhile, we note the spectral responses are interesting in their own right. For instance, the Madden-Julian Oscillation (MJO) signals (eastward propagating oscillation with wavenumber of 1–2 and period of 30–60 days) are clearly visible in all simulations (figure 2.7a–d). PBD14 reported an insensitivity of SP-CAM3's MJO signal across different CRM extent and throttling configurations. This new result now shows the MJO is intrinsically robust in SPCAM3 to both CRM extent and f_{scale}.

2.3.3 Comparison of response with CAM3

Figure 2.9 reviews several additional climatologically important state variables, which helps to put the response of SPCAM3 to f_{scale} in the context of independent studies that have analyzed the effect of model time step on conventionally parameterized GCMs, including SPCAM3's twin sister, CAM3.0. All values shown in figure 2.9 are the area-weighted horizontal average over tropical ocean (20°S–20°N).

Tropical precipitable water (figure 2.9a) decreases slightly with a higher f_{scale}. We emphasize that a drying of the column could be viewed as consistent with a shift to a more efficiently ventilated convective mixing state owing to less throttled convection at high f_{scale} (i.e. consistent with hypothesis H1). The drier near-surface layer is associated with slightly enhanced surface latent heat (LH) flux by 1–2 W/m^2 (figure 2.9b), which is balanced through increased atmospheric moisture demand. That is, surface specific humidity anomaly responses to f_{scale} (figure 2.9c) tend to mirror mean surface LH flux changes (figure 2.9b) in the tropical horizontal average of surface LH flux as well as in its geographic pattern (not shown). In contrast, surface wind speed responses (figure 2.9d) do not provide a consistent balance to the increase in evaporation.

It is logical to assess if any of these sensitivities are consistent to those of conventionally parameterized CAM3, since SPCAM3 shares many model components with CAM3. Below we review how our results compare with *Mishra and Sahany* (2011b) (MS11 hereafter) who assessed the model time step sensitivity using CAM3 with a very similar model configuration to this study: real-geography, semi-Lagrangian dynamical core, T42 spectral resolution, 64×128 physical resolution. The tested time steps in MS11 were 300, 1200, and 3600 seconds.

Table 2.2 summarizes the sensitivities of important climate variables between SPCAM and CAM3 [MS11] in the wider tropics (30°S–30°N). The magnitude of sensitivity is measured as area-weighted, horizontally-averaged, time-averaged value of the shortest time step (600 s,

	SPCAM3	CAM3
Shortwave cloud forcing	**decrease (8.2 W/m^2)**	**increase (10 W/m^2)**
Longwave cloud forcing	**decrease (4.2 W/m^2)**	**increase (1 W/m^2)**
Precipitation	increase (0.1 mm/day)	increase (0.1 mm/day)
precipitation intensity tail	increase	increase*
Precipitable water	decrease (1.2 kg/m^2)	increase (1.1 kg/m^2)
Surface evaporation	increase (0.1 mm/day)	increase (0.1 mm/day)
Surface specific humidity	decrease (0.1 g/kg)	decrease (0.1 g/kg)
Surface wind	not systematic	increase (0.05 or 0.2 m/s)
Moist Kelvin wave modes	strengthen	weaken
Equatorial wave modes at high frequency	increase	decrease*

Table 2.2: Comparison of tropical (30°S–30°N) mean climate sensitivities between SPCAM3 and CAM3 when global model time steps decrease. All variables are area-weighted, time-mean, and horizontally-averaged first and then subtracted $\Delta t = 3600$ s ($\Delta t = 3600$ s) case from $\Delta t = 600$ s ($\Delta t = 300$ s) case for SPCAM3 (CAM3). CAM3 data are inferred from Figures 1 and 15 of *Mishra and Sahany* (2011b). Except cumulus parameterization, both simulation sets are done in very similar configurations: semi-Lagrangian dynamical core with T42 resolution, 10 year-long, and real-geography. Major responses found in this study are marked in bold. (*: more noticeable in aquaplanet CAM3 simulations in *Williamson* (2008))

300 s) minus that of the longest time step (3600 s, 3600 s) in each study (this study, MS11, respectively).

Interestingly, both time-mean SWCF and LWCF show *opposite* sensitivities in SPCAM3 and CAM3. The magnitudes of the SWCF sensitivity in both models are similar, but the LWCF sensitivity in SPCAM3 is much stronger ($\sim 4\times$) than that in CAM3.

The tropical mean precipitation is fairly insensitive to decreasing model time step in both models (consistent $\sim$0.1 mm/day increase), but heavy precipitation frequency show a noticeable sensitivity in both SPCAM3 and CAM3. In both models, the heavy precipitation events become more frequent as model time step decreases. Similar sensitivity is found also in aqua-planet CAM3 and CAM4 by *Williamson* (2008) and *Williamson* (2013), respectively, that have argued the contributor of the heavy precipitation tail response is due to large-scale precipitation, not convective precipitation. The large-scale precipitation response seems to be attributed to the limited moist instability removal capability of cumulus param-

eterization suites in CAM3 and CAM4 with rigid convective instability depletion timescales (*Williamson*, 2013) as mentioned in Section 2.1. We point out that this is unlikely to be the cause of the consistently signed precipitation tail response to f_{scale} in SPCAM3, since one would expect resolved CRM convection to efficiently remove convective instabilities as they develop. Nonetheless the precipitation tail response occurs in a consistent direction in both model types.

The equatorial wave responses to model time step are vastly different between SPCAM3 and CAM3. The first-order response to decreased time step in SPCAM3 is the shift of spectral power towards higher frequencies at all zonal wavelengths. In addition, the potential strengthening and propagation speed increase of moist Kelvin wave (MKW) modes are observed in SPCAM3. However, CAM3 shows very different responses. MS11 reported the decrease of spectral power at high-fequency, high-zonal wavenumber domain with a decreased time step in CAM3, but the systematic spectral power shift was unseen. MS11 also showed weakened spectral power and decreased propagation speed of MKW modes with a decreased time step in CAM3.

Interestingly, several SPCAM3 sensitivities to increasing exterior model *time resolution* show remarkable similarities to CAM3 sensitivities to increasing *horizontal resolution*. *Williamson* (2008) assess the sensitivities of both time step and horizontal resolution in aqua-planet CAM3. While the time step sensitivity found in aqua-planet CAM3 are mostly consistent to MS11, a few variables exhibited sensitivities to horizontal resolution opposite to that in time step. For example, with increasing horizontal resolution at a fixed time step, precipitable water decreases, and the spectral power of tropical waves increases at high frequencies at all zonal wavelengths.

In summary, SPCAM3 and CAM3 show some key differences in their responses to global model time step. Time-mean shortwave cloud optical thickness is reduced in SPCAM3 but is oppositely increased in CAM3 as model time step is reduced. Secondary longwave cloud

forcing responses are noticeable in SPCAM3 whereas they are mostly insignificant in CAM3. Furthermore, although the tropical precipitation tail is increased in both models, equatorial wave spectra reveal this occurs for distinct reasons. This confirms the effect of global model time step, perhaps through its additional effect of acting as a scale coupling frequency, can affect simulated climate in SP models in unique and unfamiliar ways.

2.3.4 Inconsistency with throttling expectations

Our null hypothesis (H0) is that SPCAM3 would be *insensitive* to f_{scale} due to the lack of rigid convective adjustment timescales that have been implicated in primary responses to model time step seen in conventionally parameterized GCMs. This is clearly ruled out—our findings show that the simulated climate in SPCAM3 is sensitive to f_{scale} at a comparable magnitude of time step sensitivities of CAM3, though in a different way.

Our alternative hypothesis (H1) is that f_{scale} might affect SPCAM's climatology through its effects on convective throttling physics in limited CRM domains. The expectation of H1 is that we would observe *reverse sensitivities* with increasing f_{scale} compared to those seen for reducing CRM domain extent in PBD14. The overall idea is that the artificial environment of locally trapped compensating subsidence inside a CRM is only formally true for a closed system within the timescale of a single GCM time step—such that if the GCM and CRM couple more frequently, biases imposed by a limited CRM domain size will be buffered by more frequent information exchange with large-scale dynamics. In other words, more frequent scale coupling could be viewed as a way to help "open" the artificially closed CRM system somewhat to compensate for artificial effects on mixing due to a limited CRM domain.

Consistent with the expectation from H1, increased f_{scale} has produced a striking effect reminiscent of lessened convective throttling—a monotonic reduction of SWCF biases in regions of

the deepest convective mixing. Figure 2.10 confirms the systematic nature of this dominant response by analyzing the daily precipitation-binned, time-mean liquid condensate profile in an active convective region over ocean, 10°S–10°N, 60°E–170°E. This further emphasizes that the liquid condensate levels in the lower atmosphere systematically decrease *across all precipitation regimes* as f_{scale} increases. Consistent with H1, the reverse is seen in PBD14 (their figure 12).

However, other aspects of the response to f_{scale} are inconsistent with an overarching convective throttling argument. For instance, the CRM-diagnosed net updraft mass flux profiles in tropical convective regions (figure 2.11a) indicate that f_{scale} acts to *vertically shift* them towards a more bottom-heavy state—rather than *boosting* the magnitude of net saturated updraft mass fluxes throttled at all levels (the hallmark of the convective throttling mechanism; figure 2.11b). This seriously undermines the credibility of the convective throttling hypothesis (H1). Distinctly, f_{scale} appears to affect the diabatic heating profile of convection rather than its mixing efficiency, with a higher f_{scale} promoting more bottom-heavy convection.

Other deeper lines of analysis further reveal inconsistencies with H1. For instance, the liquid water response to f_{scale} is a monotonic decrease at all vertical levels with a higher f_{scale} (figure 2.10), while unwinding convective throttling is expected to cause a shift of condensate from lower to upper troposphere as shown in PBD14 (their figure 12). Furthermore, H1 predicts the most extreme precipitation events should become less frequent with a higher f_{scale}. However, we have seen the reverse response in that the precipitation intensity tail boosts with a higher f_{scale} (figure 2.6). Likewise, H1 predicts a vertical redistribution of convective heating with increased f_{scale} with unthrottling leading to more (less) convective energization at upper (lower) troposphere, another hallmark of planetary boundary layer ventilation effects not shown in PBD14 but shown in figure 2.12b. However, this effect is not seen in the vertical profiles of moist static energy (MSE) tendency (figure 2.12a). A

weak sensitivity of the convective MSE tendency occurs in response to f_{scale} in the lower atmosphere is observed, but it is not associated with convective moistening, and is remarkably insensitive compared to the ventilation effects involving vertical redistribution under convective throttling in PBD14 (figure 2.12b).

In short, there is convincing evidence that convective throttling arguments (H1) cannot explain the effect of f_{scale}.

2.3.5 Consequences of a convective organization sensitivity

The above analysis has revealed that f_{scale} seems to produce a fundamental shift in the nature of *convective organization* (in terms of the vertical profile of convective mass fluxes and associated diabatic heating) in SPCAM3, with a reduced global model time step leading to more bottom-heavy convection. Here we explore whether an overarching argument beginning with a shift in the vertical structure of convection can explain the set of effects we have seen.

Figure 2.11a clearly shows the mass flux profile becomes more bottom-heavy as f_{scale} increases. Gross moist stability (GMS) is a useful metric here because it tells how efficiently column MSE is exported by horizontal divergence compared to the convective strength in a column, with clear links to the sensitivity of precipitation to external perturbations. We note that a more bottom-heavy mass flux profile would in turn import more MSE to a column because the environmental MSE decreases (increases) with height in lower (upper) troposphere. We follow *Raymond et al.* (2009) and normalize GMS by column vapor import but note that our conclusions are robust to alternately normalizing by dry static energy export as the measure of convective activity in the denominator of the normalized GMS, which is given by

$$GMS = -\frac{\int \nabla \cdot (h\mathbf{v})dp}{\int L_v \nabla \cdot (q\mathbf{v})dp}, \tag{2.1}$$

where h is the moist static energy, $\mathbf{v}$ is the horizontal velocity field, L_v is the specific latent heat of vaporization, and q is the specific humidity. The total advective tendencies of h and q are derived directly from the model as the residual between the total tracked tendency from daily model snapshots minus the daily mean accumulated tendency due to all model physics.

Figure 2.13 shows that time-mean GMS decreases with increased f_{scale} in active convective regions, as expected as a consequence of a more bottom-heavy profile of vertical mass flux. In addition, with a higher f_{scale}, the MSE profile becomes slightly steeper (i.e. more negative $\partial\theta_e/\partial z$) in the lower troposphere while the moist lapse rate does not change in the upper-troposphere (not shown); this also contributes to the reduction of GMS as f_{scale} increases, but it is secondary to the vertical mass flux profile shifts. This GMS response is relevant to understanding the precipitation responses to f_{scale} because GMS defines a linkage between net precipitation (precipitation minus evaporation) and diabatic column MSE sources and sinks such as surface flux and radiative cooling (e.g. see equations 2.1–2.3 in *Raymond et al.* (2009)). At steady state a consequence of reduced GMS is enhanced sensitivity of net precipitation to a given magnitude of diabatic forcing of the column. From this view, the shift to a more bottom-heavy convective mass flux profile is consistent with an increased frequency of extreme rainfall events at high f_{scale}. Thus a change in tropics-wide vertical structure of convection may partially explain the tail response seen in the precipitation distribution. Similar arguments also apply to unsteady precipitation variability, which is not analyzed here, except that in unsteady cases it is also possible that MSE storage in a column can be altered through moisture convergence, and if GMS responds to this column MSE change, the changes in both column MSE and GMS could enhance or compensate each other.

The systematic reduction of SWCF and LWCF with increasing f_{scale} could be viewed as stemming from an overarching effect of convective organization resulting in increased pre-

cipitation efficiency [S. Tulich, personal communication]. Thus organization changes could be viewed as an indirect cause of reduced column-integrated liquid water and ice water, and hence reduced longwave and shortwave cloud forcing. Indeed, the precipitation distribution shift towards more intense events could be a signal of increased precipitation efficiency, although a detailed analysis of condensation rates against surface precipitation would be needed to confirm this.

In summary, although impossible to explain with throttling arguments under our original working hypothesis (H1), it seems possible to explain a broad set of responses to f_{scale} in SPCAM3 as the result of an overarching change in convective organization favoring more bottom-heavy convection, reduced gross moist stability, and enhanced precipitation efficiency at a high f_{scale}.

2.4 Discussion

It is unknown but worth speculating on what physical mechanisms might require an increasingly bottom-heavy convective profile as a result of a shorter global model timestep (more frequent scale coupling between explicit deep convection and large scale dynamics) in SPCAM3.

2.4.1 A convection-gravity wave feedback strawman

We propose that a relevant mechanism could be enhancement in the efficiency of a known feedback between explicit convection and large planetary waves that leads to changes in bottom-heaviness in reduced-order simulations. *Kuang* (2011) (K11 hereafter) used a cloud system resolving model coupled instantaneously to advection from a single zonal gravity wave to explore the interaction between local convection and planetary-scale gravity waves.

This dynamical scaffold can be viewed as an analog to SPGCMs—like SPCAM3, the K11 model explicitly resolves deep convection using a CRM, but within a simpler single-wave dynamical scaffold. The K11 model also enforces "stiff" (instantaneous) coupling to a single tropical gravity wave at a fixed wavelength whereas in SPCAM3 the coupling can be "loose" (infrequent, as limited by f_{scale}) and is with a spectrum of large-scale modes including but not limited to large tropical gravity waves.

Although indirect, the analogy is worth considering because K11 showed that when convection is allowed to feed back instantly with very large scale gravity waves, top-heavy forms of convective organization become limited due to an intrinsic inconsistency with the large thermal anomalies that would be needed to balance them—tangentially, for our purposes, implying a breakdown of strict weak-temperature-gradient (WTG; *Sobel et al.* (2001)) at sufficiently large zonal scales. It is conceivable that a similar organization-limiting mechanism could operate in SPCAM3 whereby increasing f_{scale} allows convection to feed back more "stiffly" (instantaneously) with GCM-resolved waves, including some that are large, and thus following reasons in K11 requiring a downward shift toward a more bottom-heavy form of organization. In contrast at a low f_{scale}, convection is left to its own devices for long periods, with infrequent and thus inefficient self-correcting large scale gravity wave interaction. In this way convection might become artificially top-heavy—that is, less bottom-heavy than it would have been interacting more frequently with a spectrum of waves, some of which are large.

The argument above is clearly speculative and we simply suggest it as a strawman for future work to either confirm or deny. It is not immediately obvious how to test it diagnostically in our simulations. Although it is tempting to causatively interpret thermal perturbations from the WTG on large zonal scales, since these are involved in the mechanisms that act to limit top-heaviness in the K11 analogy, this is not actually clear. On the one hand, one might expect increased departures from the WTG under high f_{scale} as a prediction from the analogy.

But this need not be the case if thermal anomalies are part of self-limiting inconsistency that ultimately selects for a downward vertical shift to avoid excessive wave-interactive thermal anomalies. Thus it is difficult to derive insight on the validity of the analogy from diagnosis of free tropospheric temperature perturbations.

2.4.2 Weak-temperature-gradient sensitivities

We nonetheless perform an analysis of the degree of departure from the WTG in our simulations, since it turns out to be interesting in its own right. Figure 2.14a shows the horizontally-averaged daily temperature anomaly from the 5°S–5°N tropics-wide horizontal mean at 300 hPa ($T300'$). Under perfect WTG, these anomalies would be perfectly zero, but deviations can occur, and are found to be sensitive to f_{scale} in this study. To discriminate days and regions that are experiencing mean uplift from those that are subsiding, the results are further binned by the vertical velocity anomaly at 500 hPa ($\omega 500$).

The interesting point in figure 2.14a is that increasing f_{scale} reduces the magnitude of the $T300'$ such that SPCAM3's behavior becomes more WTG-like as f_{scale} increases. A vertically resolved view of this departure from the WTG (figure 2.15) in tandem with the frequency distribution of mid-level ascent (figure 2.14b) provides a suggestive clue to its cause [C. Bretherton, personal communication]. The idea is that thermal anomalies arise from convective plumes as they deposit thermal energy by water vapor condensation in the upper atmosphere, but that these local heat anomalies (e.g. $T' > 0$) are then spread to adjacent GCM grid columns via dynamical adjustment. In SPGCMs, dynamical adjustment is limited by the timescale on which CRM and GCM are coupled. When longer time steps are used, local convection confined in an embedded CRM can build up to produce larger thermal anomalies that would in turn require a more vigorous GCM-scale vertical velocity response. This reasoning seems to satisfyingly explain both the increased magnitude of thermal depar-

tures from WTG when using longer time steps, as well as the transition to a more intense updraft spectrum in the $\omega < -0.1$ (Pa/s) range.

Of course this dynamical adjustment argument cannot explain the shift towards bottom-heavy mass flux profile, with an increased f_{scale}, that we have argued is an overarching cause of the set of climatological responses. But it is interesting to note that decreasing the global model time step reduces the magnitude of convectively induced horizontal thermal anomalies, effectively increasing the rigidity of the WTG in superparameterized simulations.

To further clarify which spatial scales produce the interesting effect of f_{scale} on WTG stiffness, we extend our analysis of $T'\omega$ to see its dependence on zonal wavelength. Figure 2.16 shows the zonal cospectrum between daily $T300'$ and $\omega 500$ in the deep tropics (5°S–5°N). It suggests planetary-scale disturbances, i.e. small zonal wavenumbers, dominate the sensitivity to f_{scale} of the covariance between T' and ω. The overall sensitivity (weaker $T'\omega$ covariance with a higher f_{scale} in the small zonal wavenumber domain) is consistent with figure 2.7, which shows the weakening of low-frequency equatorial waves—whose spectral power is most concentrated in small zonal wavenumbers—with increasing f_{scale}.

The fact that the very largest scales seem to respond especially to f_{scale} argues that more than local dynamic adjustment physics respond to f_{scale}. It is interesting to note that the largest scales are also those that were implicated in a shift to more bottom-heavy convection under "stiff" convection-gravity wave coupling in K11, though we acknowledge again that a direct linkage between our results and K11 is a bit unclear and worth further inquiry.

2.4.3 Is there an optimal f_{scale}?

What should the global model time step / scale coupling frequency (f_{scale}) between CRM and GCM be set to in a perfect world?

Philosophically, it is tempting to think that infinitely fast scale coupling might be desirable for SP simulations such that individual updraft plumes can quickly interact with fast modes of large-scale dynamics such as GCM gravity waves. For instance, there could be multiple sequential deep convective plumes in a CRM domain within a given GCM time step. However, if f_{scale} is low, individual plumes are not able to interact with large-scale dynamics, e.g. exciting gravity waves or dynamic adjustment, because the scale coupling only passes the column-averaged information at the end of the CRM integration. In this line of thought, a higher f_{scale} is preferred in SPGCMs.

On the other hand, there are also good philosophical arguments to consider avoiding too frequent scale coupling (too short global model time step), based on the typical response timescales of CRM domain-mean properties being on the order of an hour or more, as well as unphysical intra-CRM effects [S. Tulich, personal communication]. For instance, if f_{scale} is too high, a field of evolving cloud elements in a given CRM will not have had enough time to equilibrate with each other via mutual intra-CRM-scale gravity wave radiation, and portions of information can be prematurely transmitted between cloud elements through artificial interaction with the host GCM, which implicitly involves horizontal homogenization of information (see appendix in *Benedict and Randall* (2009) for further details on the CRM–GCM scaffold). In this line of thought, too high f_{scale} could be viewed as a philosophical problem for SP models that might produce artificially fast interaction between independent clouds inside CRMs. How or whether such artificial elements of the SP-scale interface engineering may have impacted problems seen in our and others' SPCAM simulations remains unclear but worth future inquiry.

Practically, some of our pilot-test results make a case for using very short global model time steps in superparameterized models. The favorable SWCF and LWCF responses and reduced tropical free tropospheric thermal anomalies might imply that an increased f_{scale} is better for SP simulations if time-mean cloud climatology and WTG-fidelity are key tuning factors. On

the other hand, the trade-off of producing a very strong tropical extreme precipitation tail could be viewed as unsatisfying, although a stable estimate of the magnitude of this tail in observations is still in debate (*Liu and Allan*, 2012).

2.5 Conclusion

The effect of GCM time step (and hence scale coupling frequency f_{scale}) in the uncoupled SPCAM3 has been systematically assessed. A few important climate state variables are discovered to be systematically sensitive to f_{scale}. The most striking responses occur in time-mean cloud radiative forcing and appear to be promising: the zonally-averaged annual SWCF and LWCF weaken and their biases against satellite observation are reduced at every latitude as f_{scale} increases. The magnitude of this sensitivity is most striking in SWCF ($\sim$ 10 W/m^2) and half as strong in LWCF ($\sim$ 5 W/m^2) in the tropics. That is, the climatology of low liquid clouds is more sensitive to f_{scale} than high clouds.

f_{scale} affects not only mean-state climate but also the tropical precipitation distribution. Extreme precipitation events become more frequent with increasing f_{scale}, which can exacerbate a pre-existing precipitation bias in SPGCMs that use small, throttled CRMs for computational efficiency. It illustrates additional effects of f_{scale} can occur with trade-offs for climate simulation. This tail response is ubiquitous throughout the tropics and not significantly linked to any particular equatorial wave mode responses. Rather, the spectral power of tropical waves shifts towards higher frequencies at all zonal wavenumbers with increasing f_{scale}, although moist Kelvin wave modes show a weak mode-specific intensification.

The global model time step sensitivity of SPCAM3 is distinct from more familiar sensitivities that have been documented in the conventionally parameterized CAM. While both models show similar magnitude of sensitivities to time steps for the majority of compared variables,

the signs of sensitivities of important climate variable disagree, including SWCF, LWCF, precipitable water, and the direction of spectral power shifts of equatorial waves. This discrepancy confirms model time step influences simulated climate of SPGCMs in a different way compared to traditional GCMs, possibly through their distinct role as the scale coupling frequency.

We began with a working hypothesis H1 that the dominant SWCF response may be the result of moist ventilation efficiency being modulated by f_{scale}. This builds on ideas of PBD14 that within a single GCM time step, deep convective updrafts can become throttled by a limited CRM domain through overly strong compensating subsidence. In this context, a higher f_{scale} could play an important role in buffering artificial throttling by exposure to the large scale dynamics of a host GCM. This view seemed consistent with the observed dominant response in our simulations of low-level liquid clouds decreasing monotonically with f_{scale}, especially in regions of strongest convection. However, it cannot explain other effects such as the LWCF bias reduction with increasing f_{scale}. More importantly, hypothesis H1 predicts the reverse expectation for the observed tropical precipitation tail response. It is also inconsistent with the observed vertical mass flux responses—the downward shift of the convective mass flux profile with increasing f_{scale}—which is distinct from the expectation of uniformly increased convective mass fluxes. Thus, contrary to our initial working hypothesis H1, our analysis revealed a higher f_{scale} does not unwind convective throttling and the SWCF responses are not the result of such unwinding, despite coincidentally similar geographic response signatures.

Instead, based on the balance of evidence, the primary effect of f_{scale} seems to be to induce a fundamental change in convective organization leading to a more bottom-heavy mass flux profile with a higher f_{scale}. Associated reduction of time-mean GMS might promote the intensification of heavy rainfall frequency in the tropics. From this view, enhanced precipitation efficiency associated with the new convective organization state could be viewed as ultimately driving the reduction of suspended condensate—and hence the systematic SWCF

and LWCF responses and favorable reductions in cloud optical biases at a high f_{scale}.

It is unknown what fundamental physical processes ultimately respond to f_{scale} to require this systematic vertical shift in convective organization. We have speculated that the efficiency of convection-gravity wave feedbacks may play a role based on theoretical ideas put forward in K11 and consistent vertical shifts in SPCAM's convective mass fluxes. But we have emphasized it is difficult to causatively rule in or out. This topic would benefit from further inquiry and careful sensitivity study. The capabilities of the newly developed SP-WRF (*Tulich*, 2015) could prove especially illuminating in this regard, due to its unique ability to study superparameterization physics in limited domains and idealized configurations, with fully cloud-resolving benchmarks for validation. Work is underway using this new superparameterized model that illuminates a mechanism [S. Tulich, personal communication].

Meanwhile, the results of this study are already relevant to SPGCM simulations that take advantage of unusually small CRMs to gain some of the benefits of superparameterization without its full computational cost. SPGCM simulation is still computationally demanding despite the continuous expansion of computational resources. One way to make it more affordable is to use small CRMs, but this can distort mean climate, especially SWCF as shown in PBD14. Using higher f_{scale} can mildly alleviate this problem, though with tradeoffs in the realism of tropical rainfall extremes and nature of convective organization. We note that using short global model time steps does not add much computational burden to a SPGCM because the number of CRM time steps is unchanged and the CRM workload dominates the SPGCM total computational workload. This is in contrast to conventional GCMs, where the global dynamics calculation tends to represent a nontrivial fraction of the overall computational workload, and thus calculating global dynamics more frequently can noticeably erode model's computational performance.

A limitation of this study has been the exclusive use of an unusually small CRM in all simulations, comprising only 8 independent columns. While this had the advantage of starting from

a highly throttled CRM configuration, designed to test a physical hypothesis, it may also have inadvertently stacked the decks for finding strong sensitivities to global model time step. Revisiting these sensitivity experiments in a baseline SPGCM using a CRM configuration with many more columns (32 or greater) would be helpful for testing the representativeness of some of our key findings. Such an analysis would require substantially more computational resources to investigate, and is beyond the scope of this study, but work on this front is underway.

Generally, there are several implications for understanding the emergent behavior of, and perhaps for tuning, the next generation of SPGCMs. SP models are relatively new and untuned, and the origins of some of their emergent convective organization, as well as their sensitivities to assumed scale coupling parameters, have not been fully assessed. The global model timestep has proved to be an interestingly direct lever on the bottom-heaviness of simulated convection and the fidelity of the WTG, which may help inform how the dynamics of organized convection manifest across the two resolved scales in SPGCMs. For tuning, although it does not fit the description in a traditional sense, f_{scale} could be regarded as a *dynamical* tuning parameter. In this context its key eccentric property is to reversely affect the optical thickness of time-mean cloud fields versus the intensity of the tropical extreme rainfall tail. Whether these properties might prove to be useful ammunition for tuning the next generation of SPGCMs depends on whether they can be leveraged against complementary trade-offs of other more traditional tuning parameters such as CRM microphysical assumptions. Such strategies could prove worth exploring as SPGCMs exit their infancy.

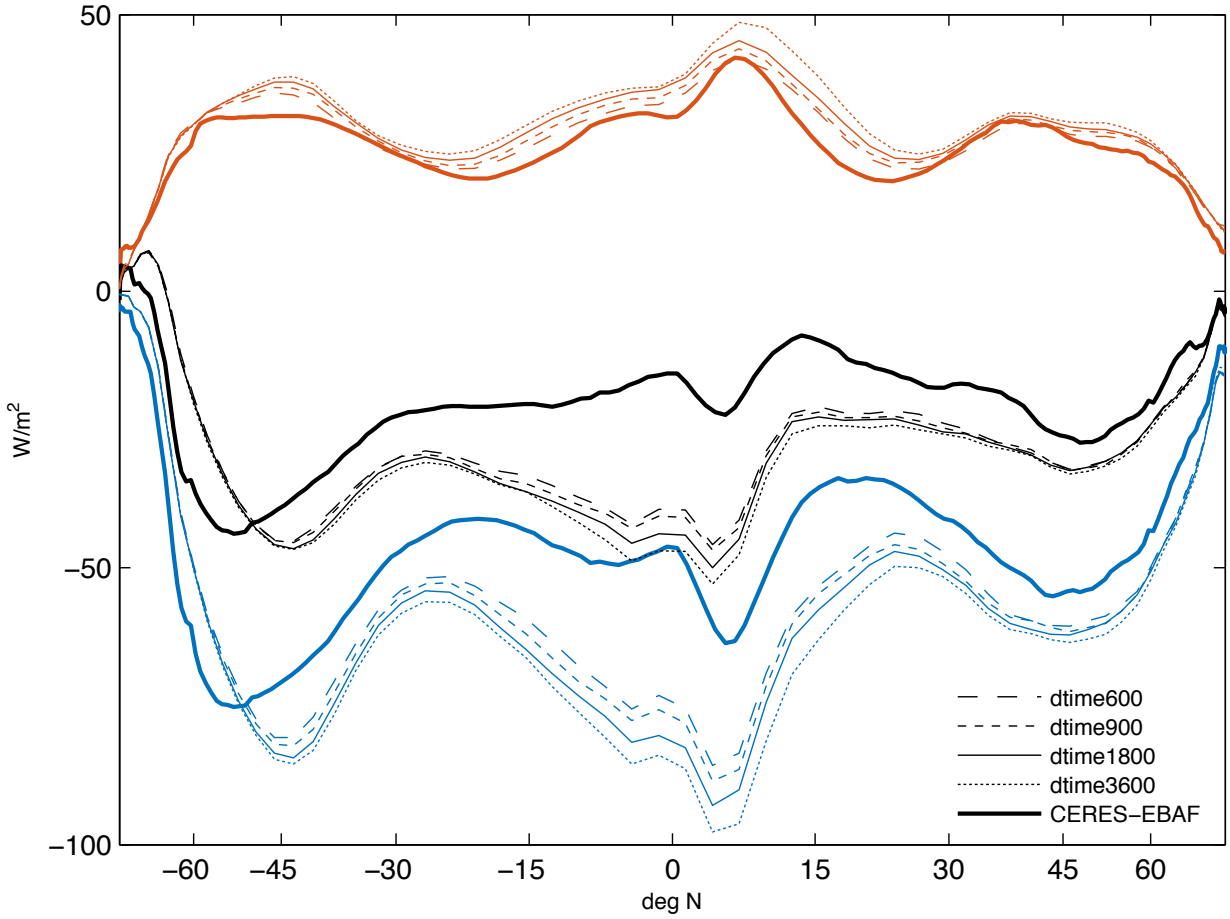

Figure 2.1: Zonally-averaged annual mean net (black), shortwave (blue), and longwave (red) cloud forcing in SPCAM3 simulations (thin lines) and observation (thick solid lines).

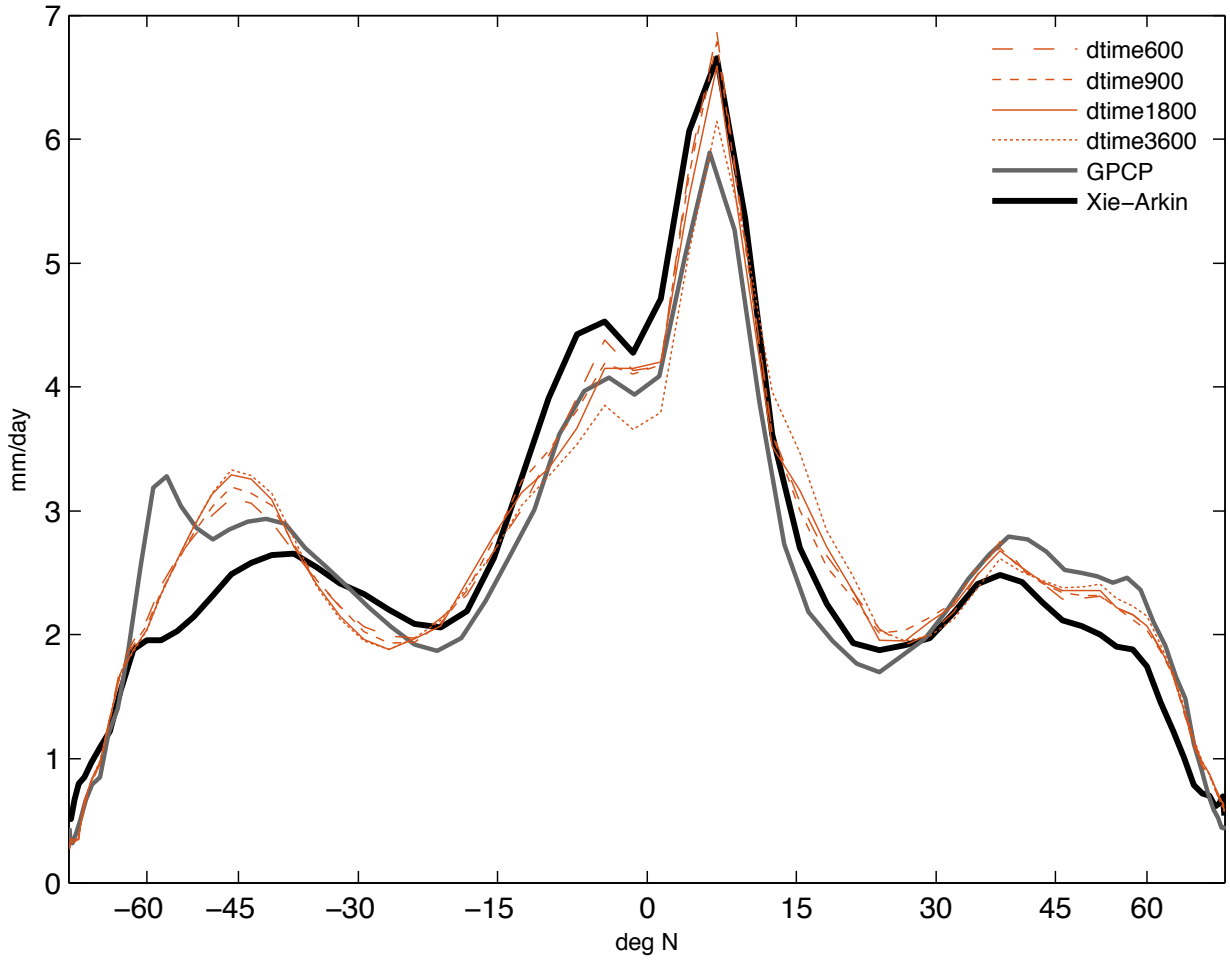

Figure 2.2: Zonally-averaged annual mean precipitation rate in SPCAM3 simulations (thin lines) and observation (thick solid lines).

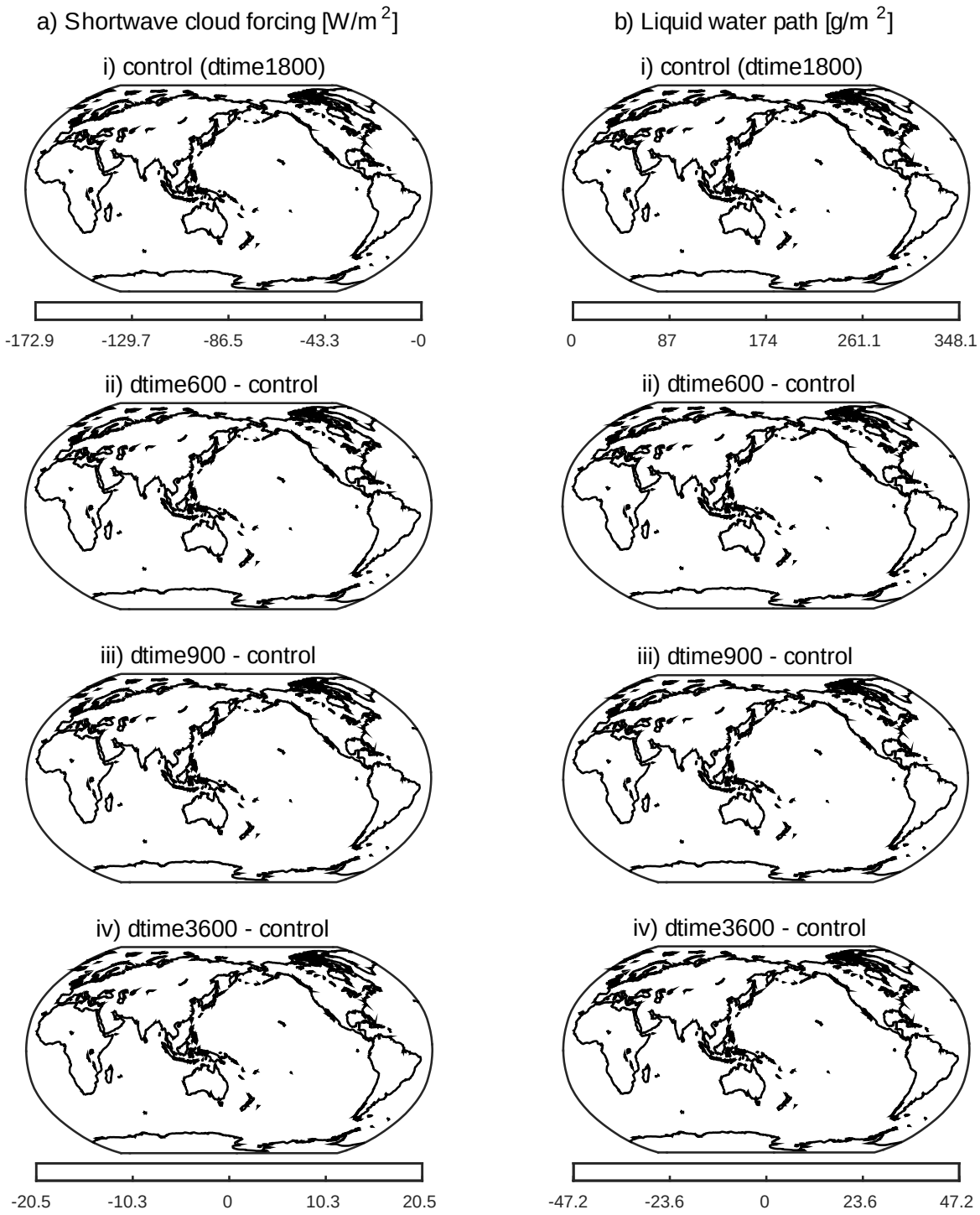

Figure 2.3: (a) Annual mean shortwave cloud forcing and (b) liquid water path from SPCAM3 simulations. (i) control simulation and (ii–iv) experiment simulation anomalies against control simulation.

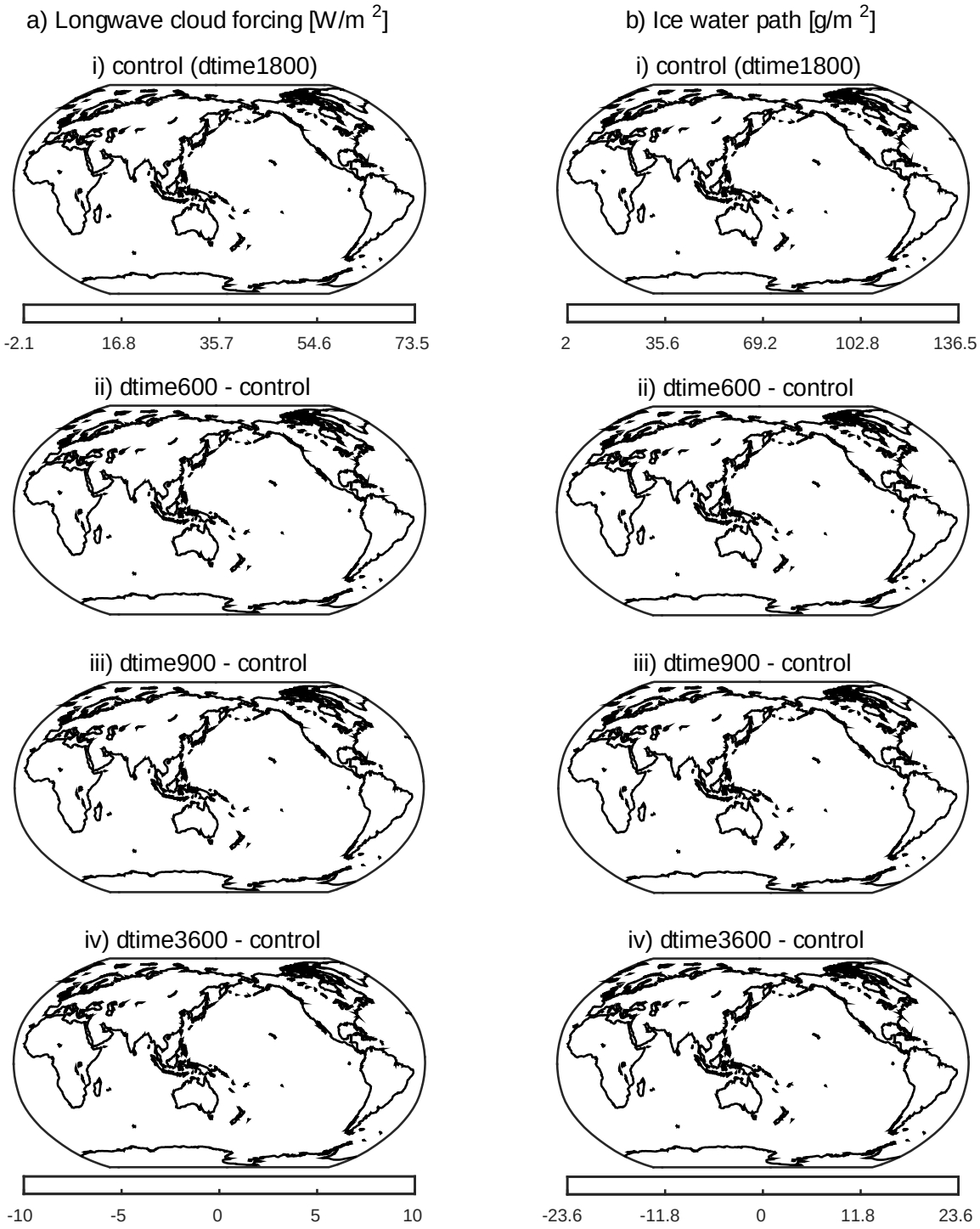

Figure 2.4: (a) Annual mean longwave cloud forcing and (b) ice water path from SPCAM3 simulations. (i) control simulation and (ii–iv) experiment simulation anomalies against control simulation.

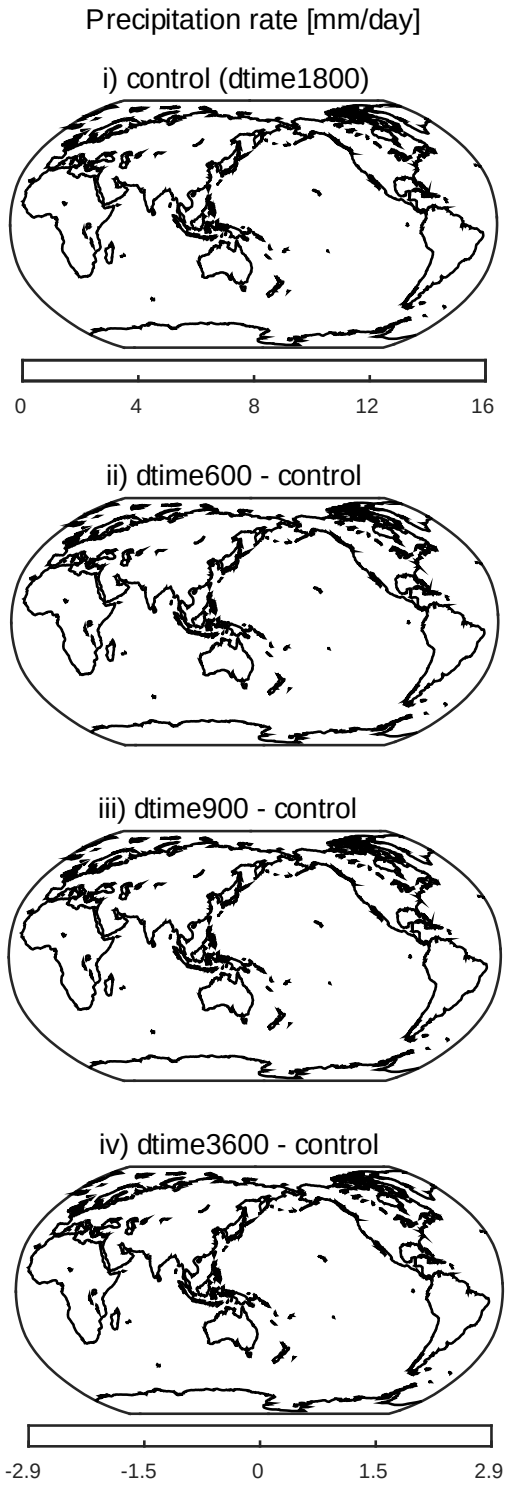

Figure 2.5: Annual mean precipitation rate from SPCAM3 simulations. (i) Control simulation and (ii–iv) Anomalies against control simulation.

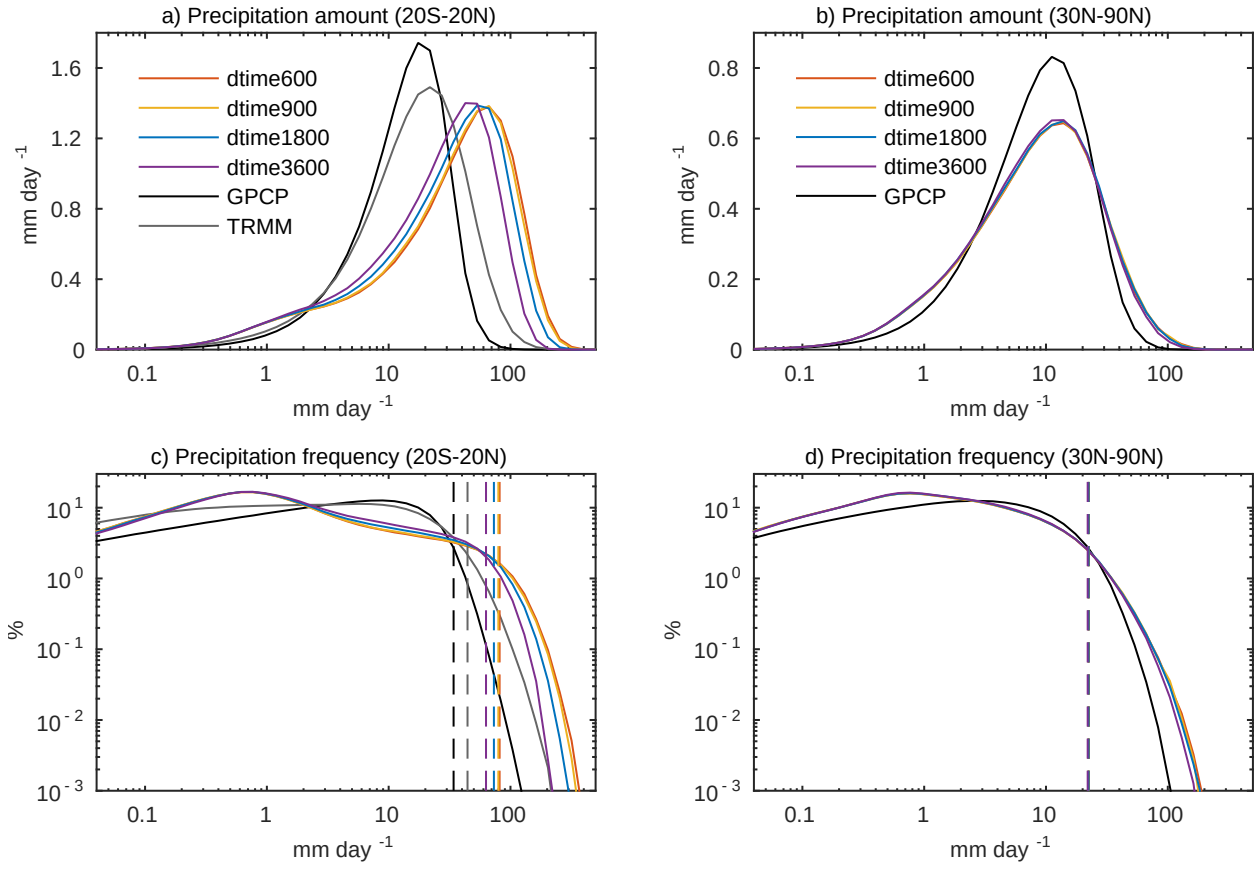

Figure 2.6: Amount (top; a and b) and frequency (bottom; c and d) distributions of daily mean precipitation rate in the tropics (20°S–20°N) (left; a and c) and northern hemisphere extra tropics (30°N–90°N) (right; b and d). Precipitation in southern hemisphere extra tropics (30°S–90°S) is very similar to b and d (not shown). The dashed lines in c and d show 99th percentiles of daily mean precipitation rate.

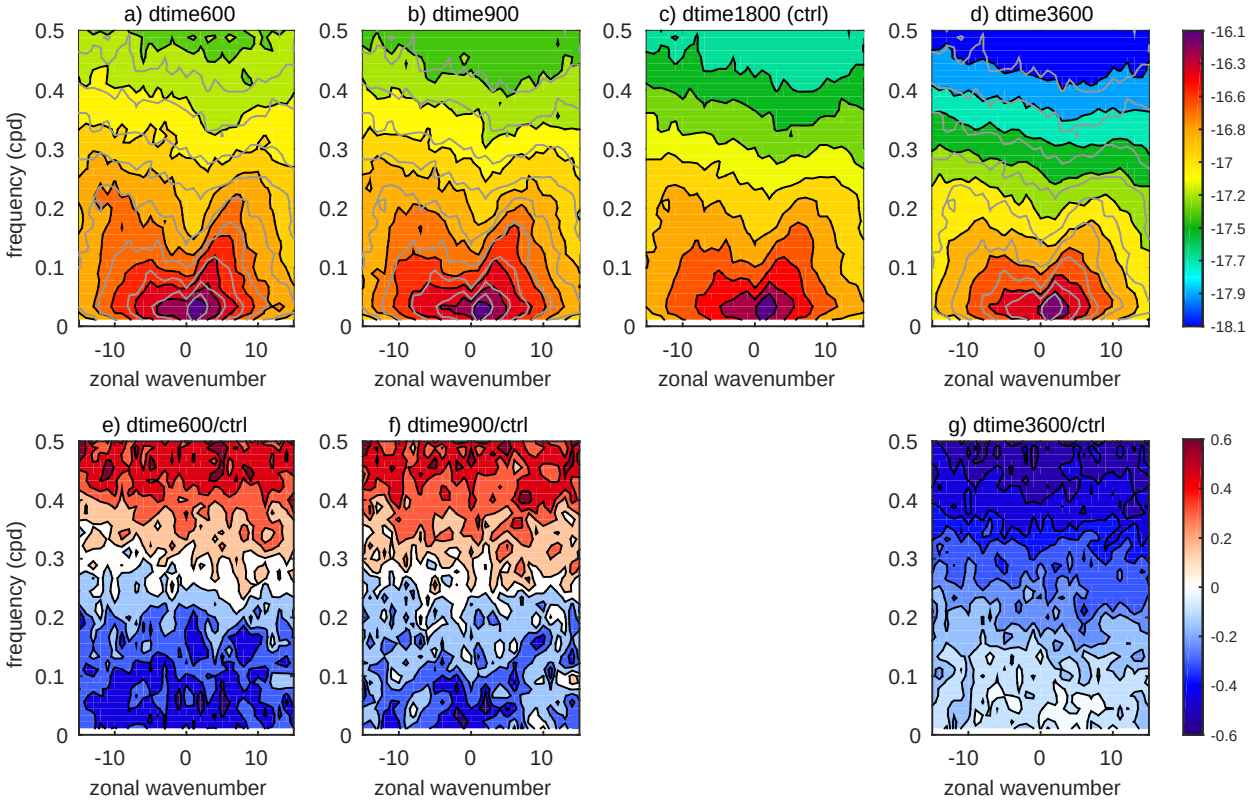

Figure 2.7: Zonal wavenumber–frequency log power spectra of equatorially symmetric daily mean precipitation rate in 10°S–10°N. (a–d) Raw log power spectra and (e–g) the ratio of log power of experimental simulation to control simulation. Grey contour lines in a, b, and d are the contour line in the control simulation in c.

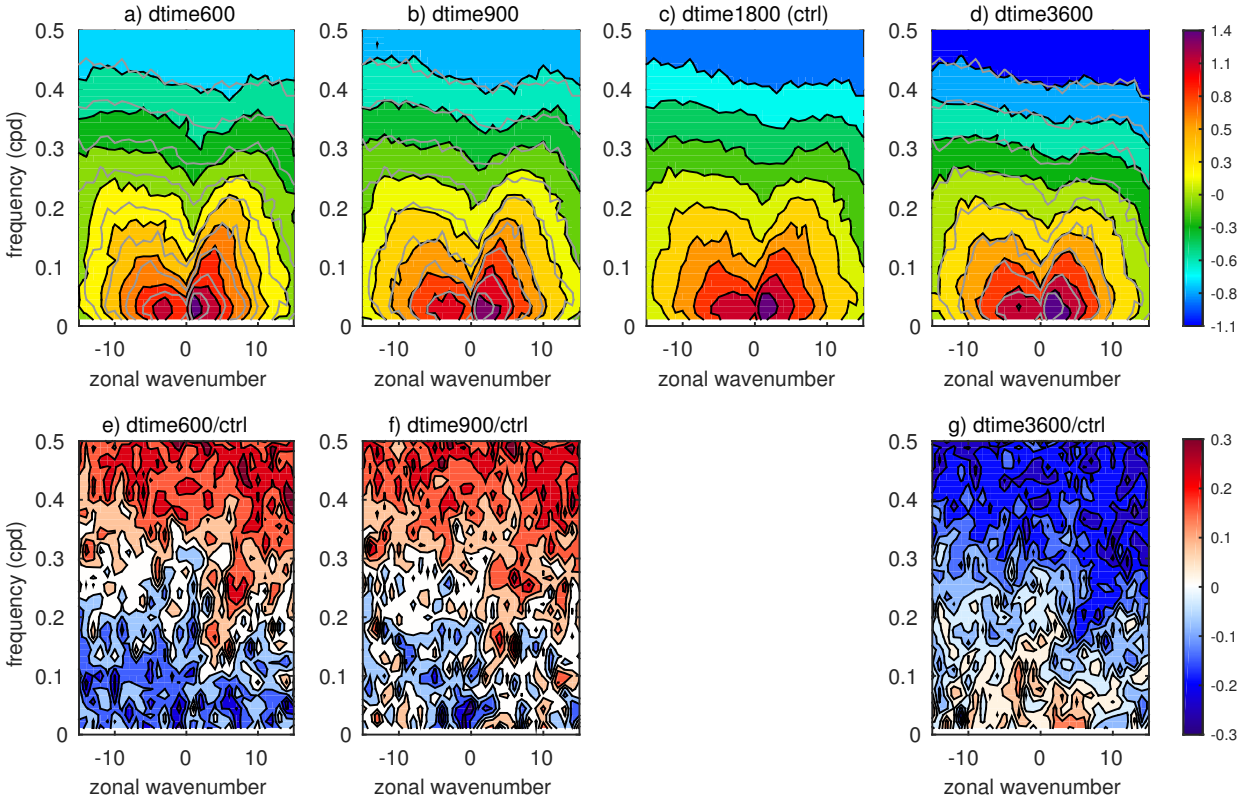

Figure 2.8: Same as figure 2.7 but with outgoing longwave radiation at the top of atmosphere.

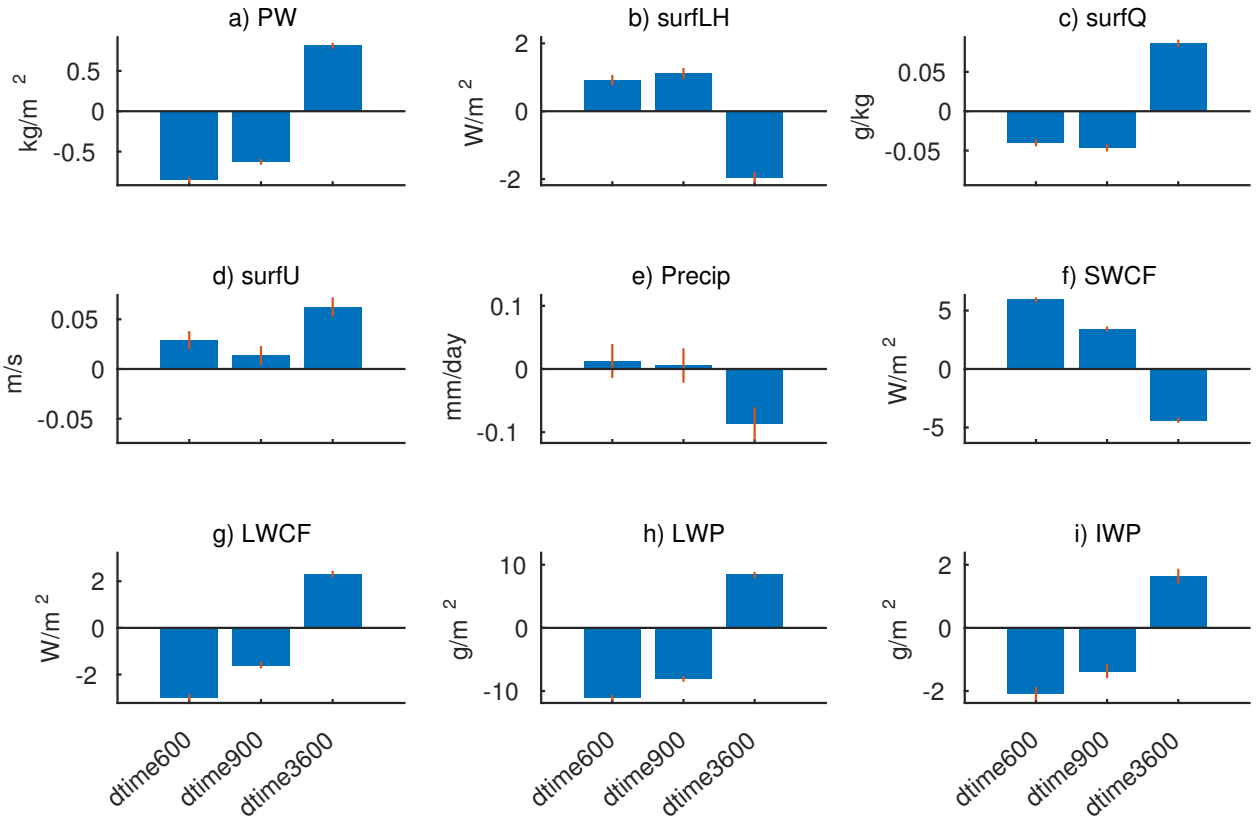

Figure 2.9: Area-weighted, annual mean anomalies of important climate variables over the tropical ocean (20°S–20°N). (a) Precipitable water; (b) Surface latent heat flux; (c) Surface specific humidity; (d) Surface wind; (e) Precipitation rate; (f) Shortwave cloud forcing; (g) Longwave cloud forcing; (h) Liquid water path; and (i) Ice water path. The red error bars show 95% confidence intervals of monthly mean values.

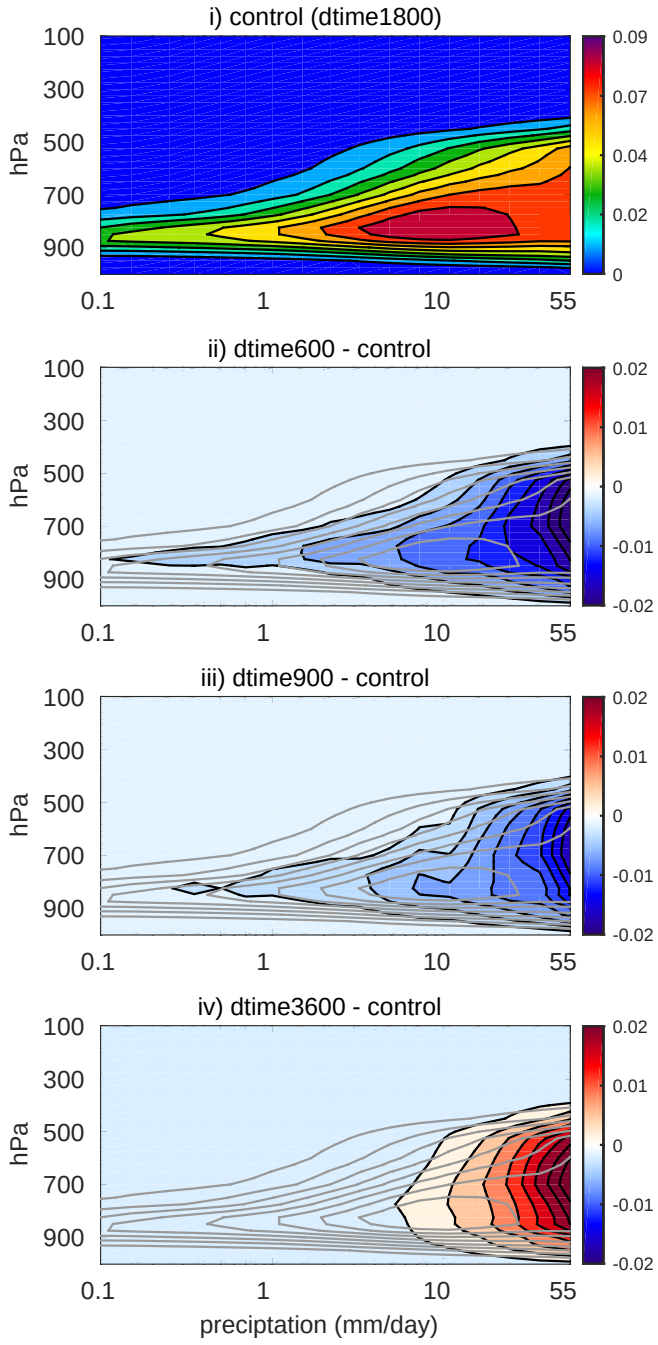

Figure 2.10: The daily precipitation-binned mean liquid condensate profile in an active convective region over ocean, 10°S–10°N, 60°E–170°E. (i) control simulation and (ii–iv) experiment simulation anomalies against control simulation. The grey contour lines in ii–iv show the control simulation contour line in i.

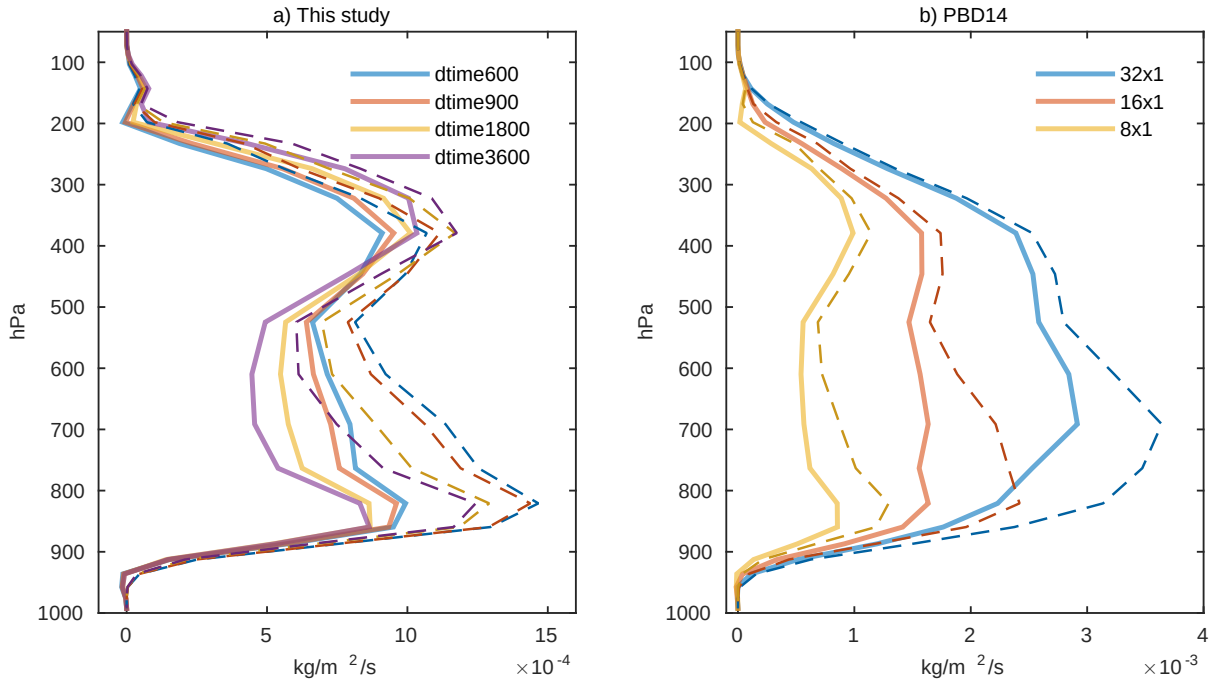

Figure 2.11: The CRM-diagnosed net updraft mass flux—the sum of saturated and unsaturated updraft mass flux components—profiles (solid lines) and their saturated moist components (dashed lines) in (a) this study and (b) PBD14 in tropical convective regions (mean daily precipitation rate > 6 mm/day in 15°S–15°N). Note the different scales on the abscissae in a and b.

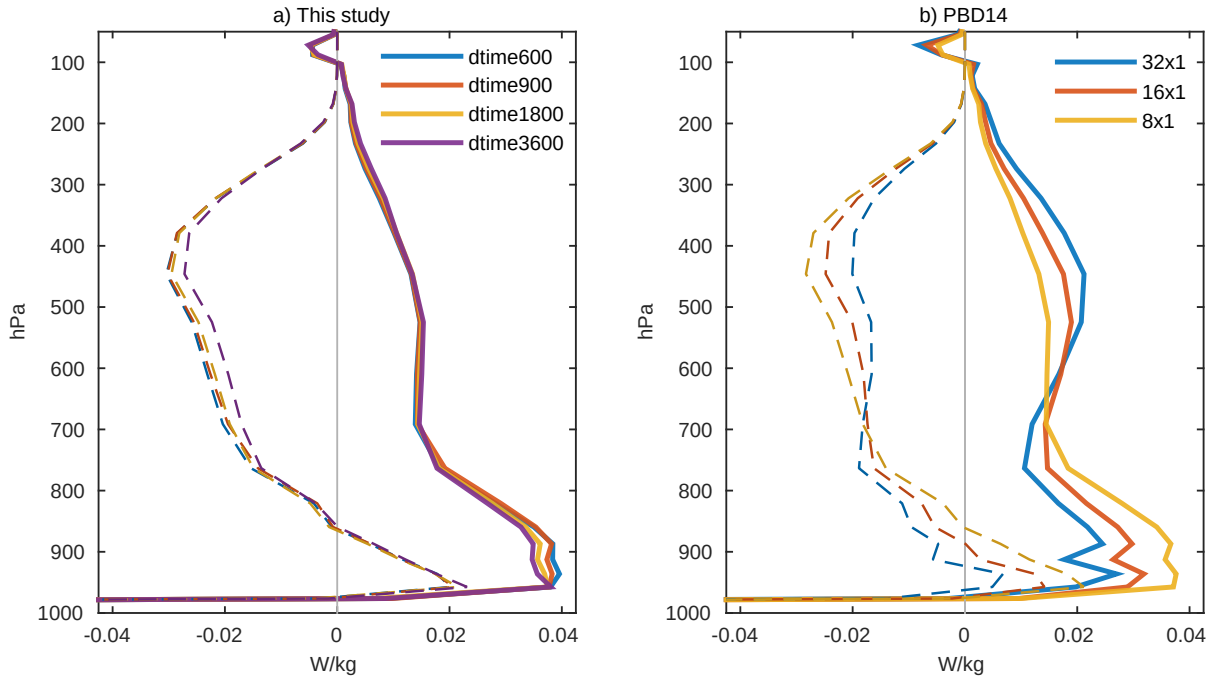

Figure 2.12: The CRM-diagnosed MSE tendency— i.e. $c_p(\partial T/\partial t) + L_v(\partial q/\partial t)$, where T, q, c_p, and L_v are temperature, specific humidity, the specific heat capacity of air, and the specific latent heat of vaporization of water, respectively—profiles (solid lines) and their moist components (dashed lines) in (a) this study and (b) PBD14 in tropical convective regions (mean daily precipitation rate $>$ 6 mm/day in 15°S–15°N).

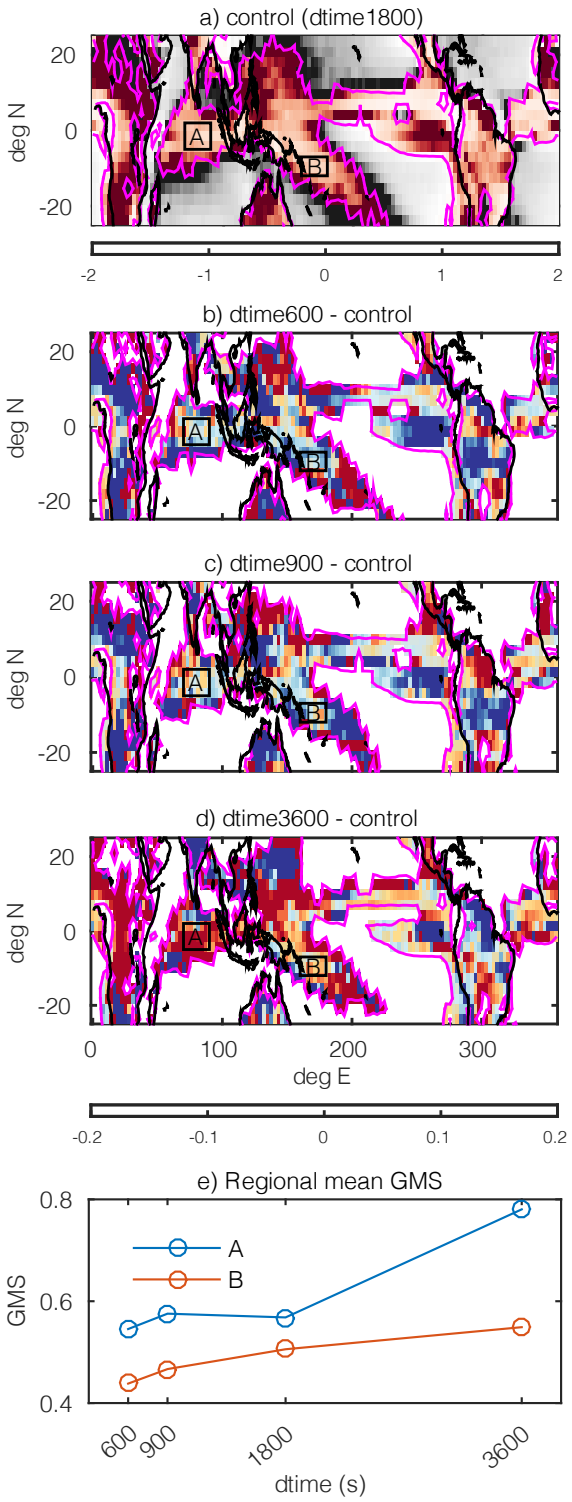

Figure 2.13: Annual mean normalized gross moist stability (GMS) in the control simulation. (a) Control simulation; (b–d) Experimental simulation anomalies against control simulation; and (e) Horizontally-averaged GMS responses in two indicated subregions, A and B. The magenta line shows the contour of GMS of 0.1.

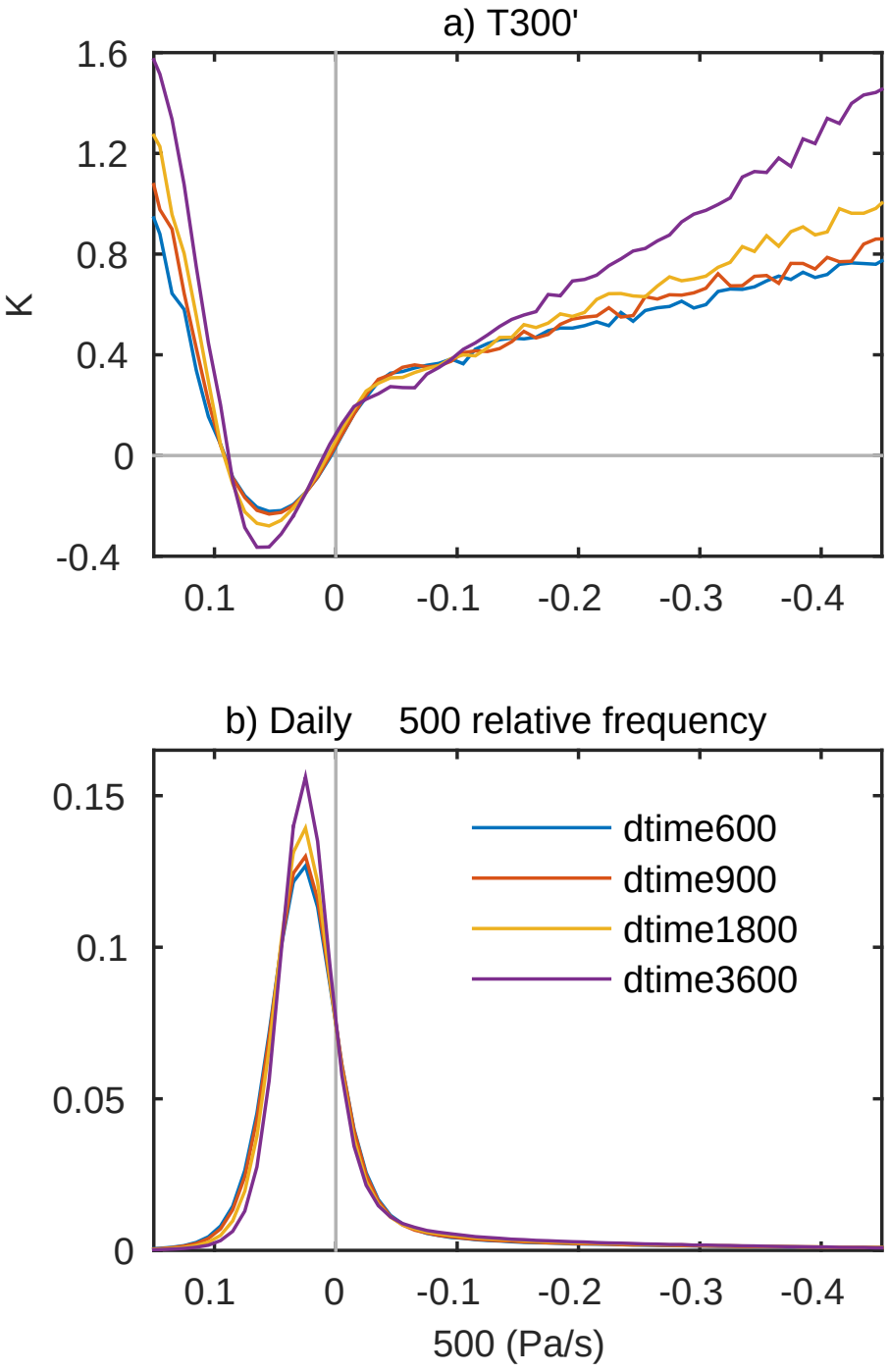

Figure 2.14: (a) Daily horizontal-mean anomalies of temperature from its horizontal field at 300 hPa ($T300'$) across vertical velocity at 500 hPa ($\omega 500$) in equatorial region (5°S–5°N). (b) Relative frequency of vertical velocity at 500 hPa.

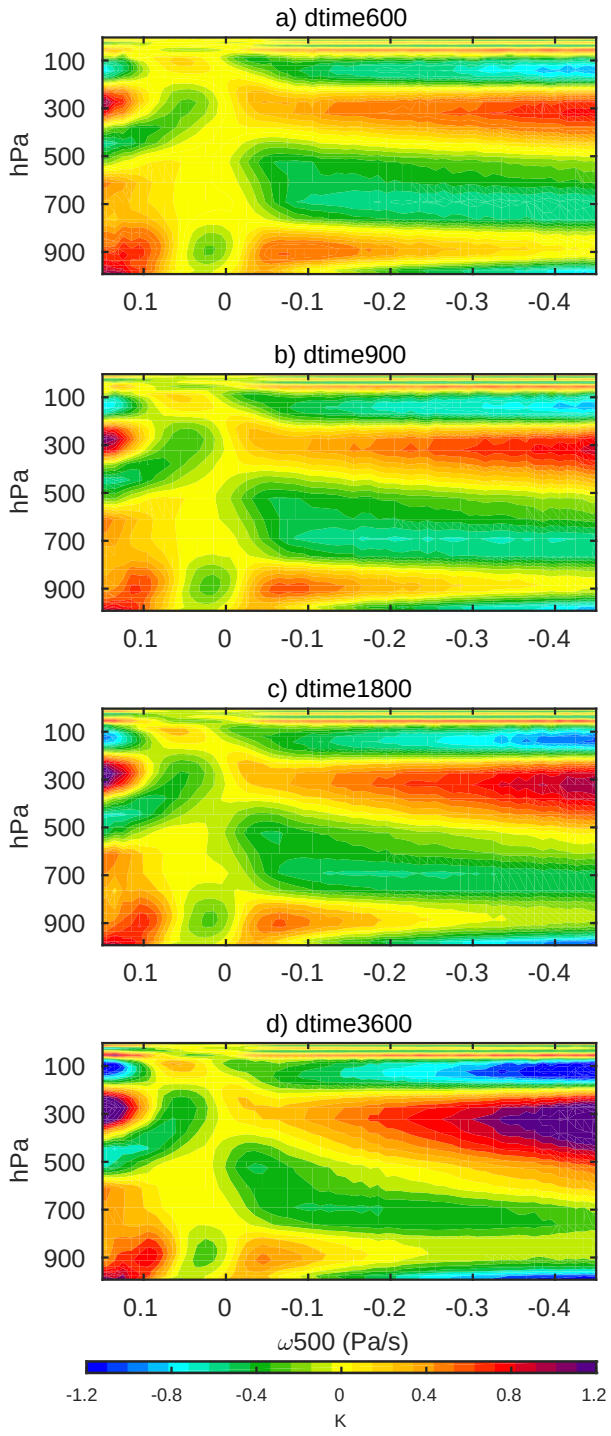

Figure 2.15: Vertically resolved profiles of temperature anomalies from its horizontal mean, binned by vertical velocity at 500 hPa (ω500) in equatorial region (5°S–5°N).

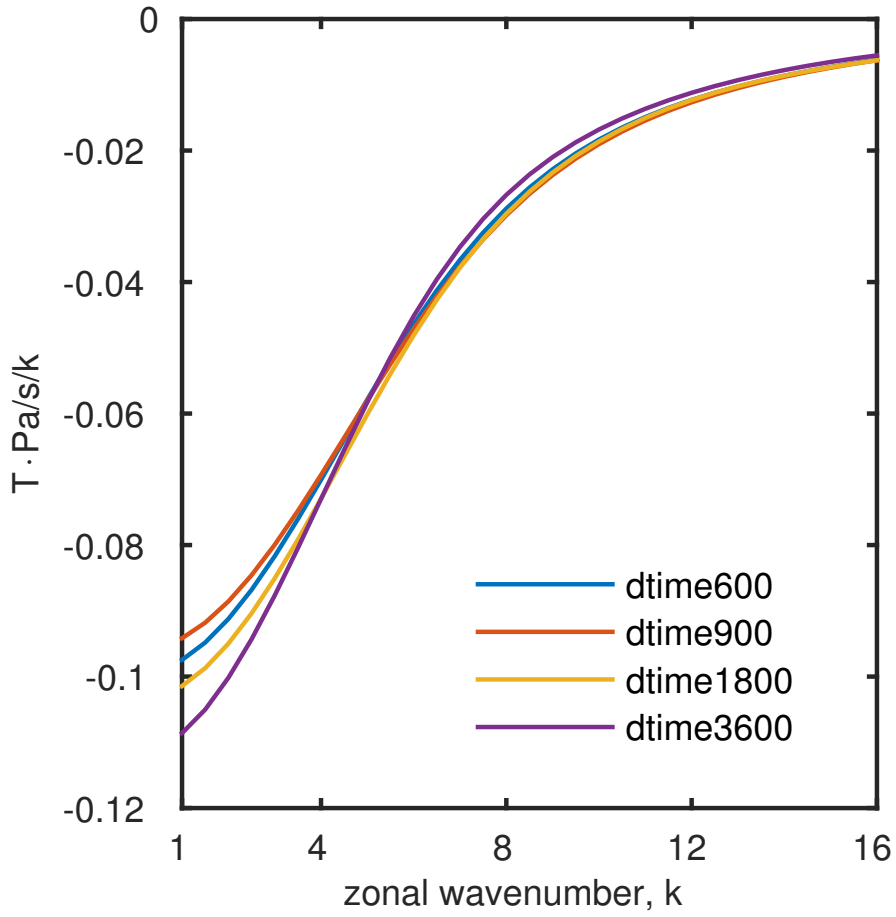

Figure 2.16: Cospectrum of daily temperature anomalies at 300 hPa and vertical velocity at 500 hPa from their horizontal field in equatorial region (5°S–5°N).

Chapter 3

The impact of superparameterization in the double ITCZ bias development

As appears in:

Woelfle, M. D., **Yu, S.**, Bretherton, C. S., and Pritchard, M. S. (2018), Sensitivity of coupled tropical pacific model biases to convective parameterization in CESM1, Journal of Advances in Modeling Earth Systems, 10, 126–144, doi:10.1002/2017MS001176. [1]

Abstract

Six month coupled hindcasts show the central equatorial Pacific cold tongue bias development in a GCM to be sensitive to the atmospheric convective parameterization employed. Simulations using the standard configuration of the Community Earth System Model ver-

[1] This research project was a collaboration between the University of California, Irvine and the University of Washington. Both Woelfle and Yu led and equally contributed to the analysis phase of the project – with Woelfle in charge of CESM simulations and Yu in charge of SP-CESM simulations. Although Woelfle led the writing of this manuscript, its narrative reflects an understanding achieved through collaboration with Yu. An unpublished subset of this research project regarding the cloud resolving model configuration sensitivity of the SP-CESM is shown in Appendix A.

sion 1 (CESM1) develop a cold bias in equatorial Pacific sea surface temperatures (SSTs) within the first two months of integration due to anomalous ocean advection driven by overly strong easterly surface wind stress along the equator. Disabling the deep convection parameterization enhances the zonal pressure gradient leading to stronger zonal wind stress and a stronger equatorial SST bias, highlighting the role of pressure gradients in determining the strength of the cold bias. Superparameterized hindcasts show reduced SST bias in the cold tongue region due to a reduction in surface easterlies despite simulating an excessively strong low-level jet at 1–1.5 km elevation. This reflects inadequate vertical mixing of zonal momentum from the absence of convective momentum transport in the superparameterized model. Standard CESM1 simulations modified to omit shallow convective momentum transport reproduce the superparameterized low-level wind bias and associated equatorial SST pattern. Further superparameterized simulations using a three-dimensional cloud resolving model capable of producing realistic momentum transport simulate a cold tongue similar to the default CESM1. These findings imply convective momentum fluxes may be an underappreciated mechanism for controlling the strength of the equatorial cold tongue. Despite the sensitivity of equatorial SST to these changes in convective parameterization, the east Pacific double-Intertropical Convergence Zone rainfall bias persists in all simulations presented in this study.

3.1 Introduction

While the skill of global climate models has generally increased with increasing resolution and updated parameterization, significant biases in simulating tropical Pacific rainfall and sea surface temperature (SST) patterns remain. Specifically, most global climate models (GCMs) participating in the Coupled Model Intercomparison Project phase 5 (CMIP5; *Taylor et al.* (2012)) simulate a spurious band of precipitation extending into the southeastern tropical

Pacific and a tongue of depressed equatorial sea surface temperatures (SSTs) spanning most of the basin (*Li and Xie*, 2014).

In observations, precipitation in the tropical Pacific is concentrated into two regions: a zonal band of convection spanning the basin near 7°N known as the Intertropical Convergence Zone (ITCZ) and a second band of convection extending southeast from the maritime continent into the south-central Pacific known as the South Pacific Convergence Zone (SPCZ). While the observed ITCZ migrates seasonally with a southern hemispheric maximum in March and April (*Mitchell and Wallace*, 1992; *Waliser and Gautier*, 1993; *Zhang*, 2002), observed zonal mean annual mean precipitation exhibits a single northern hemispheric maximum which coupled GCMs struggle to reproduce (*Li and Xie*, 2014; *Lin*, 2007). In a study examining earlier versions of coupled GCMs, *Mechoso et al.* (1995) described the canonical double-ITCZ bias as occurring when the simulated SPCZ is too zonally oriented and extends too far into the southeast Pacific leading to a spurious southern hemispheric precipitation maximum in the zonal annual mean. The presence of a local, annual mean precipitation maximum in each hemisphere is the hallmark of the so-called double-ITCZ bias, and it can be found in most modern GCMs (*Li and Xie*, 2014; *Lin*, 2007).

In addition to the excess southern hemispheric rainfall, simulated precipitation along the equator is also weaker in GCMs than observations, despite GCMs simulating too much precipitation overall in the tropics (*Lin*, 2007). The equatorial dry bias is collocated with a cold bias in SST that extends from the east Pacific to the edge of the west Pacific warm pool (*Li and Xie*, 2014). This SST bias is commonly referred to as the Pacific cold tongue (CT) bias. Both the double-ITCZ and CT biases have persisted for decades in simulations of the tropical Pacific despite improvements to resolution and updated representation of physical processes through improved parameterizations (*Lin*, 2007; *Mechoso et al.*, 1995; *Zhang et al.*, 2015). These biases can develop within months in realistically initialized coupled models (*Liu et al.*, 2012), so they are important for seasonal forecasting as well as climate simulations.

Many attempts to ameliorate the double-ITCZ and CT biases have focused on the role southeast Pacific clouds and SSTs play in setting the location of deep tropical convection and in determining the strength of the equatorial cold tongue (e.g. *de Szoeke et al.*, 2006; *Ma et al.*, 1996; *Yu and Mechoso*, 1999). *Yu and Mechoso* (1999) used prescribed clouds to show the strength of the equatorial cold tongue is sensitive to cloud radiative forcings over the southeast Pacific. *de Szoeke et al.* (2006) extended this result to a coupled regional climate model where low cloud was increased by disabling the parameterization for nonprecipitating shallow cumulus clouds. This idealized perturbation decreased SSTs and suppressed deep convection in the southeast Pacific, effectively eliminating the double-ITCZ bias. While the modification also suppressed the observed seasonal migration of the ITCZ, the result serves to further highlight the sensitivity of the coupled system to cloud parameterizations in this region.

More recent studies have expanded on the role of cloud and convective parameterizations in the development of the double-ITCZ bias. Many of these studies suggest the double-ITCZ bias results from deep convection parameterizations being too sensitive to SSTs and too insensitive to inhibitive large-scale dynamic forcings (*Hirota et al.*, 2011; *Oueslati and Bellon*, 2015; *Song and Zhang*, 2009; *Wang et al.*, 2015). The enhanced sensitivity of convection to SST supports a coupled feedback cycle which can amplify otherwise small biases (*Zhang et al.*, 2007b), leading to the development of a double-ITCZ within the first year of integration (*Liu et al.*, 2012).

While coupled feedbacks are important for explaining the full amplitude of the double-ITCZ bias in coupled GCMs, the antecedent bias is generally thought to derive from the atmospheric model. *Xiang et al.* (2017) showed the amplitude of the coupled double-ITCZ bias can be anticipated from the surface flux bias in a corresponding atmosphere-only simulation. Similarly, *Song and Zhang* (2009) attribute the initial bias development to excessive downwelling shortwave radiation. Other studies suggest the double-ITCZ bias arises because

of uncertainty in the entrainment rate leading to deep convection that is too insensitive to large scale subsidence (*Hirota et al.*, 2011), insufficient rain re-evaporation within the deep convection parameterization leading to overly strong coupling between the boundary layer and deep convection (*Bacmeister et al.*, 2006), or overly strong shallow convection leading to an overly moist boundary layer (*Wang et al.*, 2015).

In addition to local processes, remote model biases, such as the downwelling shortwave bias over the Southern Ocean, have been hypothesized to play a role in controlling the location of the zonal mean ITCZ (*Hwang and Frierson*, 2013). This view is consistent with earlier studies in which a model with a slab ocean coupled to a fully dynamic atmosphere was used to demonstrate the ITCZ and associated Hadley circulation shift toward the more energetic hemisphere when a hemispherically asymmetric energy perturbation is applied to the system (*Broccoli et al.*, 2006; *Kang et al.*, 2008, 2009). Such studies imply the improvement of extratropical model biases, e.g., the Southern Ocean cloud bias, may improve the double-ITCZ bias in coupled models. Several, recent studies suggest the role of remote biases in driving tropical precipitation shifts are overemphasized by slab ocean studies, as changes in meridional ocean heat transport tend to dominate the change in atmospheric transport in fully coupled modeling studies (*Kay et al.*, 2016; *Hawcroft et al.*, 2016; *Tomas et al.*, 2016). However, *Mechoso et al.* (2016) show the magnitude of atmospheric response to asymmetric high-latitude heating is underestimated in a coupled model where the tropical SST-stratocumulus feedback is too weak, suggesting the true climate response to asymmetric high latitude heating remains uncertain.

While the double-ITCZ bias is largely considered as driven by the atmospheric component of coupled GCMs, the CT bias is an inherently coupled problem. An overview of the challenges associated with diagnosing coupled model biases can be found in *Zuidema et al.* (2016) and citations found therein. Studies of the CT bias within an earlier version of CESM1, the Community Climate System Model version 3 (CCSM3), suggest overly strong zonal wind

stress from surface easterlies along the equator both advects upwelled Eastern Pacific water to the west and promotes local Ekman induced upwelling, which combine to produce overly cool SSTs across the equatorial Pacific (*Large and Danabasoglu*, 2006). The connection between overly strong zonal wind stress and too cool SSTs is also present in CMIP5 models (*Li et al.*, 2015). Surface fluxes damp the dynamically driven temperature changes, mainly through a reduction in surface latent heat flux. Other studies suggest the cold tongue bias is driven thermodynamically rather than dynamically. These studies suggest cold biases in the subtropical upper ocean are subducted into the subtropical cells. The resulting upwelling of this water along the equator leads to the development of the CT bias (*Li et al.*, 2013; *Vannière et al.*, 2014; *Thomas and Fedorov*, 2017). Paleoclimate studies support the connection between midlatitude and equatorial SSTs (*Burls and Fedorov*, 2014; *Fedorov et al.*, 2015). The two theories for the CT bias development, dynamically driven through upwelling or thermodynamically driven through upwelling of cooler water, suggest vastly different time scales for the development of the biases: months for the development of a dynamically driven bias and years to decades for a thermodynamically driven bias.

The relationship between convective parameterizations and the CT bias has not been as extensively studied as the relationship between convective parameterizations and the double-ITCZ bias, though several studies have examined its impact on simulations of the El Niño–Southern Oscillation (ENSO), the leading mode of equatorial Pacific climate variability. *Neale et al.* (2008) showed that including convective momentum transport by deep convection leads to a less regular ENSO and enhanced zonal wind speed along the equator. Though *Neale et al.* (2008) do not directly discuss the CT bias, the change in equatorial winds suggests convective momentum transport parameterizations may impact equatorial upwelling and thus also SST. *Guilyardi et al.* (2009) showed convective parameterization changes can suppress simulated ENSO events through changes in the amplitude of the shortwave–SST feedback. The strength of the shortwave–SST feedback may also directly affect a model's mean state by acting on other preexisting model biases. More recently, *Zhu et al.* (2017)

used a series of initialized hindcast experiments to show that a change in convective parameterizations within the Climate Forecast System affects ENSO prediction skill through modification of the amplitude of coupled ocean–atmosphere feedbacks along the equator.

In this chapter, we reexamine the role of convective parameterization in the development of both the double-ITCZ and cold tongue biases using short, coupled hindcast model simulations. We first examine the development of the biases in the standard configuration of the Community Earth System Model version 1 (CESM1). We then assess the response of the system to two changes in to the atmosphere model's convective parameterization. First, we perform a sensitivity test in which we disable the deep convection parameterization, thereby forcing all convection to be simulated by the shallow cumulus parameterization. Second, we examine simulations with a superparameterized atmosphere, which replaces all moist physics with output from an embedded two-dimensional cloud resolving model. Finally, a sensitivity test was performed to isolate the role of shallow cumulus momentum transport in determining the hindcast development.

Section 3.2 describes the CESM1 modeling system, the convective parameterizations employed, and details of the model initialization and validation data sets utilized in the study. Results of the simulations are discussed in detail in section 3.3. The chapter concludes with a summary and discussion of the implications of these results in section 3.4.

3.2 Models and Data

3.2.1 Models

Simulations presented in this study were performed using the Community Earth System Model version 1 (CESM1). This fully coupled, state of the art global climate model consists

of fully dynamic atmosphere [Community Atmosphere Model version 5 (CAM5)] and ocean [Parallel Ocean Program version 2 (POP2)] models as well as land [Community Land Model version 4 (CLM4)], sea ice [Los Alamos Sea Ice Model (CICE)], and river routing models [River Transport Model (RTM)]. CAM5 and CLM are run at a horizontal resolution of 1.9°x2.5°. POP2 and CICE are run at nominal 1° resolution with higher resolution near the equator than at the poles. Further details about the CESM1 modeling system can be found in *Hurrell et al.* (2013).

3.2.2 Convective parameterizations

For this study, we ran CAM5 with three different convection and moist physics parameterizations. The first set of simulations utilized the standard configuration of CESM version 1.2.2. In this configuration, deep convection is parameterized using a plume ensemble approach with an additional parameterization for convective momentum transport (*Neale et al.*, 2008; *Richter and Rasch*, 2008; *Zhang and McFarlane*, 1995). Shallow convection in CAM5 is parameterized using a mass-flux scheme combined with a buoyancy sorting algorithm (*Park and Bretherton*, 2009); this scheme also includes a simple representation of convective momentum transport. Simulations run using this set of parameterizations are referred to as the control (CTRL) simulations for the remainder of this chapter.

A simple test of the modeling system's sensitivity to convective parameterization was performed by disabling the deep convection parameterization, which forced all convection to be resolved by the shallow convection parameterization. This modification produces a climate with an elevated fraction of large scale versus convective precipitation as the shallow convection parameterization alone is unable to fully compensate for absence of an explicit deep convection parameterization despite being able to operate on all model levels. Simulations in which the deep convective scheme has been disabled are denoted as NODC. The NODC sim-

ulation still simulates some vertical momentum transport from the shallow convection and moist turbulence parameterizations despite the disabling of the deep convective momentum transport parameterization.

A third set of simulations was run in which all of CAM5's moist physics parameterizations were replaced by a two-dimensional cloud-resolving model (CRM) contained within each grid cell (*Grabowski and Smolarkiewicz*, 1999; *Khairoutdinov and Randall*, 2001; *Wang et al.*, 2011). The CRM used two-moment microphysics (*Morrison et al.*, 2005) and had 32 columns and 30 vertical levels with a horizontal resolution of 4 km. The CRM time step was 20 s whereas the standard physics time step for CAM5 is 1,800 s (30 min). This configuration of CESM1 is known as the superparameterized CESM (SP-CESM). Simulations run with SP-CESM are denoted as SP in this chapter. As in almost all prior implementations of SP, the version of SP-CESM used for this study does not pass momentum tendencies from the CRM to the GCM. Since the additional deep and shallow convective momentum flux computations used in the standard version of CESM1 are disabled, the implication is that convective momentum transport is not represented by SP-CESM, although vertical diffusion of momentum by the PBL turbulence scheme is allowed to operate. The SP-CESM codebase used for this study is Revision 71690 at https://svn-ccsm-models.cgd.ucar.edu/cam1/branches/UltraCAM-spcam2_0_cesm1_1_1/. The version of CESM1 from which our version of SP-CESM was created, CESM1.1, differs slightly from the version of CESM1 used for the CTRL and NODC simulations, CESM1.2. Differences between the versions are slight, mainly consisting of updating parameterizations rather than significant changes to the model code (http://www.cesm.ucar.edu/models/cesm1.2/tags/). Nonetheless, to account for the slight changes in model solution between the versions, a parallel control simulation was run for the SP simulations using the standard version of CESM1.1. This set of control simulations is denoted as NOSP to differentiate them from the CTRL simulations described previously. As the CTRL and NOSP simulations are very similar, results are only shown for the CTRL simulation unless otherwise noted. A summary

of all model simulations used in this chapter, including sensitivity tests described in section 3.3.3, can be found in table 3.1.

Simulation ID	Coupling	CESM version	Convection parameterizations included	
			Deep	Shallow
CTRL	Fully coupled	1.2.2	ZM95*	PB09†
FCTRL	Fixed SST	1.2.2	ZM95	PB09
FNODC	Fixed SST	1.2.2	_	PB09
FNOSP	Fixed SST	1.1	ZM95	PB09
FSP	Fixed SST	1.1	2D CRM (Wang et al.,2011)	
NODC	Fully coupled	1.2.2	_	PB09
NOUWCMT	Fully coupled	1.2.2	ZM95	PB09, CMT‡ disabled
NOSP	Fully coupled	1.1	ZM95	PB09
OCN	CORE forced ocean and sea ice	1.0	_	_
SP	Fully coupled	1.1	2D CRM (*Wang et al.*, 2011)	
SP3D	Fully coupled	1.1	2D CRM (*Wang et al.*, 2011)	
SP3DMOM	Fully coupled	1.1	3D CRM with CMT (*Wang et al.*, 2011)	

Table 3.1: The details of model simulations and their convective parameterizations. ∗: *Zhang and McFarlane* (1995); †: *Park and Bretherton* (2009); ‡: convective momentum transport.

3.2.3 Hindcast initialization and description

Previous studies have shown the double-ITCZ bias development to begin within the first year of integration in the CCSM3 modeling system, a predecessor to CESM1 (*Liu et al.*, 2012). Here we examine the rapidly developing component of the double-ITCZ and CT biases within the fully coupled GCM CESM1. Using hindcast simulations, we are able to compare simulated fields to observed and reanalyzed fields enabling more thorough analysis of the transient bias development. To increase confidence in the fidelity of the early parts of the simulations and to minimize the impact of initialization shocks, we use the following initialization procedures.

Coupled model simulations are initialized on the first of January in three different years: 1981, 1986, and 1991. The initial conditions for the atmosphere model are computed from

the European Center for Midrange Weather Forecasting's ERA-Interim (ERAI) reanalysis (*Dee et al.*, 2011) interpolated to the CAM5 grid. A three-member ensemble of coupled simulations is created for each start date by introducing random noise of order 10^{-4} K to the atmospheric temperature initial conditions. The land initial conditions are taken from a standalone CLM simulation forced by atmospheric forcings from *Qian et al.* (2006). The land model is run with satellite prescribed phenology and is spun up for five years prior to coupled initialization. The ocean and sea ice initial conditions are taken from a standalone simulation forced with four full cycles of the 60-year long CORE version 2 forcings (*Large and Yeager*, 2009). This standalone simulation is nearly identical to the standalone simulation described in *Yeager and Danabasoglu* (2014) and *Yeager* (2015). We take ocean initial condition files from the appropriate dates within the fifth cycling of the CORE surface forcing data set. The CORE forcings are based on a combination of wind and surface fluxes from observations and reanalysis, designed to produce upper ocean and sea ice states that are nominally in balance with cotemporaneous atmospheric forcings.

After initialization, the fully coupled model is run freely for 6 months. This allows for sampling across various ocean and atmospheric initial states. The atmosphere component is run forward in a standalone configuration from the coupled initialization date using prescribed SSTs from the merged Hadley Center sea ice and SST data set version 1 and National Ocean and Atmosphere Administration optimum interpolation SST version 2 product used in the Atmospheric Model Intercomparison Project simulations (*Hurrell et al.*, 2008). Ocean and sea ice only simulations used for comparison in this study are denoted as OCN for the remainder of this chapter. The OCN simulations are subsets of the simulation from which the ocean and sea ice states were taken for coupled initialization (*Yeager and Danabasoglu*, 2014; *Yeager*, 2015). While the standalone ocean–sea ice simulation includes weak salinity restoring, temperatures were allowed to evolve freely.

3.2.4 Validation data sets

Modeled precipitation fields are compared to the Global Precipitation Climatology Project (GPCP) version 2.1 (*Huffman et al.*, 2009). Ocean properties are compared to the Simple Ocean Data Assimilation version 2.2.4 (SODA2; *Carton and Giese*, 2008; *Giese and Ray*, 2011). SODA2 is produced by forcing POP2 with surface wind stress, insolation, specific humidity, cloud cover, 2 m air temperature, precipitation, and 10 m wind speed from the 20CRv2 data set. The reanalysis system used to produce SODA2 assimilates subsurface temperature and salinity from the World Ocean Database 2009 (*Boyer et al.*, 2009) and sea surface temperatures from ICOADS version 2.5 (*Woodruff et al.*, 2011). Surface momentum fluxes are compared against both CORE2 (*Large and Yeager*, 2009) and SODA (which uses a different surface forcing data set than CORE2). Atmospheric variables are compared to ERAI (*Dee et al.*, 2011).

3.3 Results and Discussion

3.3.1 Rapidly developing bias characteristics

Figure 3.1a shows the mean precipitation over the tropical Pacific from GPCP for the period covering our first hindcast ensemble, January to June 1981. Mean precipitation for the 1986 and 1991 ensembles are similar to those for the 1981 ensemble and are shown in figure 3.2 and figure 3.3, respectively. For the 1981 ensemble, the observed intertropical convergence zone spans the Pacific basin near 8°N, while the observed south Pacific convergence zone extends southeastward from the maritime continent. We define the western edge of the equatorial Pacific dry zone as the easternmost longitude at which the mean precipitation between 2°S and 2°N exceeds 2 mm/d. In observations, this exhibits considerable interannual variability,

with the edge of the dry zone reaching 155°W, 177°W, and 160°W in the 1981, 1986, and 1991 simulations, respectively.

In the CTRL simulation, the northern hemispheric ITCZ is also near 8°N as seen in figure 3.1b, though the rainfall is more intense than in observations. The SPCZ in the CTRL simulation is too zonal with precipitation in excess of 2 mm/d extending across nearly the entire deep tropical Pacific for all three initialization times. This eastward extension of SPCZ rainfall is characteristic of the double-ITCZ bias. The equatorial dry zone in the CTRL simulation is more expansive than observed with near equatorial precipitation in excess of 2 mm/d limited to longitudes west of 180°. The westward extension of the equatorial dry zone is seen for all initialization times and is coincident with a westward shift of precipitation within the west Pacific warm pool.

The double-ITCZ bias has been found to be sensitive to convective parameterization, but surprisingly two key tropical Pacific precipitation features related to the double-ITCZ bias persist in the NODC simulations (figure 3.1c). As in the CTRL simulation, the SPCZ in the NODC simulation is too zonally oriented and extends too far east with mean precipitation rates in excess of 2 mm/d as far east as 100°W. Precipitation along the equator remains suppressed with warm pool precipitation shifted westward. The NODC simulation differs somewhat from the CTRL simulation in that the equatorial dry zone is more meridionally expansive and rainfall within the SPCZ is more intense, while rainfall within the ITCZ is diminished.

The enhanced southeast Pacific rainfall seen in the CTRL and NODC simulations as compared to observations is also present in our 1981 superparameterized hindcast though the bias amplitude is slightly reduced (figure 3.1d). The SP SPCZ is also zonally elongated with precipitation in excess of 2 mm/d present in the southeast Pacific for the 1986 simulations (figure 3.2) though the enhancement is absent from the 1991 simulation (figure 3.3); such similarities between SP and NOSP double-ITCZ rainfall patterns have also been noted in

long coupled simulations (*Kooperman et al.*, 2016). Notably, unlike in CTRL or NODC, near equatorial precipitation in excess of 2 mm/d reaches the dateline in all SP simulations. While the dry zone terminus is still west of its observed location, SP shows improvement in this region over both the CTRL and NODC simulations. This improvement is also associated with an equatorward shift in both the ITCZ and SPCZ with the change to superparameterization.

The precipitation responses to altered convective parameterization in our fully coupled hindcasts, especially related to the meridional extent of the equatorial dry zone, are poorly captured in similar hindcasts using prescribed sea surface temperatures (SSTs) (figure 3.4). The inability of the prescribed SST simulations to capture these changes suggest the precipitation response is mediated through coupling with the upper ocean rather than being forced directly by the changes in convective parameterization.

The six-month mean SST for the period January to June 1981 from SODA is shown in figure 3.5a. Mean SSTs for 1986 and 1991 are qualitatively similar and are shown in figure 3.6 and figure 3.7, respectively. Unsurprisingly, the SST patterns are qualitatively similar to the precipitation patterns shown in figure 3.1a: mean SST is higher in the west Pacific than in the east and is also higher in the northeast Pacific than in the southeast Pacific. There is also a local minimum in SST along the equator which is coincident with the equatorial dry zone. This region of cool SST results from Ekman-driven upwelling of cool subsurface water.

Before looking at SSTs in the fully coupled simulation, we examine an ocean-only hindcast (OCN) to assess the ocean model's ability to reproduce the observed SST field when driven by realistic surface temperature, humidity, and winds. Weak salinity restoring is used in these simulations, but temperatures are allowed to freely evolve. As seen in figure 3.5b, the OCN simulation reproduces the observed SST pattern relatively well with an RMSE of 0.43 K over to tropical and subtropical Pacific basin (30°S–30°N), but with some imperfections that highlight nuances and limitations of current data sets available for ocean model initialization in coupled hindcasts. Most of the tropical Pacific basin is warmer in the OCN simulation

than in SODA though there is a region of depressed SST in the northeast corner of the basin. Along 10°N, positive surface wind stress curl drives upwelling and ridging of the thermocline (not shown). This results in an eastward geostrophic surface current known as the North Equatorial Countercurrent (NECC) along the ridge's southern flank. The wind stress curl and consequently the NECC are both present in SODA. However, the CORE data set, which is used to force the OCN simulation does not accurately represent the positive wind stress curl along 10°N (*Tseng et al.*, 2016). As a result, the thermocline ridge and NECC are poorly simulated in the OCN simulation (figure 3.8). The advectively driven cold bias is damped by a reduction in surface latent heat flux due to the prescribed forcings. Even though the fully coupled simulations are initialized with this NECC bias, they partially recover by developing a thermocline ridge near 10°N and a NECC by the third month of integration, though both are weaker than seen in SODA.

There is considerable sensitivity of SSTs to convective parameterization, particularly within the strongest cold bias found along the equator from 160°E to 95°W of the CTRL simulation (figure 3.5c). The overly cool SST along the equator is characteristic of the development of the Pacific cold tongue (CT) bias. Partly due to the development of the CT bias, the RMSE with respect to SODA increases to 0.67 K in the CTRL simulation. The amplitude and meridional extent of the equatorial cooling is enhanced in the NODC simulation (figure 3.5d). This enhancement contributes strongly to the SST RMSE increase to 0.80 K for the NODC hindcast. The magnitudes of the warm biases are also reduced, due in part to basin-wide cooling in the NODC simulation as compared to the CTRL simulation of 0.8 K to 1.0 K depending on initialization year.

Interestingly, SP appears to significantly reduce the CT bias. In contrast to the CTRL and NODC simulations, the SP simulation does not simulate a zonally extensive cold bias along the equator (figure 3.5e) leading to its improved RMSE of 0.57 K. Rather, the equatorial Pacific is cooler than SODA to the west of 150°W and generally warmer than SODA east of

150°W. The warm bias between 10°S and 20°S is still present in the SP simulation.

We have established that the strength of the CT bias development in CESM1 is sensitive to the atmospheric convective parameterization. To quantify this sensitivity, we define a Pacific cold tongue index as the mean SST over the central Pacific cold tongue region (180° to 140°W; 3°S to 3°N; black box in figure 3.5c) minus the mean SST averaged over the greater the tropical Pacific basin (150°E to 110°W; 20°S to 20°N; dashed box in figure 3.5c). Subtracting the mean tropical Pacific SST from the cold tongue SST removes the effect of mean tropical Pacific SST drift from the index. This allows for comparison of the cold tongue bias strength across simulations despite a drift in mean SST, which can become an issue in the NODC and SP simulations since they have not been retuned to minimize climate drift.

Figure 3.9 shows the evolution of the cold tongue index for all three 6 month periods of integration for all simulations and SODA. The ensemble members and ensemble means are included for the fully coupled simulations. For all three start dates, the CT index for the OCN and SP simulations remain within 0.8 K of the observed CT index with a mean bias of 0.22 K and 0.02 K, respectively, across all three integration periods. By contrast, the CT index in the CTRL and NOSP simulations drifts cold within the first month of integration for all start dates, reaching a maximum in the third month of integration then stabilizing. Regardless of initialization date, the NODC simulation produces the largest CT bias with a mean bias of 1.38 K with respect to observations.

3.3.2 Cold tongue bias development

The CT biases can be analyzed using the upper ocean heat budget over the cold tongue region. We compute a budget for the upper 100 m ocean heat content (OHC_{100}) from 180° to 140°W and 3°S to 3°N (solid box in figure 3.5c). OHC_{100} from SODA averaged over January to June 1981 is shown in figure 3.10a for comparison with the SSTs shown in figure 3.5a.

The general structure of warmer water in the west Pacific and cooler temperatures along the equator and in the east Pacific is well captured. There are two regions of locally cooler temperatures in OHC_{100} not seen in the SST field: across the basin along 10°N and in the far east Pacific, east of 120°W. The cooler temperature in these regions is due to shoaling of the thermocline to depths less than 100 m. This results in cooler waters from below the mixed layer being included in the calculation of OHC_{100}. The impact of shoaling associated with imperfect ocean initialization of the NECC is seen clearly in the strong warm bias in the OCN simulation along 10°N as compared to SODA (figure 3.10b). This is the result of the missing thermocline ridge discussed in section 3.3.1. This warm bias persists in all of the fully coupled simulations as the developing thermocline ridge in the fully coupled simulations is still weaker than seen in SODA (figure 3.8). The strong warm bias east of 120°W in the SP simulation is due its overly deep thermocline in this region.

Despite the differences between the OHC_{100} and SST biases in regions of thermocline shoaling, the bias structure in the central equatorial Pacific is similar across the two fields. The OCN simulation exhibits a slight warm bias (0.23 K) along the equator (180°E–220°E) as compared to SODA. The CTRL and NODC simulations both exhibit equatorial cold biases of 1–2 K. The SP simulation shows a weak cold bias centered at 180° longitude that is less zonally extensive than that seen in the CTRL simulation. As the cold tongue bias characteristics are similar between SST and urn:x-wiley:19422466:media:jame20530:jame20530-math-0002 we can use a budget analysis of OHC_{100} to better understand the drivers of the SST bias in this region.

The upper 100 m ocean heat budget is as follows:

$$\frac{d}{dt}OHC_{100} = c_{p,ocn}\frac{d}{dt}[\rho_{ocn}T] = \dot{Q}_{sfc} + [\dot{Q}_{adv}] + [\dot{Q}_{phys}] \tag{3.1}$$

where $c_{p,ocn}$ is the heat capacity of ocean water, taken to be 3,996 J/kg/K; ρ_{ocn} is the density

of ocean water which is taken from the model output; T is the mean ocean temperature. Depth averaging over the upper 100 m is indicated by square brackets. The heating tendencies consist of net surface heat flux, $\dot{Q}_{sfc}$, net advection, $\dot{Q}_{adv}$, and ocean physics, $\dot{Q}_{phys}$, which is computed here as a residual and includes the effects of parameterized vertical diffusion, baroclinic eddies, and isopycnal mixing. The net surface heat flux is the sum of surface turbulent and radiative heat fluxes. Shortwave fluxes through the bottom of a layer are considered in computing the net surface heat flux. The advective heating term is the sum of the zonal, meridional, and vertical advection tendencies:

$$\dot{Q}_{adv} = \dot{Q}_{adv,x} + \dot{Q}_{adv,y} + \dot{Q}_{adv,z} = -u\frac{\partial}{\partial x}(\rho_{ocn}T) - v\frac{\partial}{\partial y}(\rho_{ocn}T) - w\frac{\partial}{\partial z}(\rho_{ocn}T) \tag{3.2}$$

where $\dot{Q}_{adv,x}$, $\dot{Q}_{adv,y}$, and $\dot{Q}_{adv,z}$ are the zonal, meridional, and vertical components of the advective heat flux, respectively; u, v, and w are the zonal, meridional, and vertical velocities, respectively. For our study, the advective flux is not computed directly from model outputs of temperature, density, and velocity as suggested in equation (3.2). These fields are only available as monthly means for the OCN simulation, but sub-monthly transients are important particularly for meridional heat advection. However, the model does output the component-wise net heat flux through each grid box boundary, e.g., $\boldsymbol{u}T$ where $\boldsymbol{u}$ is the zonal ocean velocity vector. These quantities can be used to derive the advective flux by subtracting the heat transport due to a reference flow that accounts for mass convergence in a given direction, e.g.,

$$\dot{Q}_{adv,x} = c_{p,ocn}\left(-\frac{\partial}{\partial x}\overline{\rho}_{ocn}\overline{uT} - \left(-\overline{\rho}_{ocn}\overline{T}\frac{\partial}{\partial x}\overline{\boldsymbol{u}}\right)\right) \tag{3.3}$$

where $\overline{[\ldots]}$ on the right hand side of the equation indicates a monthly mean at a given grid point. Similar equations are used to compute the meridional and vertical advection terms. The computation presented in equation (3.3) agrees well with advective fluxes computed from daily outputs of temperature and velocity from the fully coupled simulations. For

consistency, monthly means are also used for all other budget terms. To reduce numeric losses, all heat budget terms are computed on the native ocean model grid. As POP uses a shifted northern hemisphere grid, the modeled fluxes in the northern hemisphere are truly in the model grid x- and y-direction rather than being directly along lines of constant latitude or longitude. However, as the budget terms we examine are near the equator, the direction correction is small and can be neglected. Previous studies suggest ocean advective processes are responsible for the CT bias development in fully coupled GCMs (*Li et al.*, 2015; *Thomas and Fedorov*, 2017). Figure 3.11a shows the difference in the OHC_{100} budget between the CTRL and OCN simulations over the cold tongue region for all modeled years. Consistent with the rapid initial decline in the CTRL cold tongue index relative to SODA/OCN shown in figure 3.9, the CTRL-OCN anomaly in net upper ocean heat flux is strongly negative for the first two months of integration with net cooling in excess of 50 W/m2 for all initialization dates. The rapid initial cooling is driven by the net advective tendency whose components are shown in figure 3.12a. In 1981 and 1991, the increased advective cooling is the result of increased zonal advection while in 1986, the cooling results from enhanced upwelling. The difference in net surface heat flux between the OCN and CTRL simulations is weakly negative at the start of the simulations but shows no consistent sign through the continued simulation. Thus, net surface fluxes weakly aid the development of the cold tongue bias in the first month of integration but have little net effect on the bias development as the simulations progress. The contribution of ocean physics to the cold tongue bias development is also small compared to the initial effect of the advective fluxes.

When the deep convection parameterization is disabled, the cold tongue bias worsens. The associated difference in the OHC_{100} budget between the NODC and CTRL simulations is shown in figure 3.11b. The cold tongue bias develops and intensifies strongly within the first three months of integration for the 1986 and 1991 simulations and more gradually in 1981. As with the difference between the OCN and CTRL simulations, the additional cooling in the NODC simulation is driven by advective processes, primarily enhanced upwelling with

smaller contributions from zonal and meridional advection (figure 3.12b). After month 3, the advective fluxes switch from net cooling to a net warming tendency, which is balanced by a combination of surface flux and ocean physics driven cooling.

In contrast to the NODC simulation, the SP simulation exhibits a weakened cold tongue bias as compared to its respective control simulation, NOSP (figure 3.9). Unlike in the NODC simulation, the advective flux anomalies in the first three months of the SP simulation are not of uniform sign. While the SP simulation shows reduced cooling due to zonal advection throughout the integration period (figure 3.12c), this warming is strongly compensated by enhanced equatorial upwelling. Surface flux differences between the SP and NOSP simulations are weakly negative, contributing a slight tendency toward an enhanced cold tongue bias. The net OHC_{100} change with respect to the NOSP simulation is highly variable across simulation start dates, with the 1981 simulation showing a general warming tendency while the 1986 simulation experiences stronger cooling in SP than NOSP for months two and three. Some of the variability between ensemble start dates is driven by the relative severity of the NOSP cold tongue bias: the NOSP bias is strongest in 1981; this is also the year SP shows the greatest improvement.

We next discuss the mechanisms behind the changes in the advective fluxes and the relationship between these fluxes and the convective parameterization employed. Ocean circulations are driven by momentum and buoyancy exchanges with the overlying atmosphere. Buoyancy-driven circulations operate on time scales much longer than the length of the simulations presented here. Thus, this discussion will focus on the response of the near-surface wind-driven ocean circulation.

Figure 3.13a shows the meridional mean zonal wind stress over the equatorial central Pacific (3°S to 3°N) for the first two months of integration of the 1981 ensemble alongside the SODA and CORE data sets. This corresponds to the period of strongest advective biases between the OCN and CTRL simulations (figure 3.11a). In this region, the CORE data set exhibits

weaker easterlies than the SODA data set west of 150°W and stronger easterlies east of this longitude. Despite this difference, the CT index in the CORE-forced OCN simulation is similar to that of SODA (figure 3.9). Figure 3.13b shows the difference in near-equatorial zonal wind stress between the fully coupled simulations and the CORE data set over the same period as figure 3.13a. The CTRL simulation exhibits enhanced easterly wind stress west of 140°W. The enhanced easterlies drive a stronger zonal flow thereby cooling the central Pacific. The enhanced easterly wind stress in the central Pacific of the CTRL simulation is also seen in 1991. In 1986, the enhanced easterlies are shifted to west of 170°E. This interannual variability is likely responsible for the differing importance of zonal advection and upwelling for the formation of the cold tongue bias as seen in figure 3.12a.

In 1981, the NODC wind stress response is similar to that of CTRL (figure 3.13d). Thus, their CT biases are quite similar. However, in the 1986 and 1991 simulations, the zonal wind stress in NODC is much stronger than in CTRL (figure 3.13e–f). Thus, these years see stronger advective cooling (figure 3.12b) and a stronger cold tongue bias. The SP simulations exhibit a similar relationship between equatorial zonal wind stress and CT bias strength. However, the change in wind stress in the SP simulations is opposite in sign to that induced by NODC leading to the greatly improved CT index in the SP simulations.

The mean boundary-layer easterlies along the equator are accelerated by the large-scale zonal pressure gradient and decelerated by surface drag (wind stress). A third important source of boundary-layer zonal momentum is vertical eddy momentum fluxes that mix down stronger easterly momentum from the overlying shallow cumulus layer into the boundary layer (*Stevens et al.*, 2002). Meridional advection of zonal momentum by a cross-equatorial flow and lateral eddy flux convergence of meridional momentum appear to be less important in the boundary layer overlying the central Pacific cold tongue. Thus biases in simulated wind stress biases most likely stem from biases in pressure gradients or in cumulus momentum transport.

The meridional mean of near equatorial surface pressure is shown in figure 3.14. The zonal pressure gradient in the central and west Pacific of the CTRL simulation is stronger than seen in ERAI, consistent with the enhanced zonal wind stress seen in the CTRL simulation in this region. figure 3.14d–f compares the surface pressure response of the NODC and SP simulations to their respective control simulations. The differences in the near equatorial surface pressure field between the NODC and CTRL simulation are qualitatively consistent with the wind stress changes seen in figure 3.13d–f. In 1981, they have similar zonal surface pressure gradients and similar near equatorial zonal wind stresses. In 1986 and 1991, NODC develops a stronger surface pressure gradient resulting in stronger surface wind stresses. Thus, the chain of events leading to the NODC cold tongue amplification is quite simple: disabling the deep convection parameterization enhances the zonal surface pressure gradient, which drives stronger near surface zonal winds, which produces a stronger zonal wind stress on the ocean surface and more oceanic advective cooling. However, this simple chain breaks down when applied to the SP simulations.

Compared to NOSP, the surface pressure response in the SP simulations shows either little change in the zonal pressure gradient (1981) or a slight increase (1986 and 1991) (figure 3.14d–f). This suggests the near equatorial zonal wind stress in SP should be similar to or more easterly than the NOSP simulation, contrary to the weaker wind stress response seen in figure 3.13. This incongruity between zonal winds and zonal surface pressure gradient exists for all initialization years, suggesting an important role for changes in downward eddy momentum fluxes in determining the changes in surface wind stress in the superparameterized simulations, similar to that discussed for the tropical Atlantic in *Zermeño-Diaz and Zhang* (2013).

The vertical profiles of zonal wind in the first month of integration of the fully coupled hindcasts over the equatorial central Pacific (3°S to 3°N and 180° to 140°W) are shown in figure 3.15a–c. The zonal wind is too easterly at all levels in the CTRL simulation as

compared to ERAI. Both the low level jet and the top of the free tropospheric easterlies are too high in CTRL as compared to their location in ERAI. In the free troposphere (700 hPa to 300 hPa), both the NODC and SP simulations show reduced easterlies as a result of a dearth of deep convective momentum transport which brings easterly momentum up from the surface in the CTRL simulation.

Figure 3.15d–f shows an expanded view of the zonal wind profiles below 800 hPa most relevant for surface wind stress. The SP simulations show a strikingly enhanced low level jet near 850 hPa along with reduced zonal wind speed near the surface and increased low level zonal wind shear. While the SP and NODC wind anomalies agree aloft (above 750 hPa), the low level NODC zonal wind profile is similar to that of the CTRL simulation, suggesting SP's enhanced vertical wind shear is due to its lack of shallow convective momentum transport.

The standard configuration of CESM1 includes an explicit convective momentum transport parameterization as part of the deep convection parameterization (*Neale et al.*, 2008; *Richter and Rasch*, 2008) and implicit momentum transport within the shallow cumulus and moist turbulence parameterizations (*Bretherton and Park*, 2009; *Park and Bretherton*, 2009). The similarity in the low level wind gradient in the CTRL and NODC simulations suggest the low level zonal wind gradient is controlled more strongly by the shallow convection parameterization than the deep convection parameterization in this region. Vertical momentum transport in SP-CESM is accomplished through the resolved large-scale circulations within CAM5 and the CESM1 moist turbulence parameterization.

Inclusion of convective momentum transport in an atmospheric GCM accelerates the near surface zonal flow and slows zonal wind speeds above 900 hPa (*Richter and Rasch*, 2008). Similarly, *Zermeño-Diaz and Zhang* (2013) highlight the importance of entraining free tropospheric easterly momentum into the boundary layer for accurately simulating near equatorial easterlies in the tropical Atlantic. In light of these previous studies, the differences between the SP and NOSP simulations seen in figure 3.15 are unsurprising. Thus, while the SP

simulations show improvement in the development of equatorial SSTs, the improvements are likely due to missing processes rather than an improved representation of atmospheric dynamics. More broadly, convective momentum fluxes may be an underappreciated mechanism for controlling the strength of the equatorial Pacific cold tongue.

3.3.3 Sensitivity tests

To confirm shallow convection momentum transport is the main driver of the differences between the SP and NOSP simulations, we performed a sensitivity test using three-member ensembles identical to the CTRL ensembles, except that momentum transport by the shallow convection parameterization is disabled. These simulations are referred to as NOUWCMT. Similar to the change in SP, near equatorial wind stress in NOUWCMT is less easterly than in CTRL as shown in figure 3.16a despite little change in the surface pressure field as seen in figure 3.16b. The NOUWCMT simulations' low-level zonal wind profile shows the same enhanced vertical gradient as the SP simulations (figure 3.15). The change in surface wind produced by this modified profile also shows the same CT bias reduction as the SP simulations (figure 3.16c), confirming the SP CT improvements to be the result of the nonphysical low level zonal wind structure.

Khairoutdinov et al. (2005) showed inclusion of momentum tendencies from embedded three-dimensional CRMs within SP-CAM leads to improvements in tropical rainfall and SST patterns relative to tests that disable the CRMs' momentum tendencies. To test the effect of three-dimensional CMT, we simulated two new 1986 hindcast ensembles using an embedded 8x8-column CRM with the same 4 km horizontal resolution as our standard SP simulation. In the first, SP3D, CRM momentum tendencies are neglected, while in the second, SP3DMOM, these tendencies are fed back to the large-scale model. Due to computational expense, SP3D and SP3DMOM were only run for one month.

The change from SP to SP3D has limited effect on the vertical zonal wind profile, but when the momentum tendencies are included in SP3DMOM the near surface zonal wind speed is enhanced (figure 3.17a). This results from both increased vertical mixing, as indicated by the reduced low level wind shear, and an increased zonal pressure gradient (figure 3.17b). While SP is warmer than NOSP over the first month of integration, this CT bias improvement is weaker in SP3D (figure 3.18). Inclusion of momentum tendencies in SP3DMOM leads to a worsened cold tongue as compared to NOSP, further confirming the SP improvement is achieved through a nonphysical representation of the low level zonal wind.

Finally, to assess the extent to which wind stress changes seen in the coupled simulations are driven by the atmospheric component of the coupled modeling system rather than by coupled feedbacks, we rerun the 1986 hindcasts using fixed SSTs for a lower boundary condition. For the following discussion, all simulations using fixed SSTs rather than a dynamic ocean will be denoted by an F preceding the simulation designation, e.g., FSP is the fixed SST version of the SP ensemble. figure 3.19b shows the surface pressure bias as compared to ERAI for the first month of integration for the fixed SST hindcasts. There is little bias in the SP gradient in the central Pacific, yet the zonal wind profile exhibits the same reduced low level wind speed and enhanced low level jet seen in the fully coupled simulations. The profiles for the FCTRL, FNODC, and FNOSP simulations are also similar to their coupled counterparts as seen in figure 3.19a, confirming the zonal wind profile in these hindcasts is set by the atmosphere alone and does not require coupled feedbacks to develop. Because the wind biases in the fixed SST simulations are unable to force changes in the underlying SSTs, the central Pacific precipitation patterns, which are largely governed by SST gradients (*Lindzen and Nigam*, 1987), do not exhibit the meridional shifts with changes in convective parameterization as was seen in the fully coupled simulations (figure 3.4).

3.4 Discussion and Conclusions

In this study, we showed the rapidly developing east Pacific double-ITCZ rainfall bias in CESM1 to be robust to extreme changes in convective parameterization. However, we also showed the central equatorial Pacific precipitation and cold-tongue (CT) SST biases to be very sensitive to the same changes. Simulations using the default configuration of CESM1 develop a double-ITCZ and cold tongue bias within the first six months of integration. When the deep convection parameterization is disabled (NODC simulations), the model continues to produce a double-ITCZ in the eastern tropical Pacific, and the central Pacific precipitation and CT biases amplify for two of the three initialization ensembles. In contrast, when all moist parameterizations are replaced by embedded cloud resolving models in the superparameterized version of CESM (SP simulations), the southeast Pacific double-ITCZ bias still develops, but the Pacific CT bias severity is greatly reduced leading to improved simulation of precipitation in this region.

In all of our simulations, the changes in cold tongue temperature were driven by changes in vertical and zonal oceanic advective heat fluxes. Given the two-month time scale of the CT bias development, these changes are dynamically driven by changes in the surface wind stress field. The CT bias within the CTRL simulation develops as a result of increased zonal wind stress and an associated increase in zonal advection of cool water from the east Pacific. When deep convection is disabled, the zonal pressure gradient is enhanced, leading to enhanced zonal surface wind stress, which drives increased upwelling. As a result, the NODC simulation developed a worsened CT bias.

The relationship between zonal pressure gradient and surface wind biases found in the CTRL and NODC simulations does not extend to the SP simulations because of changes in the superparameterized model's vertical profile of the zonal wind. The SP simulations lack convective momentum transport, which results in an acceleration of the zonal wind at the

top of the boundary layer, near 850 hPa, and a deceleration of near surface zonal wind speed as surface drag effects are less efficiently mixed upward and thus concentrated in the lowest model levels. That is, free tropospheric easterly momentum is not efficiently mixed downward, as has been previously shown to produce biases in equatorial Atlantic surface winds (*Zermeño-Diaz and Zhang*, 2013). As a result of this nonphysical redistribution of lower level momentum, the CT bias in the SP simulation is artificially improved in our hindcasts. Thus, convective momentum transport is an important control on SST in addition to its previously identified role in determining tropical Pacific precipitation patterns (*Wu et al.*, 2003).

A sensitivity test in which shallow convective momentum fluxes are disabled while all other parameterizations remain active is able to reproduce the change in the lower level zonal wind profile seen in SP and the associated improvement in the CT bias, confirming the lack of convective momentum flux as the main driver of the CT bias improvement seen in the SP simulations. Use of embedded three-dimensional cloud resolving models (CRMs) instead of the standard two dimensional CRMs, produced slightly reduced zonal wind shear and accelerated the near surface wind reducing the CT bias improvement. An additional simulation wherein the momentum fluxes from the three-dimensional CRM were fed back to the large scale model (SP3DMOM) further reduced the zonal wind shear, enhancing the low level winds. As a result, the month one CT bias in SP3DMOM is stronger than in SP further suggesting the SP CT improvement is achieved through nonphysical treatment of atmospheric momentum.

Finally, simulations using prescribed SSTs in place of a dynamic ocean confirm the rapidly developing wind stress response seen in the fully coupled model simulations is primarily due to the atmosphere model rather than the result of coupled feedbacks. Thus, the SST response in the coupled model is likely a response to the altered zonal wind stresses rather than the driver. Because the uncoupled wind structure projects strongly onto the coupled simulations,

this provides an additional, potentially valuable uncoupled benchmark, which may serve to reduce the computational time necessary for coupled model development. Our simulations also suggest the meridional shifts in precipitation seen in the fully coupled simulations result from the rapidly developing coupled-SST bias rather than resulting directly from the wind biases, though further work would aid in confirming this relationship.

While the hindcasts presented in this study demonstrate the importance of both large-scale pressure gradients and vertical momentum transport to the rapid cold tongue bias development in CESM1, further work is necessary to fully understand the role these processes play in determining the climate of longer integrations. Specifically, all simulations presented in this study were initialized during points in both the annual cycle (January) and the interannual ENSO cycle (one to two years prior to an El Niño), when equatorial SSTs are warming in the central Pacific. This may affect the balance of the large-scale pressure gradient and vertical momentum mixing key to determining the modeled surface wind stresses.

To this end, one member of the 1981 ensemble for each model configuration was extended out to encompass five years. The cold tongue index and its components for each of these simulations are shown in figure 3.20. Internal variability along the equator with regards to the ENSO cycle combined with a drift toward cooler SSTs across the tropical Pacific in the NODC and SP simulations swamps the expected response to convection parameterization discussed in this chapter. Extended simulations with more ensemble members may prove enlightening for continued exploration of the impact of connective momentum transport on equatorial Pacific SST biases, particularly for the superparameterized simulations.

The simulations presented in this study suggest convective parameterizations play a large role in determining the mean state of the equatorial Pacific, not only through their impact on atmospheric heating and moistening, but also through their parameterized momentum transport and its effect on surface wind stress. The CTRL and NODC simulations produce low level vertical wind profiles with realistic shapes though the wind speed is slightly too

strong. This suggests the shallow convection and planetary boundary layer physics are sufficient to produce the proper vertical wind profile, but it is the large scale pressure forcing that results in an overly strong mean surface wind, which in turn drives the rapidly developing cold tongue bias. The superparameterized simulations are unable to accurately simulate the vertical wind profile near the equator, serendipitously yielding a weaker surface wind stress that reduces the cold tongue bias and supports the improved central Pacific rainfall climatology noted in *Kooperman et al.* (2016) but for nonphysical reasons. Global rainfall statistics were improved by inclusion of a convective momentum transport parameterization in a superparameterized version of the Weather Research and Forecast model (*Tulich*, 2015). However, as we show here, inclusion of convective momentum transport may uncover other compensating model biases in the superparameterized tropical Pacific, which must be corrected in order to properly simulate the cold tongue–ITCZ complex in this region.

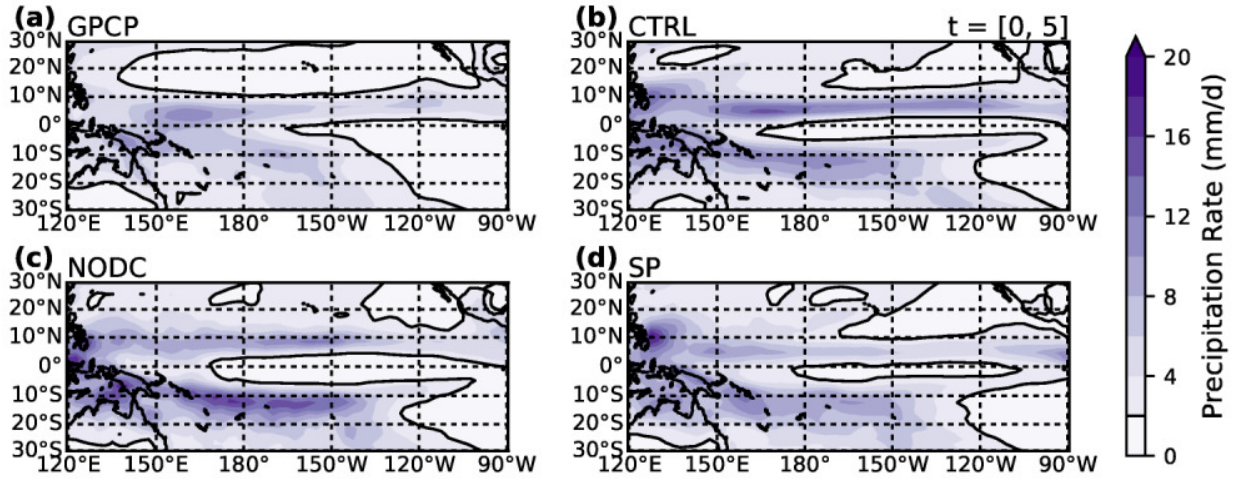

Figure 3.1: Mean precipitation over the tropical Pacific region for January to June 1981 from (a) observations and as simulated in the (b) CTRL, (c) NODC, and (d) SP simulations. The 2 mm/d contour is plotted in black on each panel.

Figure 3.2: Mean precipitation over the tropical Pacific region for January to June 1986 from (a) observations and as simulated in the (b) CTRL, (c) NODC, and (d) SP simulations. The 2 mm/d contour is plotted in black on each panel.

Figure 3.3: Mean precipitation over the tropical Pacific region for January to June 1991 from (a) observations and as simulated in the (b) CTRL, (c) NODC, and (d) SP simulations. The 2 mm/d contour is plotted in black on each panel.

Figure 3.4: Difference in mean January to June 1986 precipitation between (a) NODC and CTRL hindcasts, (b) FNODC and FCTRL hindcasts, (c) SP and NOSP hindcasts, and (d) FSP and FNOSP hindcasts. The 0 mm/d contour is plotted in thin black for reference on each panel. Prescribed (or fixed) SST simulations are denoted by an F preceding the hindcast name.

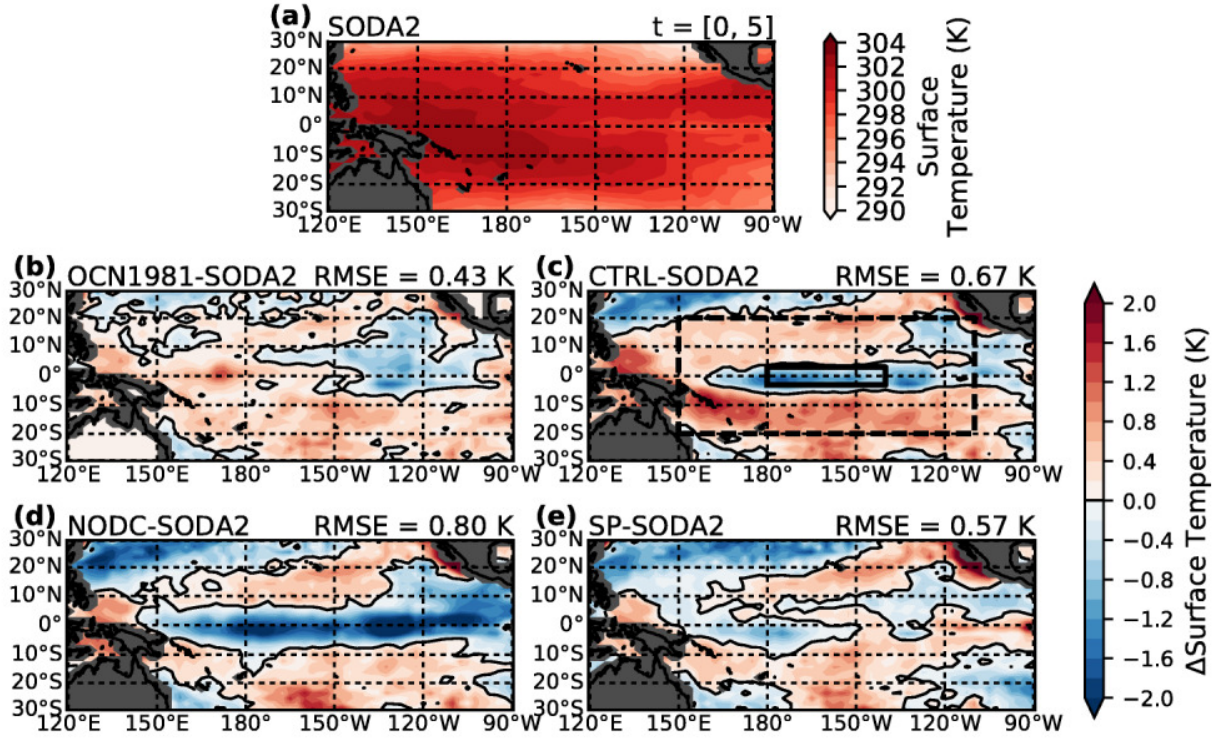

Figure 3.5: (a) Mean sea surface temperature over the tropical Pacific basin for January to June 1981 from observations (SODA). The difference between the (b) ocean only, (c) CTRL, (d) NODC, and (e) SP simulations and the observed temperatures are also shown. The $\Delta T?=?0°C$ contour is plotted in thin black for reference on panels (b–e). The cold tongue index is computed as the difference between the mean SST within the solid black box minus the mean SST within the dashed black box shown in (c).

Figure 3.6: (a) Mean sea surface temperature over the tropical Pacific basin for January to June 1986 from observations (SODA). The difference between the (b) ocean only, (c) CTRL, (d) NODC, and (e) SP simulations and the observed temperatures are also shown. The ΔT=0°C contour is plotted in thin black for reference on panels (b–e). The cold tongue index is computed as the difference between the mean SST within the solid black box minus the mean SST within the dashed black box shown in (c).

Figure 3.7: (a) Mean sea surface temperature over the tropical Pacific basin for January to June 1991 from observations (SODA). The difference between the (b) ocean only, (c) CTRL, (d) NODC, and (e) SP simulations and the observed temperatures are also shown. The ΔT=0°C contour is plotted in thin black for reference on panels (b–e). The cold tongue index is computed as the difference between the mean SST within the solid black box minus the mean SST within the dashed black box shown in (c).

Figure 3.8: Latitude versus depth plot of mean temperature over month six of the 1981 integration for (a) SODA and the (b) OCN, (c) CTRL, (d) NODC, and (e) SP simulations. The black line on each plot highlights the location of the 293 K (20°C) isotherm which is a proxy for the thermocline. The solid white line on each plot is the 293 K isotherm from SODA. The dashed white line in each plot indicates the depth (100 m) over which the ocean heat budgets shown in this chapter are computed.

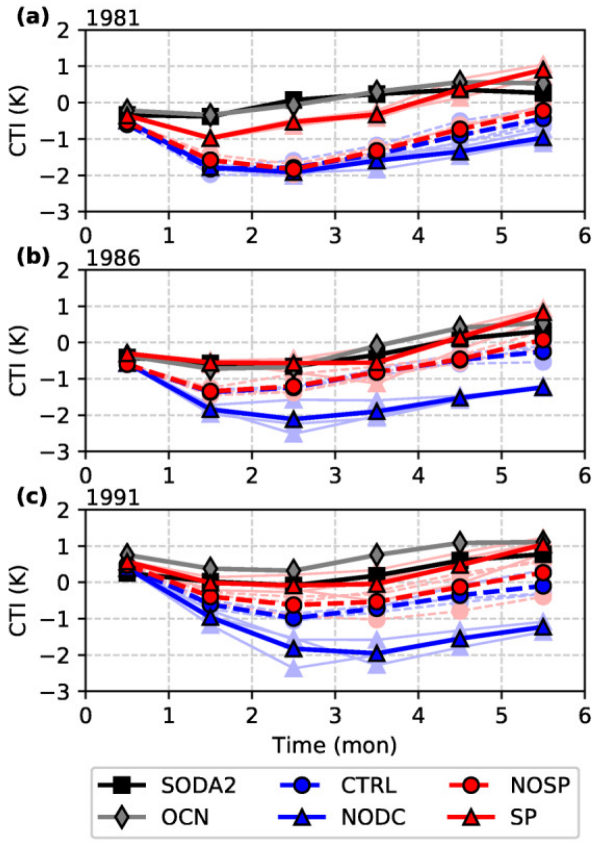

Figure 3.9: Transient evolution of the cold tongue index for all observations and all simulations for simulations initialized on (a) 1 January 1981, (b) 1 January 1986, and (b) 1 January 1991. The cold tongue index is the mean SST in the region 180° to 140°W and 3°S to 3°N minus the mean SST in the region 150°E to 110°W and 20°S to 20°N. Bold lines for CTRL, NODC, NOSP, and SP indicate ensemble means while faded lines show the individual ensemble members.

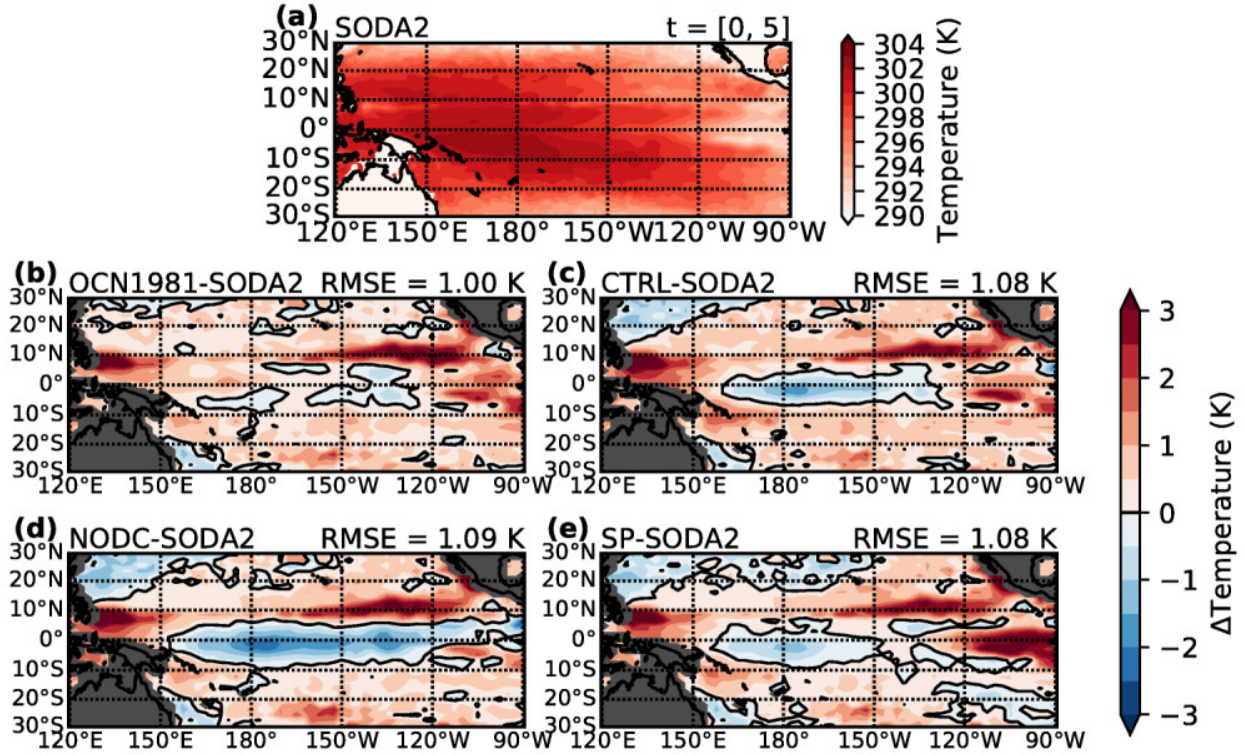

Figure 3.10: Mean upper 100 m ocean temperature over the tropical Pacific basin for January to June 1981 from (a) observations. The difference between the (b) ocean only, (c) CTRL, (d) NODC, and (e) SP simulations and the observed temperatures are also shown. For plots showing differences from observations (figure 3.10b–e), the 0 K contour is shown for reference.

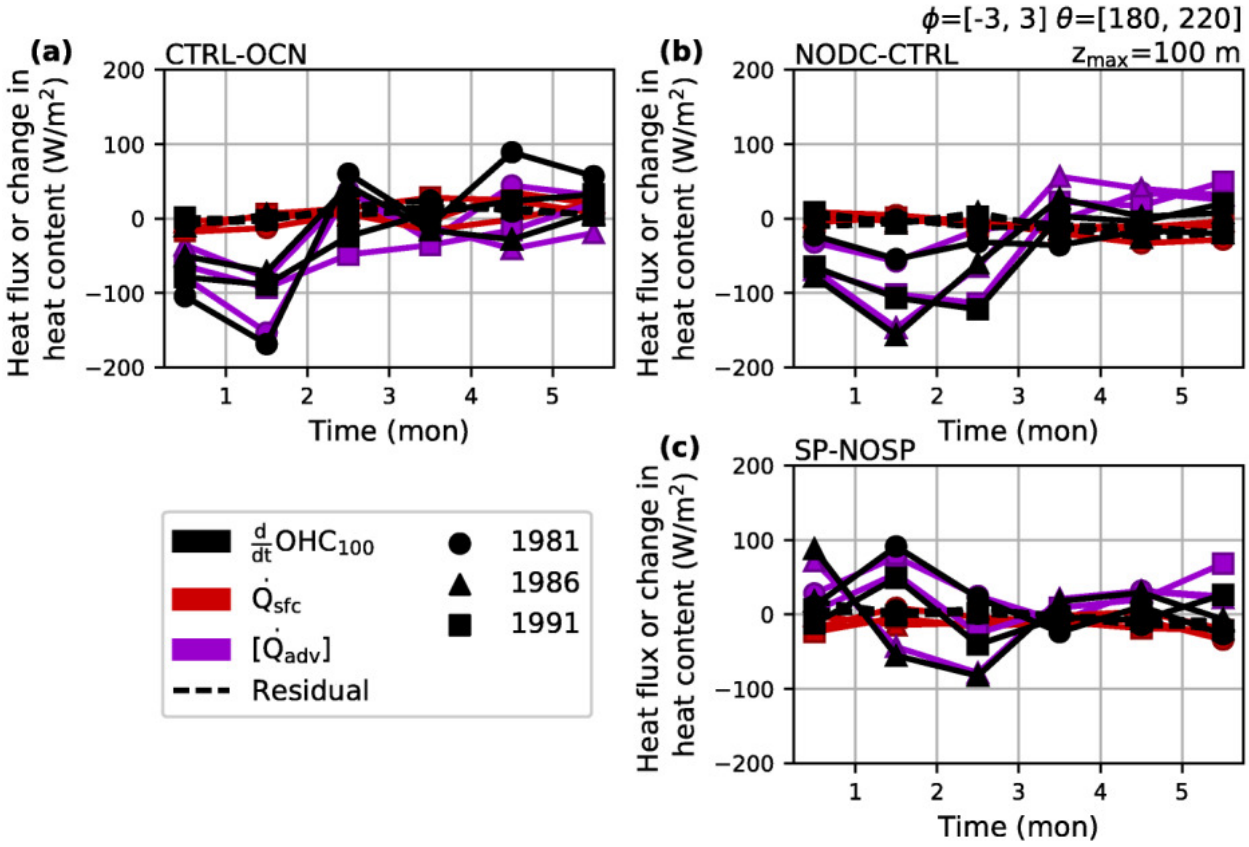

Figure 3.11: Time evolution of ocean heat budget for (a) CTRL minus OCN, (b) NODC minus CTRL, and (c) SP minus NOSP. The time series for 1981, 1986, and 1991 simulations are indicated with a close circled, closed triangle, and closed square, respectively. Ocean physics are shown as a residual of the other budget terms.

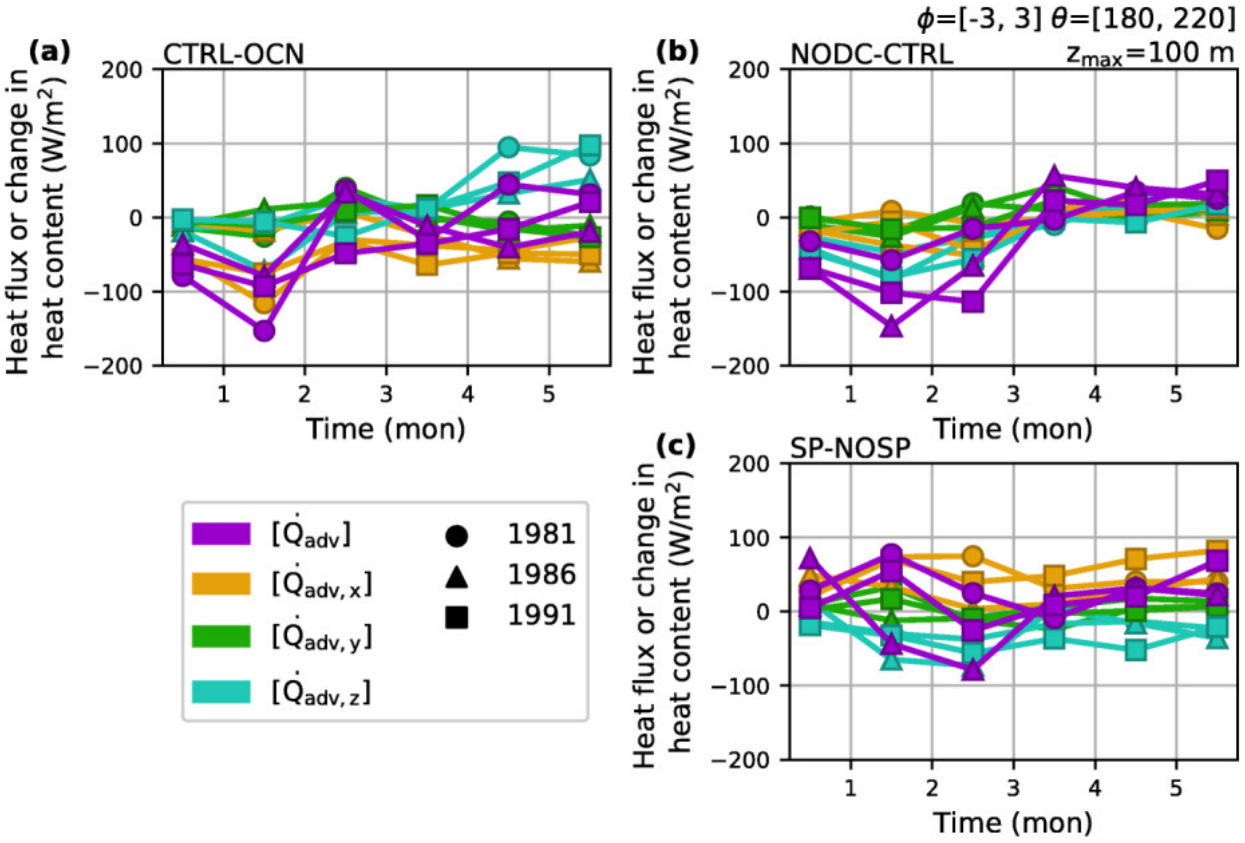

Figure 3.12: Time evolution of ocean advective heat flux terms for (a) CTRL minus OCN, (b) NODC minus CTRL, and (c) SP minus NOSP as a local heating rate over the central equatorial Pacific (3°S to 3°N and 180°E to 220°E). The time series for 1981, 1986, and 1991 simulations are indicated with a close circled, closed triangle, and closed square, respectively. The net advective flux (purple) is the same as on figure 3.11.

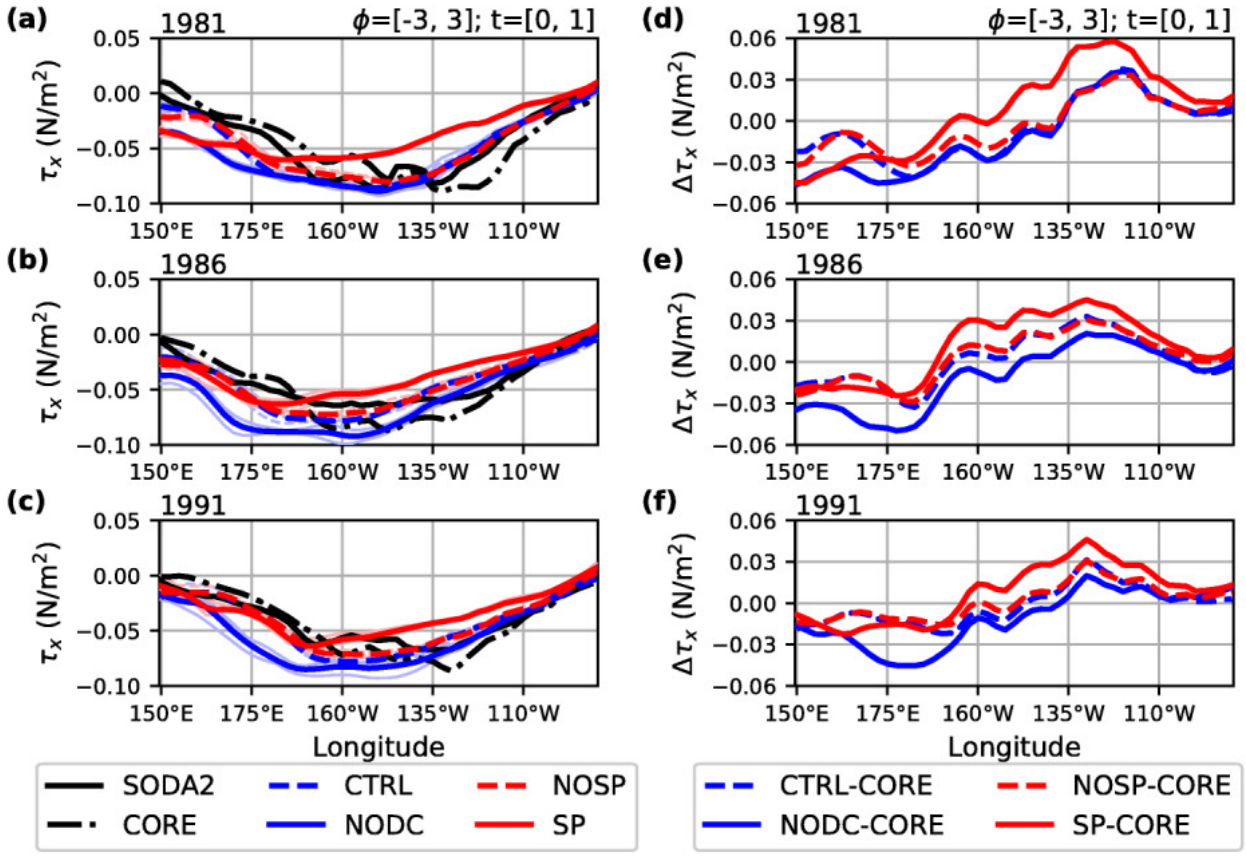

Figure 3.13: January–February meridional mean of zonal wind stress over the near-equatorial (±3° latitude) central Pacific for the fully coupled simulations, SODA, and CORE for (a) 1981, (b) 1986, and (c) 1991. Bold lines show ensemble means or observations. Faded lines show ensemble members. Difference between fully coupled ensemble means and CORE data set are shown for (d) 1981, (e) 1986, and (f) 1991.

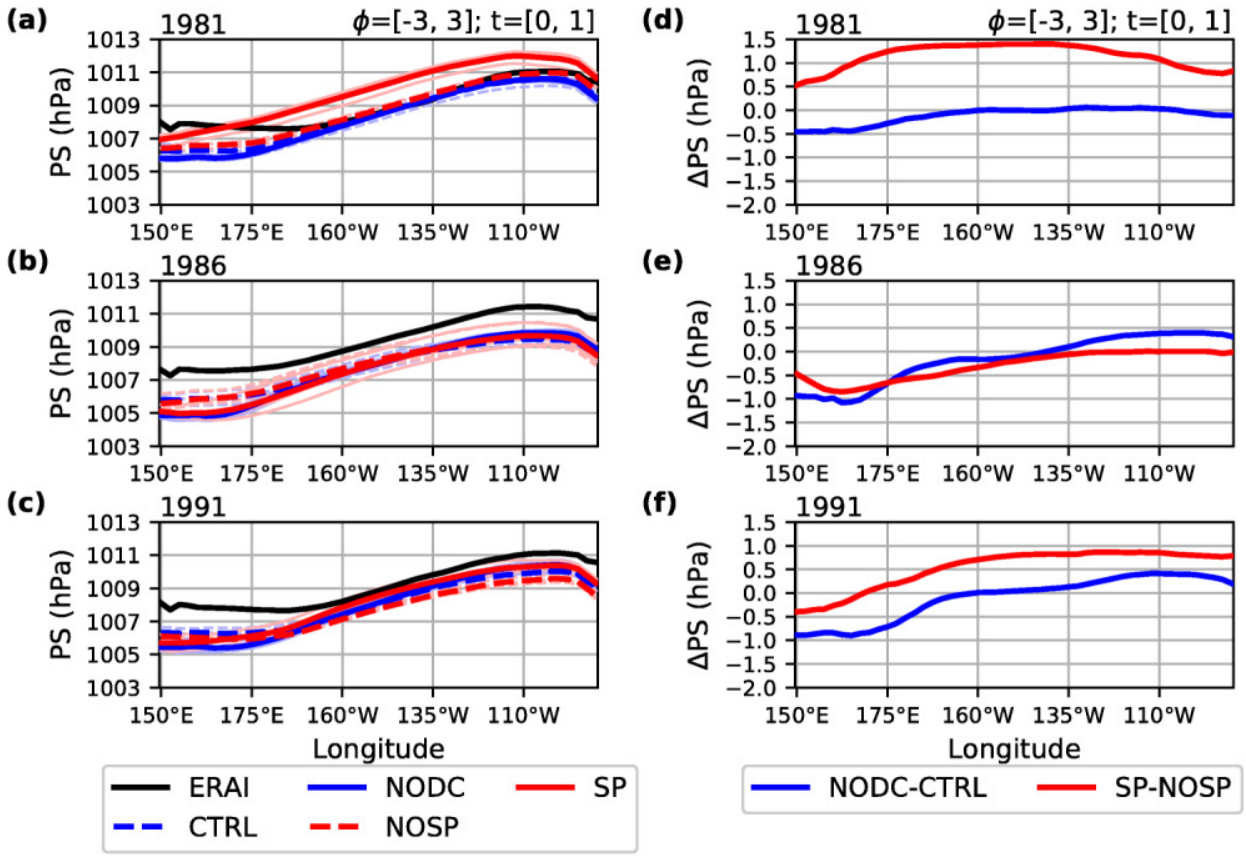

Figure 3.14: January–February meridional mean of sea-level pressure over the near-equatorial (±3° latitude) central Pacific for the fully coupled simulations, SODA, and ERAI for (a) 1981, (b) 1986, and (c) 1991. Bold lines show ensemble means or observations. Faded lines show ensemble members. Difference between perturbed convection ensemble means and the ensemble mean of their respective control simulations for (d) 1981, (e) 1986, and (f) 1991.

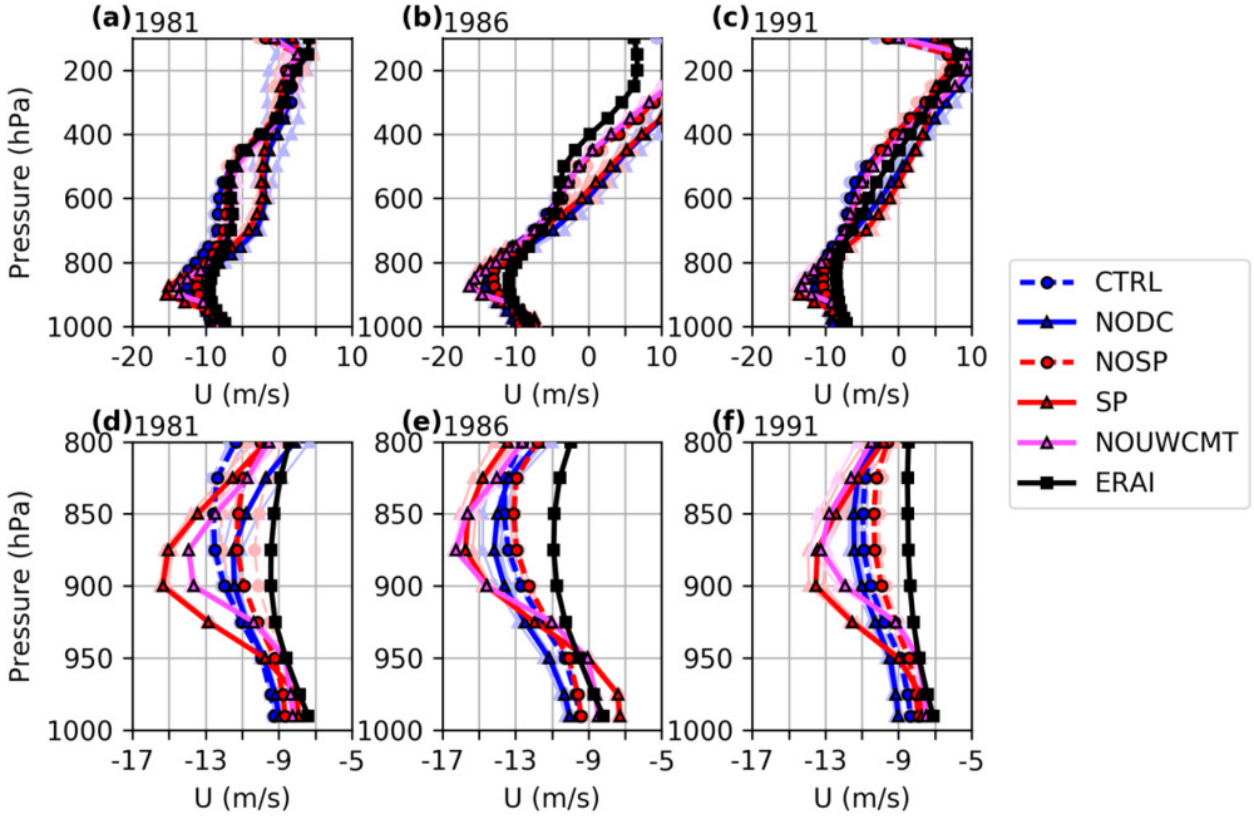

Figure 3.15: Vertical profile of zonal wind speed from (a) January 1981, (b) January 1986, and (c) January 1991 averaged over the cold tongue region, 3°S to 3°N and 180° to 140°W, for the CTRL, NODC, SP, NOSP, and NOUWCMT simulations and the ERAI reanalysis. The lower level wind profile (below 800 hPa) for each month is enlarged in figure 3.15d–f.

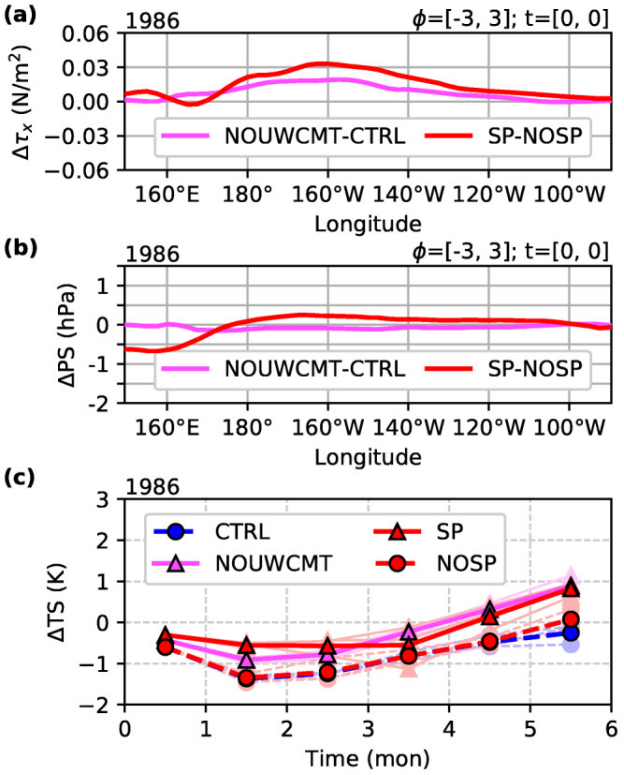

Figure 3.16: January 1986 near-equatorial (±3° latitude) (a) zonal wind stress and (b) surface pressure for SP and NOUWCMT as a difference from their respective control simulations. (c) Cold tongue index development for the 1986 CTRL, NOSP, SP, and NOUWCMT hindcasts. Bold lines are ensemble means; faded thin lines are ensemble members.

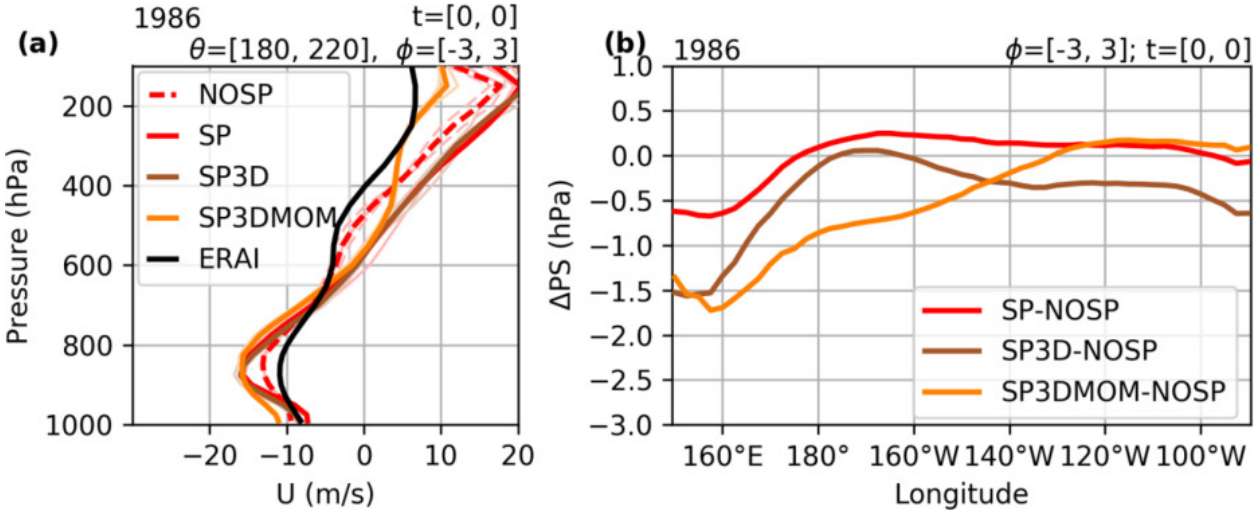

Figure 3.17: (a) January 1986 zonal wind profile for the NOSP, SP, SP3D, and SP3DMOM hindcasts alongside ERAI. Bold lines are hindcast ensemble means, and faded lines are individual ensemble members. (b) Near-equatorial (±3° latitude) surface pressure profile differences from NOSP.

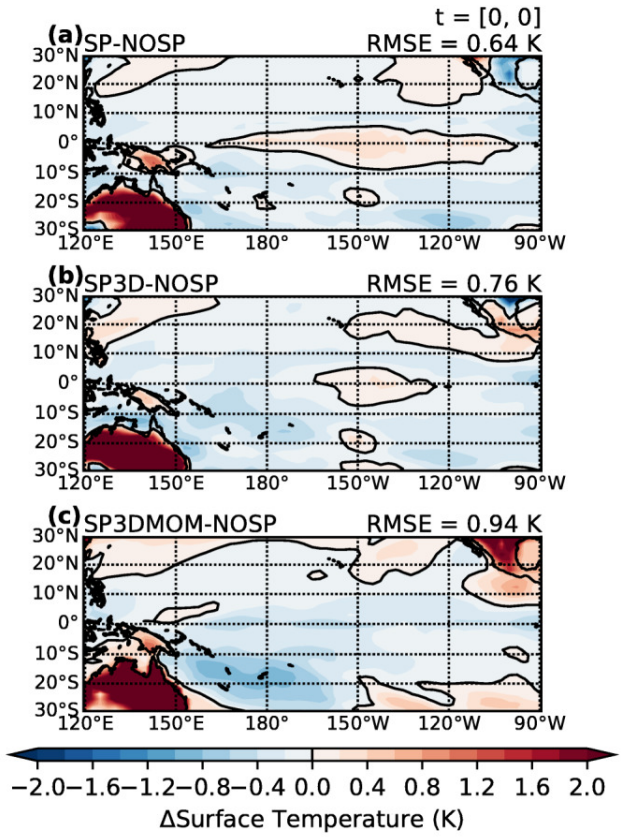

Figure 3.18: Difference in SST with respect to the NOSP hindcast for (a) SP, (b) SP3D, and (c) SP3DMOM averaged over January 1986.

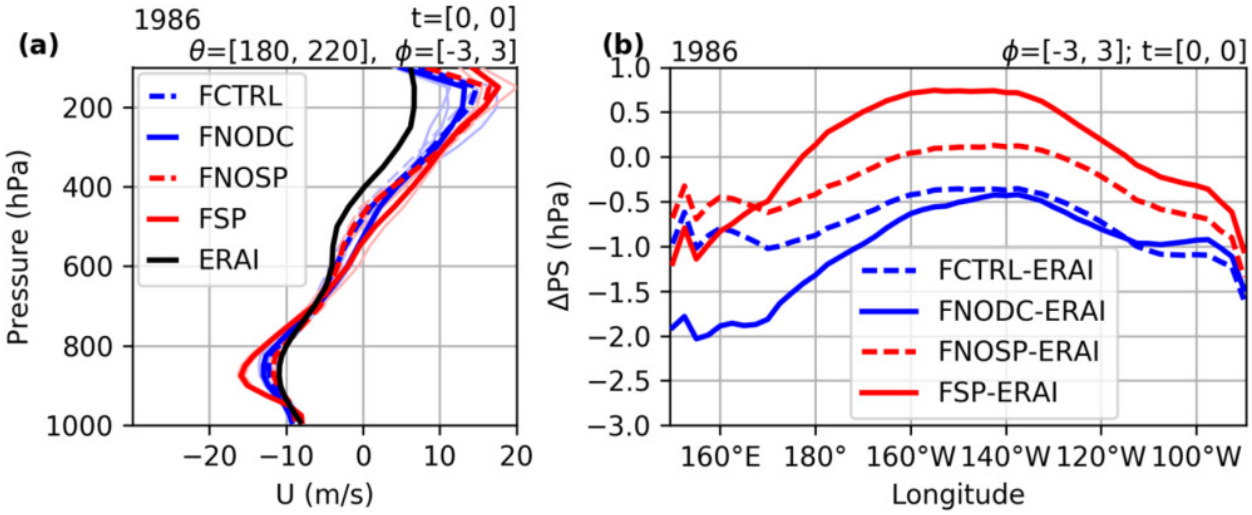

Figure 3.19: (a) January 1986 zonal wind profile for the fixed SST hindcasts alongside ERAI. Bold lines are hindcast ensemble means, and faded lines are individual ensemble members. (b) Near-equatorial (±3° latitude) surface pressure profile differences from ERAI.

Figure 3.20: Time evolution of the (a) cold tongue index and its components, (b) near equatorial central Pacific SSTs and (c) greater tropical Pacific mean SST, for single simulations initialized in January 1981 and utilizing the CTRL, NODC, NOSP, SP, and OCN model configurations. Plotted values cover the period from January 1981 through December 1985. Observations from SODA are included for comparison.

Chapter 4

Is oceanic buffering of forced ITCZ shifts controlled by an underappreciated Atlantic meridional overturning circulation pathway?

As submitted as:

Yu, S., and M. S. Pritchard (2018), Is oceanic buffering of forced ITCZ shifts controlled by an underappreciated Atlantic meridional overturning circulation pathway?, Journal of Climate, submitted (May 3rd, 2018).

Abstract

Ocean circulation responses to interhemispheric radiative imbalance can damp north-south migrations of the intertropical convergence zone (ITCZ), by reducing the burden on atmo-

spheric heat transport. The role of the Atlantic meridional overturning circulation (AMOC) in such dynamics has not received much attention. Here, we show coupled climate modeling results that suggest AMOC responses are of first order importance to muting ITCZ shift magnitudes as a pair of solar forcing bands is moved from equatorial to polar latitudes. The cross-equatorial energy transport response to the same amount of interhemispheric forcing becomes systematically more ocean-centric when higher latitudes are perturbed in association with strengthening AMOC responses. In contrast, the responses of the Pacific Subtropical Cell are not monotonic and cannot predict this variance in the ITCZ's equilibrium position. Overall these results highlight the importance of the meridional distribution of interhemispheric radiative imbalance and the rich buffering of internal feedbacks that occurs in dynamical versus thermodynamic slab ocean modeling experiments. Mostly, the result implies that the problem of developing a theory of ITCZ migration is entangled with that of understanding the AMOC's response to hemispherically asymmetric radiative forcing—a difficult topic deserving of focused analysis across more climate models.

4.1 Introduction

The intertropical convergence zone (ITCZ) is a band of intense rainfall encircling most of the tropics, roughly coinciding with the ascending branch of the Hadley Cell. Even a minor shift of its location (or change of its intensity) matters to society as this can result in major fluctuations of regional water availability in the tropics as well as impacting the extratropics through changes in the frequency of tropical cyclones (*Dunstone et al.*, 2013; *Merlis et al.*, 2013) and shifts of the midlatitude jet (*Ceppi et al.*, 2013; *Cvijanovic et al.*, 2013). The zonal-mean position of the ITCZ is constrained by interhemispheric energy imbalance of the atmosphere because the thermally-direct Hadley cell transports heat following the direction of its upper branch (i.e. the energetics framework; see *Schneider et al.* (2014) and *Kang et al.*

(2018) for reviews). That is, the ITCZ resides in the warmer hemisphere so that its upper branch crosses the equator, helping transport heat to the colder hemisphere. Transient ITCZ migrations toward an anomalously warmed hemisphere can occur in response to external forcing over a multitude of timescales, from seasonal to millennial (*Donohoe et al.*, 2013; *Schneider et al.*, 2014).

It is imperative to better understand such ITCZ shift dynamics, and especially the role of the ocean, which has been receiving increased attention. Recent global climate model (GCM) experiments have shown that oceanic dynamics can damp ITCZ shift responses to high-latitude forcing imposed by cloud brightness (*Kay et al.*, 2016), ocean albedo (*Hawcroft et al.*, 2016), sea-ice cover (*Tomas et al.*, 2016), and stratospheric aerosols (*Hawcroft et al.*, 2018). This is in contrast to studies that do not include ocean dynanmics (e.g. *Chiang and Bitz*, 2005; *Broccoli et al.*, 2006; *Kang et al.*, 2008) which exhibit more pronounced ITCZ shifts to extratropical forcings. This occurs since perturbations to interhemispheric energy balance need not be restored by the atmosphere alone in a dynamic ocean coupled GCM; they can also be mediated by changes in oceanic heat transport. The mechanical coupling between the Hadley cell and the oceanic subtropical cell (STC) via zonal surface wind stress has been attributed to one such damping effect (*Held*, 2001; *Schneider et al.*, 2014; *Green and Marshall*, 2017; *Schneider*, 2017; *Kang et al.*, 2018). But the role of STC damping relative to other potentially important oceanic damping pathways, such as the Atlantic meridional overturning circulation (AMOC), remains unclear. Yet theoretical arguments that the AMOC is fundamental to controlling the annual-mean ITCZ location (*Frierson et al.*, 2013; *Marshall et al.*, 2014) motivate its potential importance.

Several modeling studies already suggest important links between the AMOC and the ITCZ position. It has been known for decades that coupled GCM experiments subjected to freshwater hosing in the North Atlantic exhibit southward shifts of the ITCZ in association with a weakened AMOC (*Manabe and Stouffer*, 1995; *Vellinga and Wood*, 2002; *Zhang and Del-*

worth, 2005; *Chang et al.*, 2008; *Zhang et al.*, 2010; *Drijfhout*, 2010). More recently, *Fučkar et al.* (2013) argued that AMOC-type circulations determine the zonal-mean ITCZ position in an idealized limited-domain coupled GCM. Building on this work, *Frierson et al.* (2013) and *Marshall et al.* (2014) showed the ITCZ's annual-mean position tends to lie north of the equator is a result of AMOC heat transport, using a combination of slab ocean aqua-planet and idealized global coupled GCM, along with observational analysis. Other studies allude to an important role of the AMOC in the ITCZ shift response to aerosol clean-up projected over the 21st century. For instance, the projected northward ITCZ shift due to relative warming of the North Atlantic from regional aerosol clean-up is shown to be smaller in the Atlantic than in the Pacific (*Rotstayn et al.*, 2015; *Allen*, 2015) and counteracted by weakening of AMOC (i.e. cooling of the North Atlantic), ultimately muting the shift of annual-mean ITCZ position (*McFarlane and Frierson*, 2017).

The above studies all hint at the potential for ITCZ shifts to be modulated by the AMOC's response to external radiative forcing. But questions remain about how significant this AMOC-linked pathway is. Indeed, much is yet to be discovered about how the AMOC responds in general to geographically structured radiative forcing at top of atmosphere, as can occur through latitudinally sensitive cloud feedbacks to climate change, or some volcanoes, or through geoengineering by solar radiation management. Yet this may have implications for ITCZ shift dynamics.

We hypothesize that the AMOC can play an important role for muting ITCZ shift in this context. Conceptually this is based on the fact that on long (greater than interannual) timescales the AMOC variability is driven by thermodynamic forcing (*Buckley and Marshall*, 2016). This is in contrast to wind-driven variations in other circulation components such as the STC, whose variability is mainly driven by mechanical forcing via surface wind stress (*JP and Lu*, 1994; *Liu and Philander*, 1995). A consequence of mechanical coupling in the STC is that the cross-equatorial atmospheric and oceanic energy transports must

positively covary (as illustrated in figure 4.1a and b). That is, the partitioning between atmospheric and oceanic responses cannot vary much through the STC coupling, assuming oceanic thermal structures do not change much. The AMOC is not subject to this mechanical constraint; rather its heat transport has the capacity to covary negatively with a given top-of-atmosphere heating imbalance (as illustrated in figure 4.1c and d). Thus, if the AMOC responded sensitively to the details of how a hemispherically asymmetric external forcing were geographically distributed, this could potentially act as an efficient control on ITCZ shift damping, associated with changes in the overall ocean-atmosphere partitioning of the cross-equatorial energy transport response.

To probe this issue, we present results from a coupled climate model experiment, in which we artificially alter the top-of-atmosphere (TOA) energy budget through solar radiation modulation focused in discrete latitudinal bands at varying distances from the equator (figure 4.3a). The TOA insolation is perturbed to induce a northward heat transport by increasing (decreasing) the solar constant in the southern (northern) hemisphere. Such a perturbation is introduced at four different latitudinal bands (TROP, SUBTROP, MIDLAT, and HIGHLAT) occupying an equal area to examine partitioning responses to the different forcing locations. One additional experiment perturbing the whole hemisphere at a quarter of the magnitude (i.e. identical interhemispheric power asymmetry) is also performed (WHOLE). TOA forcing allows freedom for the simulated climate system to internally select its preferred partitioning of heat transport responses between the atmosphere and ocean (and, within the ocean, between AMOC vs. other ocean circulation components). Our forcing is in some ways similar to *Mechoso et al.* (2016) (solar flux alteration) and Haywood et al. and *Haywood et al.* (2016); *Hawcroft et al.* (2018) (stratospheric aerosol management), but also with three notable differences—(i) we only perturb non-UV part of solar radiation to avoid a direct stratospheric perturbation, (ii) we avoid net global perturbation by introducing both solar flux source and sink, and (iii) we integrate for long enough to sample AMOC responses (200 years, compared to 20 (*Haywood et al.*, 2016), 25 (*Mechoso et al.*, 2016), and 80 (*Hawcroft*

et al., 2018) years).

Consistent with our hypothesis, the results will reveal a strong correlation between the magnitude of AMOC responses and the meridional distribution of interhemispheric forcing, which in turn explains a large degree of variance in the degree of ITCZ shift response that occurs at equilibrium.

4.2 Method

4.2.1 GCM simulations

The Community Earth System Model (CESM) version 1.2.2. (*Hurrell et al.*, 2013) is used, configured with interactive atmosphere, land, ocean and sea ice components in a preindustrial experiment mode initialized with a spun-up ocean (i.e. the standard "B_1850_CAM5" component set). A set of five experiments that induce interhemispheric energy imbalance at top of the simulated atmosphere (TOA), but in different latitude ranges, by dividing each hemisphere into four zonal bands of equal area, eg. tropical, subtropical, mid-latitude, and high-latitude zones. The four experiments are called TROP, SUBTROP, MIDLAT and HIGHLAT hereafter. In addition, we perform an extra experiment (WHOLE) of which the whole hemisphere is perturbed but at a quarter magnitude in order to keep the area-integrated perturbation identical to other cases. A control simulation (CTRL) is conducted with no perturbation for the same period as that of the perturbed simulations. In each test, we introduce an artificial incoming non-UV shortwave energy source / sink pair at the TOA in the southern / northern hemisphere, of magnitude 17 W/m^2 in annual mean—by multiplying a constant factor, not adding, in order to prevent exceedingly high perturbation during winter. Our decision to position our forcing at TOA is attractive philosophically as it maximizes the simulated climate system's freedom to excite internal feedbacks and to inter-

nally select the partitioning of the meridional energy transport response between atmosphere and ocean. Each simulation is integrated for 200 years, but the last 150 years of simulations are used for the analysis in this paper, unless otherwise noted. Model simulation output and model code modification are available upon request.

4.2.2 Meridional energy transport calculation

The total (atmospheric plus oceanic) meridional heat transport, F, is calculated as

$$F(\phi) = -\int_{\phi}^{\pi/2}\int_{0}^{2\pi}\left[R_{TOA} - \frac{\partial(E_A)}{\partial t} - \frac{\partial(E_O)}{\partial t}\right]a^2 cos\phi d\theta d\phi,$$

where R_{TOA} is a residual radiative flux at TOA, E_A (E_O) is a column energy storage of atmosphere (ocean), a is the Earth radius, and θ and ϕ are longitude and latitude, respectively. Zonally-integrated meridional oceanic heat transport, F_O, is directly calculated from the ocean model by summing advective and diffusive fluxes over depth and longitude at each latitude. Meridional atmospheric heat transport, F_A, is calculated as a residual, e.g. $F_A = F - F_O$.

4.2.3 Oceanic heat transport decomposition

Cross-equatorial OHT is decomposed into into its dynamic ($T_{ctrl}\Delta v$), thermodynamic ($v_{ctrl}\Delta T$), and nonlinear components ($\Delta v \Delta T$),

$$\Delta(vT) = T_{ctrl}\Delta v + v_{ctrl}\Delta T + \Delta v \Delta T,$$

where v is meridional velocity, T is temperature, $\Delta(\cdots) = (\cdots)_{exp} - (\cdots)_{ctrl}$, and subscript exp (ctrl) means experiment (control) simulation result.

4.2.4 Tropical precipitation asymmetry index (PAI)

Following *Hwang and Frierson* (2013), a precipitation asymmetry index is calculated as the area-weighted mean precipitation rate difference between north (0° to 20°N) and south (20°S to 0°), then normalized by the area-weighted mean precipitation rate of the whole tropics (20°S to 20°N). Accordingly, the PAI captures the relative strength of the two solstice season ITCZ positions, as which we define the position of *annual-mean* ITCZ. The responses of PAI are well-correlated with that of the tropical precipitation centroid (figure 4.2), which is another popular measure of annual-mean ITCZ position.

4.3 Results

We begin by analyzing the annual-mean ITCZ precipitation response across the experiment ensemble using the last 150-year average. A southward ITCZ "shift", a term we will use as shorthand to describe an increase (decrease) in intensity of the southern (northern) zonal-mean, annual-mean rainfall band, is observed in all cases, as expected by the northward cross-equatorial atmospheric heat transport (AHT) response to warming (cooling) the southern (northern) hemisphere. However, its magnitude monotonically decreases as the forcing bands are moved poleward (figure 4.3b). This differing ITCZ shift response occurs *despite* the fact that the magnitude of incoming solar forcing asymmetry is constrained to be identical across the experiments. This implies that either (i) latitudinally varying internal radiative feedbacks modify the effective magnitude of the asymmetric forcing across experiments; and/or (ii) the cross-equatorial oceanic heat transport (OHT) response is sensitive to the geographic details of the forcing. While the effective forcing (i.e. including radiative feedbacks), which mostly determines the cross-equatorial total heat transport since oceanic heat content change is very small (fig. Sfigure 4.4), does show some variation across experiments, there is remarkably little spread in its net interhemispheric asymmetry (figure 4.3b) with a

range of 2.90–3.38 W/m^2 as a result of compensating internal radiative feedbacks (figure 4.4). This is interestingly inconsistent with the results of *Seo et al.* (2014), in which latitudinally sensitive cloud feedbacks are able to exert strong control of AHT due to the use of a slab ocean model; the implication is that dynamic oceanic buffering is important to this issue. For our own purposes the main point is that such internal radiative feedback can only explain about 0.12 PW spread in the total (oceanic plus atmospheric) cross-equatorial heat transport response, arguing against hypothesis (i) that the latitudinally varying internal radiative feedbacks may drive the AHT sensitivity to the forcing locations. In contrast the spread of AHT alone is much larger (figure 4.3c), implying that variability in the annual-mean ITCZ shift response is mainly driven by variability in OHT responses across the experiments.

So far we have found that the cross-equatorial heat transport partitioning between ocean and atmosphere becomes a key factor that determines the magnitude of ITCZ shift in our experiments: When interhemispherically asymmetric solar forcing is concentrated at higher latitudes, the partitioning of the coupled response becomes more ocean-centric and thus the ITCZ shift response becomes more muted. The question naturally arises as to why.

Before proceeding, we first confirm that it is appropriate to view relationships between AHT and ITCZ across our experiments through an energetics framework. This acknowledges that there can be special cases where such a framework can be inappropriate, for instance if the heat transport efficiency of the Hadley circulation (i.e. the gross moist stibility, GMS) dominates spread in the AHT response (*Seo et al.*, 2017) or if the eddy heat transport dominates spread in the time mean Hadley circulation heat transport (*Roberts et al.*, 2016). However, in our case, the cross-equatorial AHT response is a good proxy for a zonal-mean ITCZ shift response. A tight linear relationship between the cross-equatorial AHT and the mean meridional circulation (Hadley circulation) responses show GMS responses are secondary (figure 4.5), and the eddy heat transport (transient plus stationary) responses are much weaker than Hadley cell heat transport and scale with the strength of Hadley

circulation (figure 4.6). Thus a time-mean energetics framework is appropriate to apply in our analysis.

Figure 4.7 shows that Atlantic dynamics play a leading role in driving the tendency towards a more ocean-centric energy transport response with higher latitude forcing. To understand the role of each ocean, the basin-specific OHT responses are decomposed into dynamic and thermodynamic components (figure 4.7). The OHT responses to changing the latitudinal position of hemispherically asymmetric forcing are mostly driven by dynamic changes, not thermodynamic. But different ocean basins respond differently. Only the Atlantic shows a clear monotonic sensitivity across experiments in line with the global OHT sensitivity. In contrast, the Pacific-Indian OHT does not exhibit a monotonic sensitivity, except during the transition from SUBTROP to MIDLAT, during which both Atlantic and Pacific-Indian basins show comparable OHT increases. Despite the fact that the absolute magnitude of the Atlantic OHT response is generally smaller than that of the Pacific-Indian, normalized by its respective basin width the Atlantic is a much more efficient energy transporter (yellow dots in figure 4.7) and seems to play a controlling role in the experiments.

This draws our analysis toward the Atlantic meridional overturning circulation (AMOC), as the main dynamical pathway of meridional oceanic heat transport in the Atlantic. Consistent with the Atlantic OHT, the AMOC response becomes monotonically stronger as the solar forcing bands are moved poleward (figure 4.8a). Transient analysis shows this monotonic sorting with forcing latitude emerges within 30 years (figure 4.9a) and persists for two centuries amidst internal variability. There is reassuring consistency in the unsteady evolution of the anomalous Atlantic OHT and AMOC strength (figure 4.9a and b).

Unlike the AMOC responses, the Pacific-Indian STC responses do not exhibit a monotonic sensitivity with implications for total cross-equatorial OHT (figure 4.9c). While tantalizing changes in the STC circulation response do occur (figure 4.8b, and hemispherically asymmetric component in figure 4.10), no associated cross-equatorial OHT responses are detectable

(figure 4.9d). This implies internal compensations in the structure of the shallow overturning circulation's response buffer its overall interhemispheric energetics. The buffering mechanisms are case specific. For instance, in HIGHLAT, despite the fact that a weakening of the STC mass circulation response might act to reduce its OHT relative to CTRL, this is compensated by a deepening of the circulation indicating increasing vertical thermal contrast—in turn implying more efficient heat transport per unit overturning circulation, thus acting to increase OHT in resistance to the weaker circulation. A separate mechanism buffers the TROP experiment, via spinup of a strong cross-equatorial roll-type circulation near the equator (*Miyama et al.*, 2003) that acts against weakened STC mass circulation, in this case through a mechanism that is independent of the STC's depth.

4.3.1 Different timescale between Pacific and Atlantic Mechanism

In figure 4.11, scatter plots of key predictors of tropical precipitation asymmetry both within experiments (i.e. dots of one color) and across experiments (i.e. dots spanning multiple colors) provide an especially compact way to contrast the differing roles of the two ocean basins on multidecadal (top) vs. interannual (bottom) timescales. On long timescales, the decomposition of the global relationship between PAI and OHT shows that the Atlantic clearly controls the equilibrium state response to the TOA forcing (monotonic color ranking along statistically significant inter-experiment regression line in figure 4.11a, b), whereas the Pacific-Indian OHT cannot detectably predict global PAI variance within noise (figure 4.11c). However, on short timescales, a robust regression is detected within each experiment between Pacific-Indian OHT and global PAI (colored regression lines in figure 4.11d, f). This timescale separation between the two ocean basins is robust to variations of the exact running mean windows used to discriminate short- from long-term behavior, although the long-term Atlantic correlation reaches its maximum around a 10-year averaging window (figure 4.11g).

The opposite signs of the PAI–OHT correlation for the Atlantic (across experiments) versus the Pacific-Indian (within experiments) illustrate the fundamental difference of AMOC vs. STC freedom to damp ITCZ shifts that was alluded to in the introduction and figure 4.1. Keeping in mind that a more negative PAI implies a more southward ITCZ position and a more positive (northward) cross-equatorial AHT (figure 4.12), the regressions in figure 4.11 show that Atlantic OHT negatively covaries with AHT, whereas Pacific-Indian OHT positively covaries with AHT. This confirms our hypothesis that an AMOC response has the capacity to be an effective damping mechanism for ITCZ shift, as it can significantly alter the partitioning between atmospheric and oceanic heat transport.

We note that the cross-experiment correlation between the PAI and the Atlantic $\mathrm{OHT_{eq}}$ responses (figure 4.11b) does not depend on the fact that the magnitude of effective forcing (forcing + radiative feedbacks)—which dictates the total heat transport (TotalHT) magnitude—happens to have been similar across our experiments (e.g. figure 4.3c). While the response magnitudes of $\Delta\mathrm{AHT_{eq}}$ and $\Delta\mathrm{OHT_{eq}}$ are constrained by the effective forcing magnitude ($\Delta\mathrm{AHT_{eq}} + \Delta\mathrm{OHT_{eq}} = \Delta\mathrm{TotalHT_{eq}}$), the *partitioning* between $\Delta\mathrm{AHT_{eq}}$ and $\Delta\mathrm{OHT_{eq}}$ is not, i.e.

$$\frac{\Delta\mathrm{AHT_{eq}}}{\Delta\mathrm{TotalHT_{eq}}} + \frac{\Delta\mathrm{OHT_{eq}}}{\Delta\mathrm{TotalHT_{eq}}} = 1, \tag{4.1}$$

implying that the negative covariance between the normalized quantities is guaranteed despite the fact that the covariance of the un-normalized quantities depends on the magnitude of $\Delta\mathrm{TotalHT_{eq}}$. Assuming that the Hadley Circulation heat transport dominates the cross-equatorial atmospheric heat transport ($\Delta\mathrm{AHT_{eq}} = \Delta\mathrm{AHT_{eq}^{HC}} + \Delta\mathrm{AHT_{eq}^{EDDY}} \approx \Delta\mathrm{AHT_{eq}^{HC}}$; Fig. 4.6), that the cross-equatorial oceanic heat transport is mostly driven by two overturning circulations ($\Delta\mathrm{OHT_{eq}} \approx \Delta\mathrm{OHT_{eq}^{STC}} + \Delta\mathrm{OHT_{eq}^{AMOC}}$), and that $\mathrm{AHT_{eq}^{HC}}$ and $\mathrm{OHT_{eq}^{STC}}$ are

coupled ($\Delta \mathrm{OHT}_{\mathrm{eq}}^{\mathrm{STC}} \approx \alpha \Delta \mathrm{AHT}_{\mathrm{eq}}^{\mathrm{HC}}$; *Held* (2001)), Eq. 4.1 can be simplified to

$$(1+\alpha)\frac{\Delta \mathrm{AHT}_{\mathrm{eq}}^{\mathrm{HC}}}{\Delta \mathrm{TotalHT}_{\mathrm{eq}}} + \frac{\Delta \mathrm{OHT}_{\mathrm{eq}}^{\mathrm{AMOC}}}{\Delta \mathrm{TotalHT}_{\mathrm{eq}}} = 1, \tag{4.2}$$

where the superscripts HC, EDDY, STC, and AMOC denote heat transport components due to the Hadley Circulation, eddies, the subtropical cell, and the Atlantic meridional circulation, respectively, and α is a positive definite function. Accordingly, we expect to see a similarly tight, if not tighter, correlation when normalizing $\mathrm{OHT}_{\mathrm{eq}}$ by the effective forcing magnitude; indeed this is confirmed in figure 4.13.

4.4 Discussion

The many internal feedbacks in our experiments have led to behaviors worth contrasting against the intuition gained from slab ocean modeling setups, which would not have predicted them. For instance, using a slab-ocean coupled GCM forced by a prescribed oceanic heat transport, *Seo et al.* (2014) showed amplifying TOA energy imbalance and hence a larger ITCZ shift with higher latitude perturbation, and explained this as a result of net positive SST–low cloud, SST–outgoing longwave radiation (OLR) feedbacks. Despite the fact that similar SST-mediated radiative feedbacks also exist in our study, we observe a TOA energy imbalance that is largely insensitive to forcing latitude. This can be traced to the fact that we observe a much weaker SST response magnitude (figure 4.14a) in our more heavily buffered system. For instance, our SST response for HIGHLAT is about 3 K, but this is an order of magnitude smaller than Seo el al. (20–80 K) despite the fact that their forcing magnitude is only 1.64 times larger than in our experiment. A decomposition of the details shows that for our high latitude forcing cases (MIDLAT and HIGHLAT), the SST–OLR negative feedback actually wins over the positive SST-low cloud feedback. This underscores that important positive feedbacks that were not included in the setup of *Seo*

et al. (2014) ended up playing leading roles in our high latitude forcing cases (figure 4.4). One likely culprit is the positive ice–albedo feedback, which counteracts the negative SST–OLR feedback. It is unclear whether the resilient net TOA response across our simulations is a coincidence, or an intrinsic feature of the Earth's climate system in the limit of fully interactive radiative/convective/SST feedbacks; this could be worth more study. Regardless, our findings about partitioning do not depend on the net TOA response magnitude having turned out this way (figure 4.11 and figure 4.13).

Meanwhile, the damped SST response in our simulations highlights the importance of the ocean circulation's role in the global energy budget. Ocean dynamics limit excessive local storage of heat near the surface by redistributing it vertically and horizontally. We have focused on the striking role of overturning circulations in this regard, but the role of gyre circulations would also be an interesting direction for future work to further understand the ocean's role in ITCZ shift buffering. While the subtropical gyre circulations do not participate much in the direct (advective) heat exchange across the equator, they can non-locally affect both the atmospheric and oceanic column energy budgets via SST-dependent feedbacks, such as through SST–low cloud feedbacks modulated by gyre currents that carry anomalously heated surface water away from radiative action centers (*Mechoso et al.*, 2016). Indeed, such linkages occur in our experiments (figure 4.14).

It is worth commenting on the utility of using a theoretical framework pinned on equatorial atmospheric net energy input ($\mathrm{NEI_{eq}}$) to interpret our simulations. $\mathrm{NEI_{eq}}$ has been argued to determine the sensitivity of the latitude of the zonal-mean ITCZ (ϕ_{ITCZ}) to a given magnitude of $\mathrm{AHT_{eq}}$ perturbation, i.e. $\phi_{\mathrm{ITCZ}} \sim \frac{\mathrm{AHT_{eq}}}{\mathrm{NEI_{eq}}}$ (*Bischoff and Schneider*, 2014). $\mathrm{NEI_{eq}}$ is also known to correlate with the hemispherically symmetric component of tropical precipitation biases including the double ITCZ bias (*Adam et al.*, 2016, 2017). We hypothesize that variations in the $\mathrm{NEI_{eq}}$ response to solar forcing do not play a leading role in our experiments based on the quasi-linear relationship between interannual PAI vs. global $\mathrm{OHT_{eq}}$ responses

(figure 4.11d, f). Consistent with this view, the fractional response of NEI_{eq} is much smaller than that of AHT_{eq} (figure 4.15). However, we acknowledge that effects of NEI_{eq} are important and may be responsible for the deviation from the linear regression line, since changes in NEI_{eq} can cause ITCZ shifts independent of changes in AHT_{eq}.

An obvious limitation of this study is the use of a single climate model, which raises the question of whether similar responses should be expected in other climate models. On the one hand, a satisfying answer on inter-model spread will only be gleaned from focused intercomparison, which will be forthcoming via a new Extratropical-Tropical Interaction Model Intercomparison Project. This community activity will include analysis of atmosphere-ocean partitioning of the energy transport response to extratropical TOA perturbation [Sarah Kang, personal communication, 2017]. On the other hand, it is also already logical to expect some degree of similarity of responses to occur across independent models. Despite the fact that the temporal mean structure and variability of the AMOC varies widely among Coupled Model Intercomparison Project version 3 and 5 (CMIP3 and 5) models (*Medhaug and Furevik*, 2011; *Zhang and Wang*, 2013; *Muir and Fedorov*, 2015), the AMOC's response to differing forms of radiative forcing tends to share a common sign. Across CMIP5 models, anthropogenic CO_2 forcing tends to weaken the AMOC (*Gregory et al.*, 2005; *Cheng et al.*, 2013), and volcanic aerosol forcing strengthens it (*Ding et al.*, 2014) while also shifting the ITCZ towards the hemisphere opposite to eruption (*Iles and Hegerl*, 2014). Anthropogenic aerosol forcing has also been shown to strengthen the AMOC across a set of independent studies that used different coupled GCMs (e.g. GFDL CM2.1 (*Delworth and Dixon*, 2006), CSIRO Mk2.1 (*Cowan and Cai*, 2013), and HadGEM2-ES (*Menary et al.*, 2013)). Especially considering that our TOA solar perturbation shares some similarities to a geographically confined aerosol radiative forcing, these are all reasons to expect that the sensitivity we have shown in CESM should be detectable in other CMIP5-class climate models.

Another limitation of this work is that it does not attempt to fully attribute the mechanistic

pathway connecting regional TOA solar forcing to varying degrees of AMOC response. While beyond scope, we view it as an interesting topic worthy of future work, via process analysis focused on subducting regions. As expected from cooling of the North Atlantic, positive regional anomalies of surface ocean density over the Labrador Sea deep water formation region lead AMOC responses in all our experiments (figure 4.16). But the origin of these density perturbations in the Labrador Sea is not immediately obvious, especially in the case of low-latitude forcing experiments where solar perturbations are applied away from the deep water formation regions. Relevant processes are likely to include advection of buoyancy anomalies through subtropical and subpolar gyres and regional meteorological changes via tropical-extratropical teleconnection. Future work focusing on these mechanistic process chains might help contribute to further understanding of the AMOC–ITCZ nexus. Another caveat of our experimental design is that the TROP forcing somewhat awkwardly attempts to force a sharp thermal gradient near the equator. On the one hand, the actual near-equatorial SST gradient response of this subexperiment is not an outlier relative to our other simulations, which suggests sharp thermal gradients are efficiently buffered by dynamics that must resist them near the equator (figure 4.17). Nonetheless, future iterations of this experiment design would benefit from avoiding this technical issue.

A final limitation is our use of idealized, geographically localized forcing bands to probe the coupled system's dynamics. It is natural to wonder to what degree this informs understanding of the system's sensitivity to more realistic sources of interhemispherically asymmetric solar forcing like volcanoes or geo-engineering. In this context we suggest it may be possible to think of our experiments as akin to Green's functions, or kernels, in that they have some demonstrable additive utility. That is, the results of the WHOLE experiment, in which we perturb each entire hemisphere at one quarter the power magnitude of the four regional sub-experiments, reproduces to a remarkable degree the linear average of those four experiments' independent responses (e.g. figs. 4.4, 4.7, and 4.8). This implies some generality beyond our idealized setup that could be practically relevant to many realistic forcing contexts; the idea

of kernels summarizing these dynamics is worth exploring more.

Notwithstanding such limitations, one implication of our results relates to improving tropical rainfall biases in coupled GCMs. Our results, along with recent coupled GCM studies (*Kay et al.*, 2016; *Hawcroft et al.*, 2016, 2018), seem to challenge the notion that *high-latitude* cloud radiative biases play a controlling role on biases of tropical precipitation, a view that has been supported by correlations across CMIP5 models(*Hwang and Frierson*, 2013). Our experiments imply the opposite, given that the AMOC response can provide an efficient buffer to ITCZ shifts when hemispherically asymmetric radiative forcing biases are concentrated at high latitudes. The reduction of this oceanic buffering pathway when the same interhemispheric forcing is focused at low latitudes implies that even a small bias in cloud radiative forcing near the tropics might induce a strong atmospheric (ITCZ shift) response. This appears consistent with the findings of *Xiang et al.* (2017) who argued that across CMIP5 models, the degree of the double ITCZ bias of coupled models is better predicted by the hemispheric asymmetry of their net TOA shortwave fluxes near the tropics in atmosphere-only simulations, than by those in the extratropics. It also evokes the findings of *Mechoso et al.* (2016) who showed stratocumulus cloud biases in the subtropics can overwhelm modifications to southern ocean radiative forcing. Together, these results support renewed focus on improving *low-latitude* radiation biases towards improving tropical precipitation.

4.5 Conclusion

We have shown results from a comprehensive global climate model that reveals the AMOC can be especially important in setting the degree to which ocean dynamics act to damp radiatively forced migrations of the zonal-mean ITCZ. This effect becomes strong when an interhemispherically asymmetric forcing is focused at high latitudes, highlighting the importance of the meridional distribution of shortwave radiative forcing in such dynamics.

The main implication is that ongoing attempts to develop ITCZ migration theory that includes the role of buffering by ocean dynamics may ultimately depend on a satisfying theory for the AMOC's response to radiative forcing, and its links to the ITCZ. Another practical implication for near-term GCM development is that fixing low-latitude TOA radiative biases in climate models might be a more practical strategy towards improving tropical rainfall biases than fixing high-latitude biases.

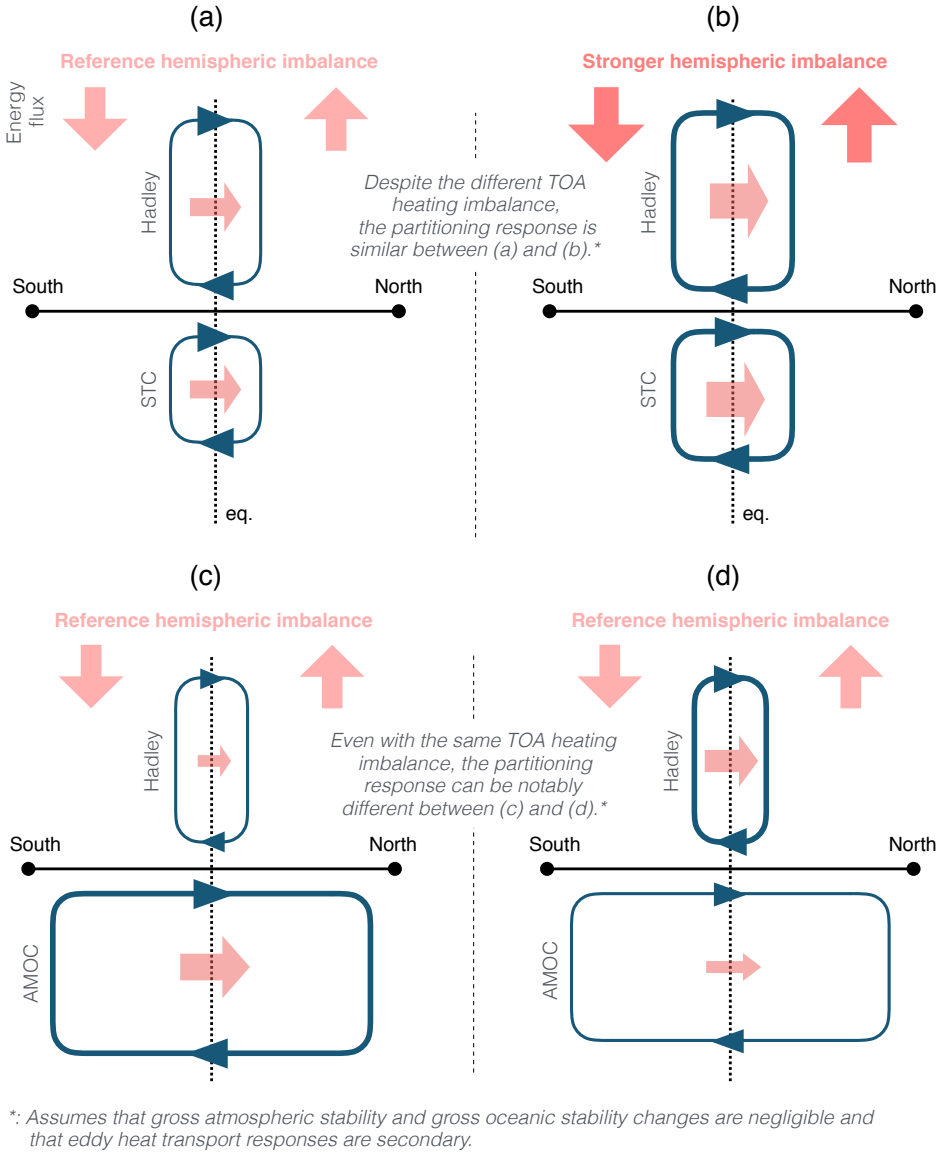

Figure 4.1: Schematics of ITCZ shift damping mechanisms involved with (a, b) the subtropical cell, versus (c, d) the Atlantic meridional overturning cell. Red vertical arrows denote a hemispherically asymmetric top-of-atmosphere net radiative perturbation, and blue lines the associated zonal-mean overturning streamline responses. (Top) The subtropical cell (STC) and Hadley cell (HC) are mechanically coupled via zonal surface wind stress such that the STC and HC overturn in the same direction with similar response partitioning. In this limit a spinup of the STC (b) must associate with a spinup of the HC and enhanced demand from additional interhemispheric forcing. (Bottom) In contrast, the Atlantic Meridional Overturning Circulation (AMOC) is not subject to these constraints. A diverse set of response partitionings is possible. Even with no change in interhemispheric forcing a strengthening AMOC requires a weakening HC (c, d), or vice-versa, due to atmosphere-ocean competition for a fixed amount of required energy transport. That is, the two cells' responses can be prone to negatively covary.

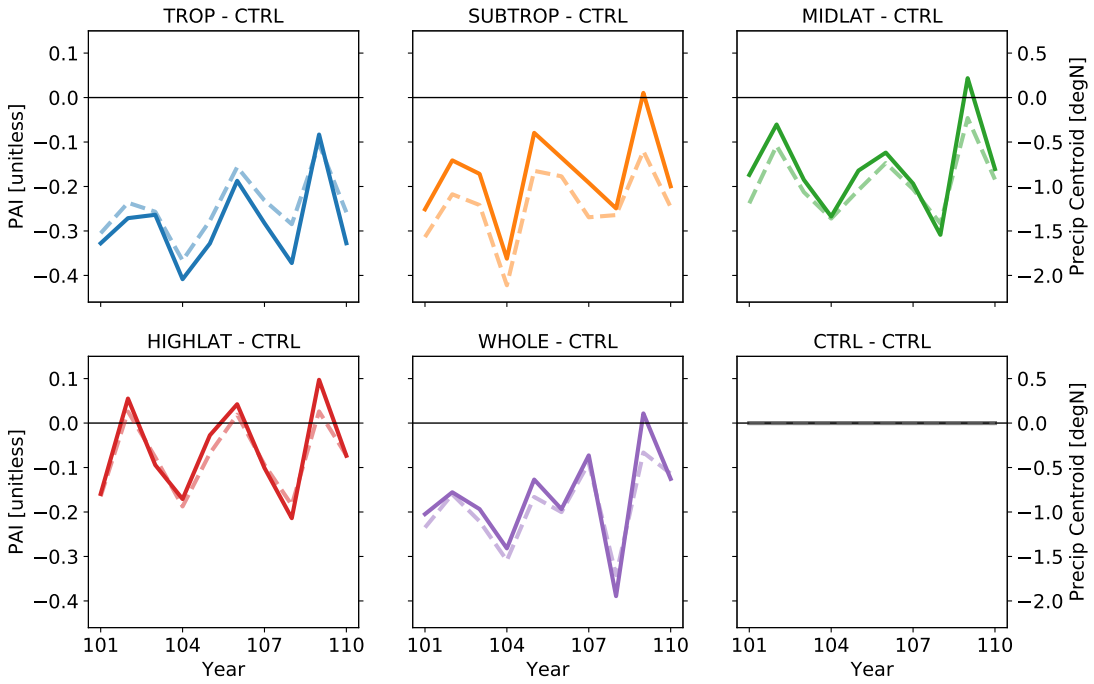

Figure 4.2: Comparison between (solid) the precipitation asymmetry index and (dashed) precipitation centroid as alternate measures of the tropical rainfall responses, computed within 20 degrees of the equator, for an arbitrary time interval of the simulation (years 101-110).

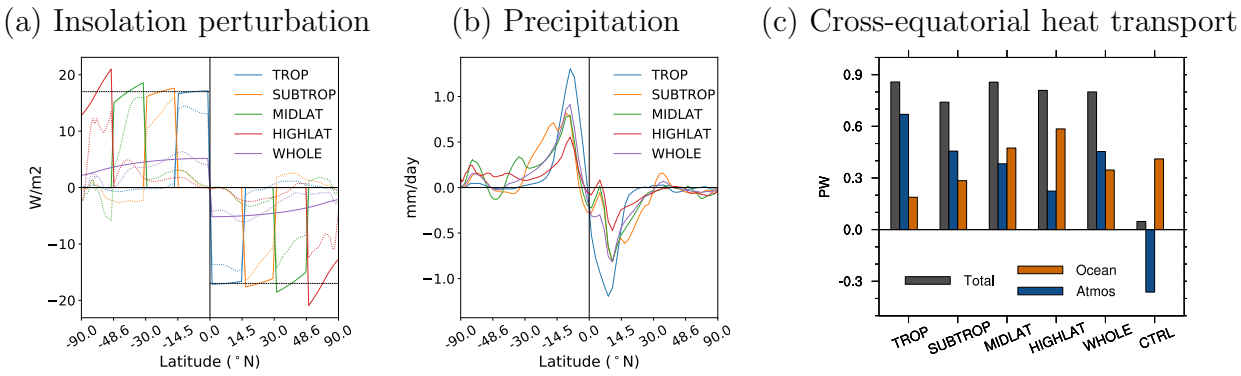

Figure 4.3: (a) Zonal-mean, annual-mean top-of-atmophere insolation perturbation (solid line) and net radiative flux responses (dotted line). (b): Zonal-mean, annual-mean precipitation responses. (c): Annual-mean cross-equatorial heat transport responses of total (grey), atmospheric (blue), and oceanic (brown)—control results are shown as a baseline.

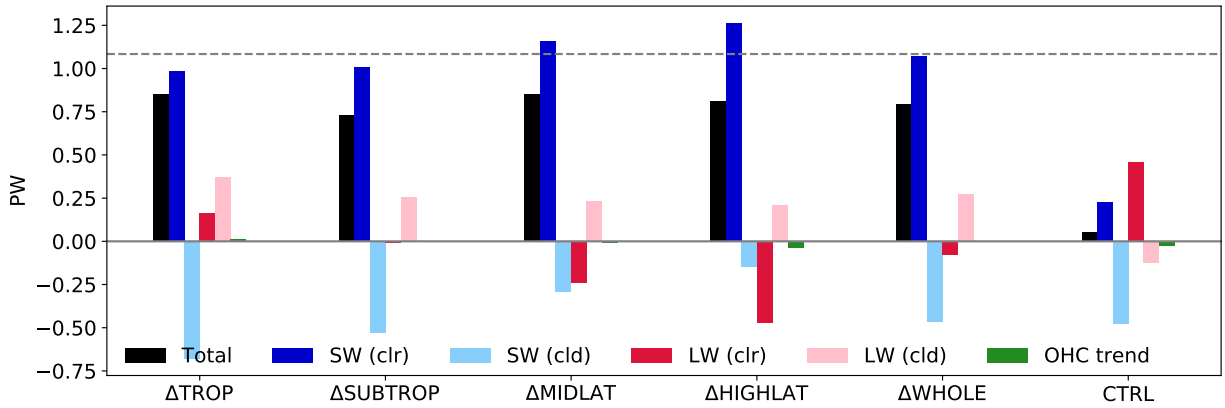

Figure 4.4: The decomposition of the annual-mean cross-equatorial total heat transport (HT_{eq}) responses. The HT_{eq} (black) is decomposed into heat transports due to clear-sky shortwave flux (blue), shortwave cloud radiative effect (CRE) (light blue), clear-sky longwave flux (red), longwave CRE (light red), and oceanic heat content trend. Δ means experiment minus control. All radiative fluxes are at the top of atmosphere. Averaging period is from model year 51 to 200.

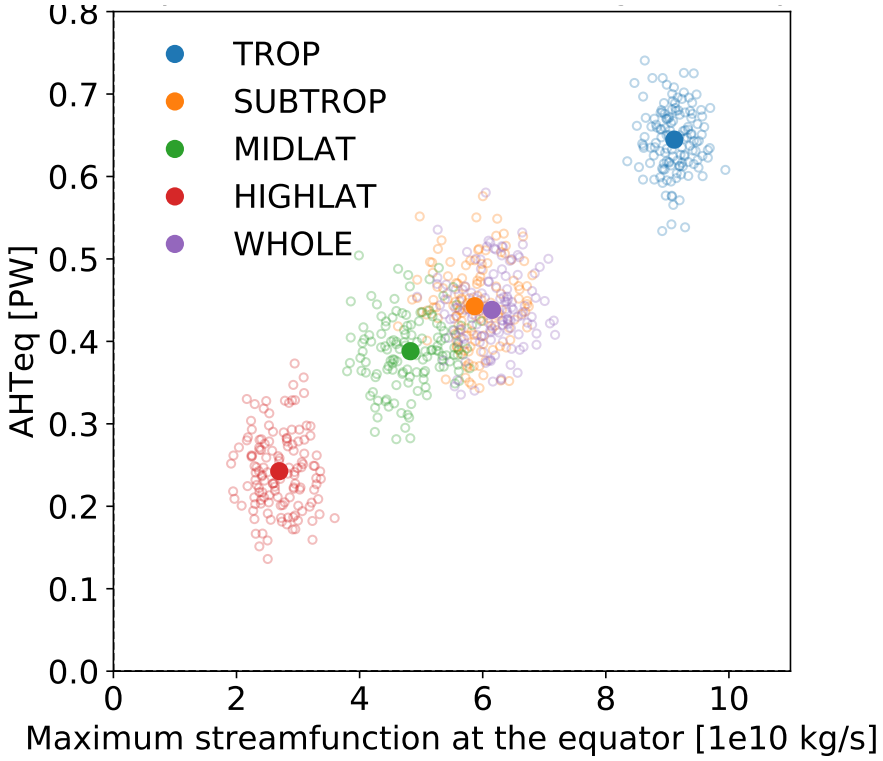

Figure 4.5: Scatter plot between the annual-mean cross-equatorial atmospheric heat transport (AHT_{eq}) response and annual-mean maximum meridional mass streamfunction response at the equator—as a proxy of Hadley circulation strength. Empty dots are 15-year running-averaged time-series for year 51–200 and the filled dots are the mean value of them. The strong relationship implies changes in gross moist stability across the experiments are not significant.

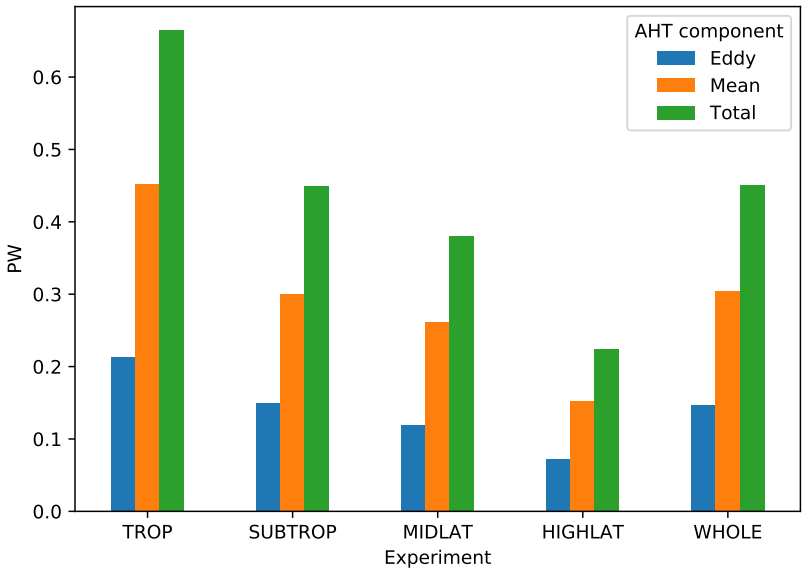

Figure 4.6: The decomposition of the annaul-mean cross-equatorial atmospheric heat transport (green) into meridional mean circulation (orange) and eddy (blue) components. The eddy component include both stationary and transient eddies.

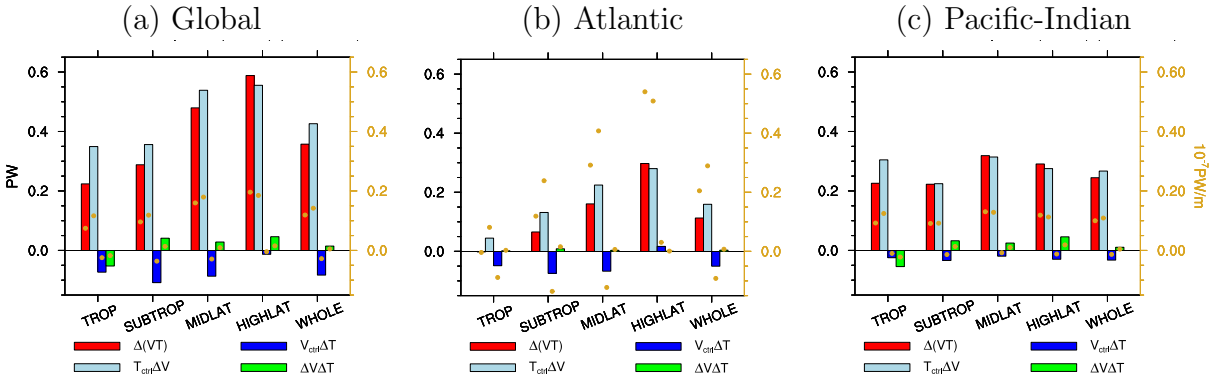

Figure 4.7: Annual-mean, cross-equatorial oceanic heat transport (OHT) responses of global (a), Atlantic (b), and Pacific-Indian (c) ocean [unit: PW]. Different colors show different component of OHT: total (red), dynamic (light blue), thermodynamic (deep blue), and nonlinear (green). Yellow dots are for OHT normalized by basin width [unit: 10^{-7} PW / meter].

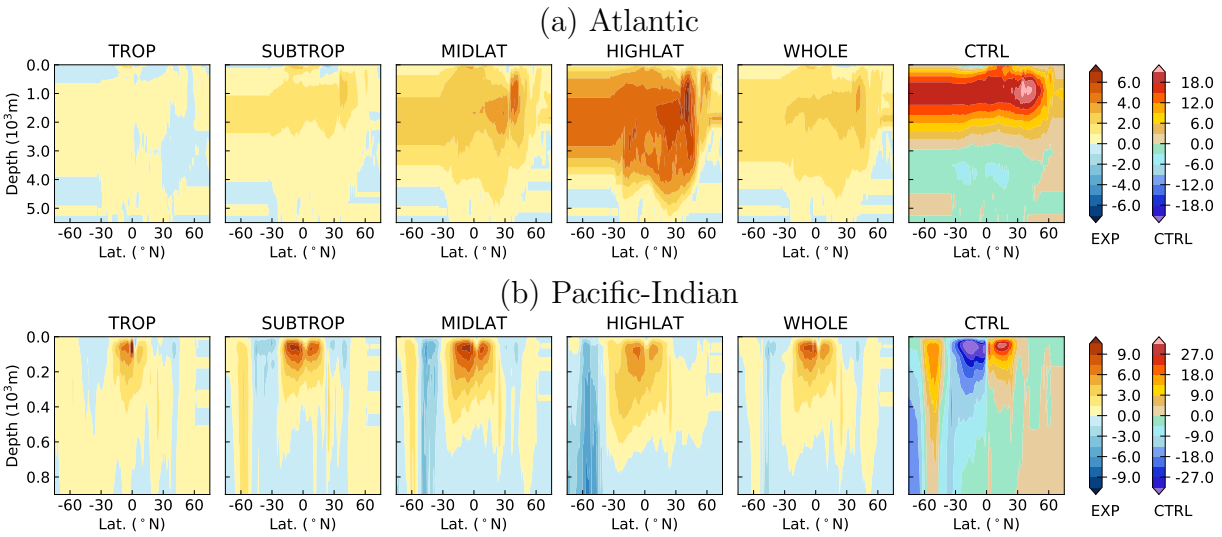

Figure 4.8: Annual-mean overturning streamfunction responses for Atlantic (a) and Pacific-Indian basin (b). Right most panels are total response of control simulation [unit: Sv]. Warm (cold) colors are signed as clockwise (counter clockwise) circulations. Note that (a) and (b) have different depths and color bars.

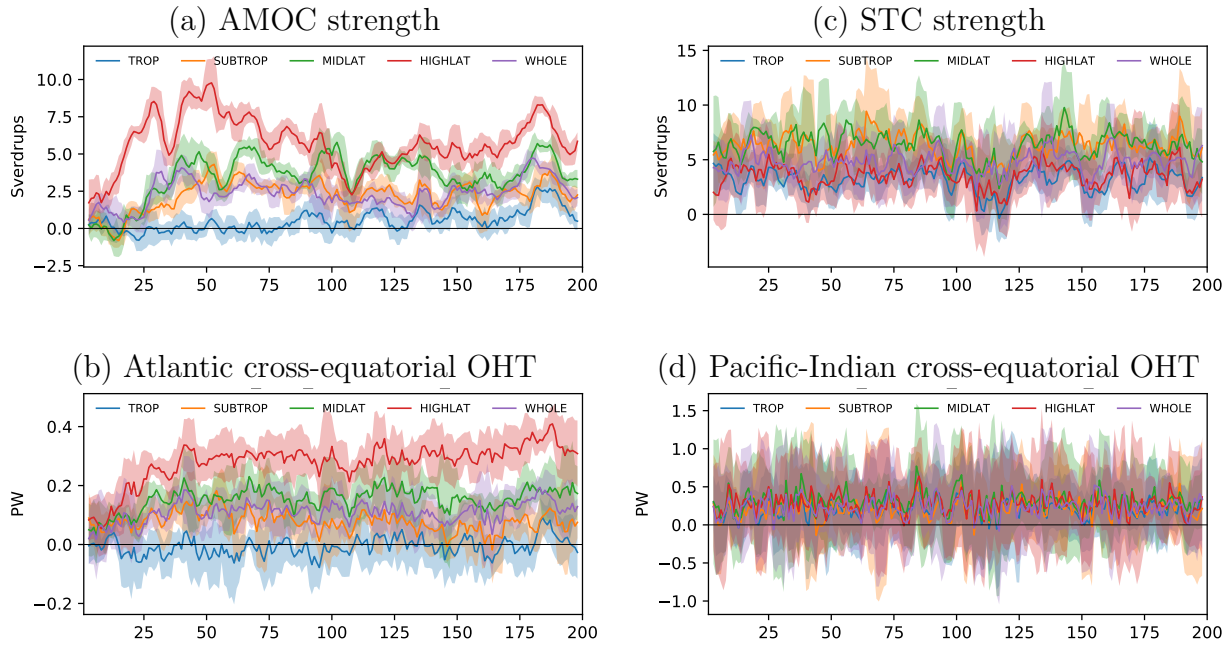

Figure 4.9: Time series of responses of AMOC strength(a), Atlantic cross-equatorial oceanic heat transport (b), Pacific-Indian asymmetric subtropical cell strength (c), and Pacific-Indian cross-equatorial oceanic heat transport (d). A solid line shows 5-year running mean and shading is ± one 5-year running standard deviation. AMOC strength is defined as a maximum overturning streamfunction within 30°N to 50°N latitude and 600m to 1400m depth in Atlantic. Pacific-Indian asymmetric subtropical cell strength is defined as a maximum of asymmetric component of overturning streamfunction within 7°N to 15°N latitude and 0m to 250m depth in Pacific-Indian.

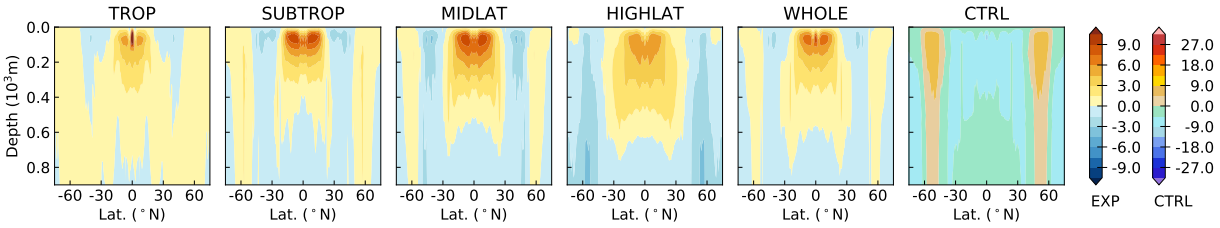

Figure 4.10: Asymmetric component of figure 3b (Pacific-Indian meridional overturning streamfunction). Following Green and Marshall *Green and Marshall* (2017), Asymmetric component is defined as $\psi(\phi) = [\psi(\phi) + \psi(-\phi)]/2$, where ψ is overturning streamfunction, and ϕ is latittude.

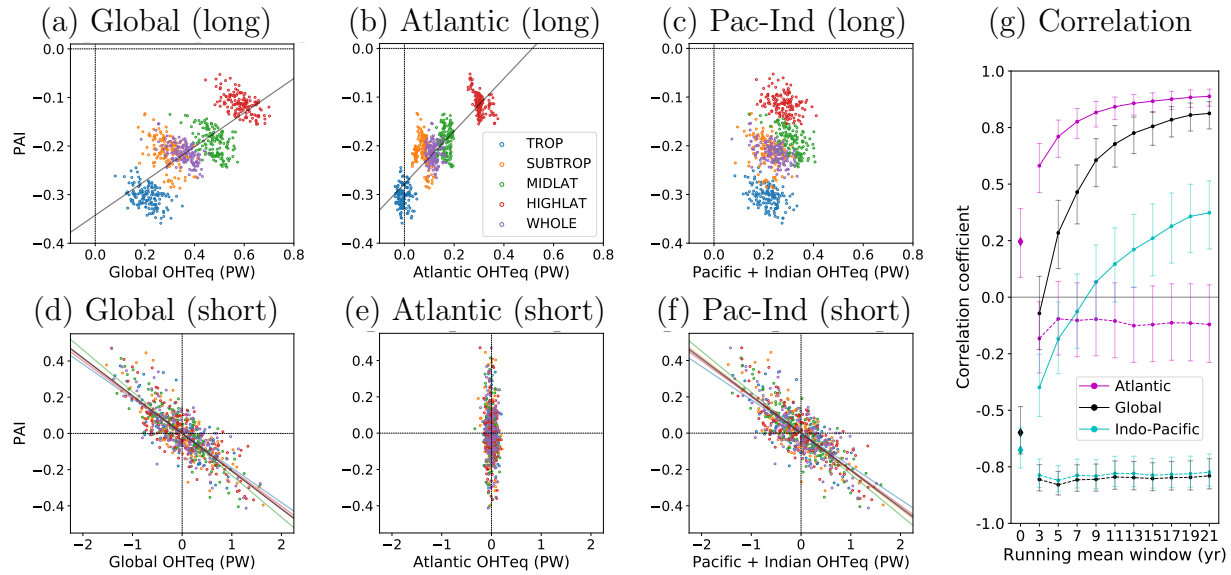

Figure 4.11: Scatter plots of annual-mean time series between tropical precipitation asymmetry index (PAI) and cross-equatorial oceanic heat transport (OHT) during Year 51 to 200. (top panels) long-term component defined as 15-year running average; (bottom panels) short-term component defined as anomalies from the long-term component. (a, d) Global ocean; (b, e) Atlantic ocean; (c, f) Pacific and Indian ocean. Regression lines for all experiments (grey) and for each experiment (color) are shown only for relationship whose r^2 is larger than 0.5. (g) shows correlation coefficients, r, of long-term (solid line) and short-term (dashed line) with different running mean windows. Zero running mean window means original time series. Errors bars are 95% confidence interval.

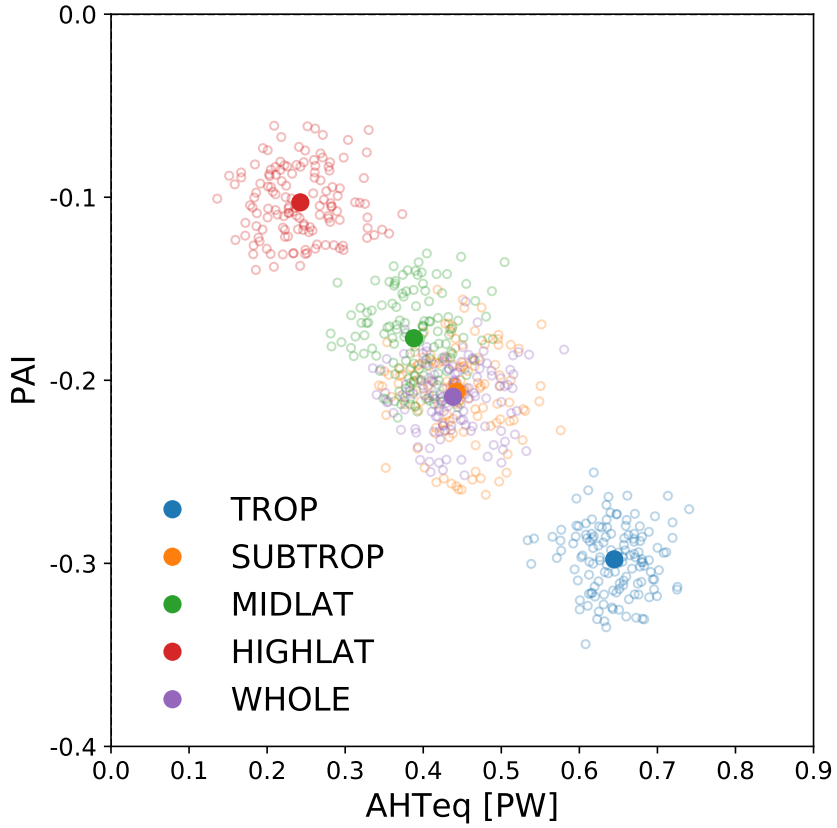

Figure 4.12: Scatter plot between the annual-mean tropical precipitation asymmetry index (PAI) response and the annual-mean cross-equatorial atmospheric heat transport (AHT_{eq}) response. Empty dots are 15-year running-averaged time-series for year 51–200 and the filled dots are the mean value of them.

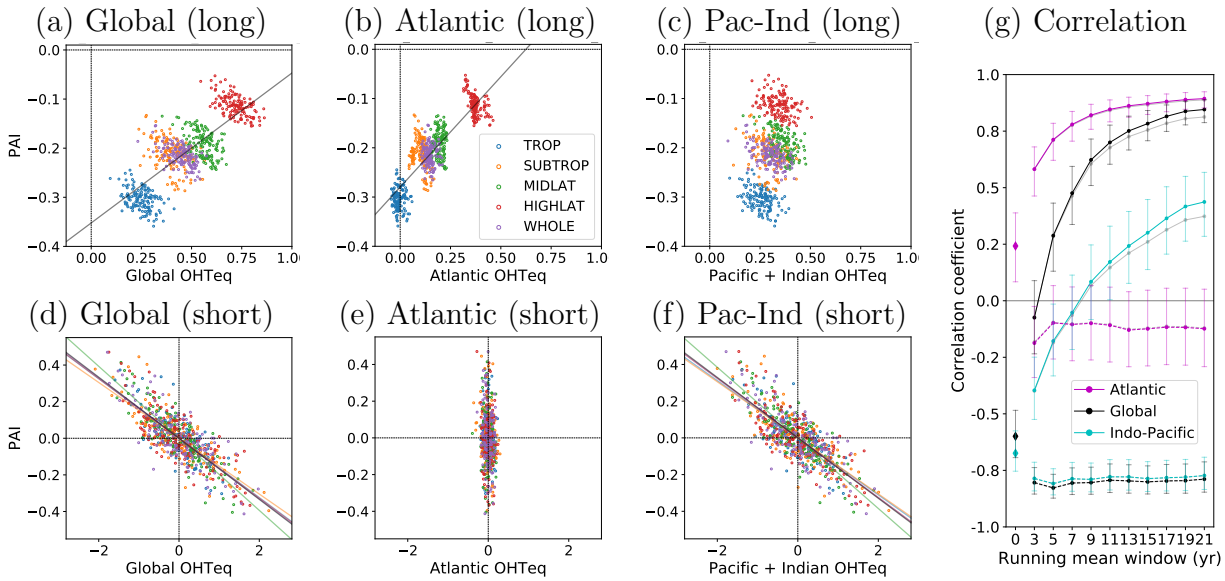

Figure 4.13: Identical to figure 4.11 except that $\mathrm{OHT}_{\mathrm{eq}}$) responses are normalized by their respective total heat transport responses. The grey lines in (g) show the correlation coefficients before normalization, which are identical to those in figure 4.11d.

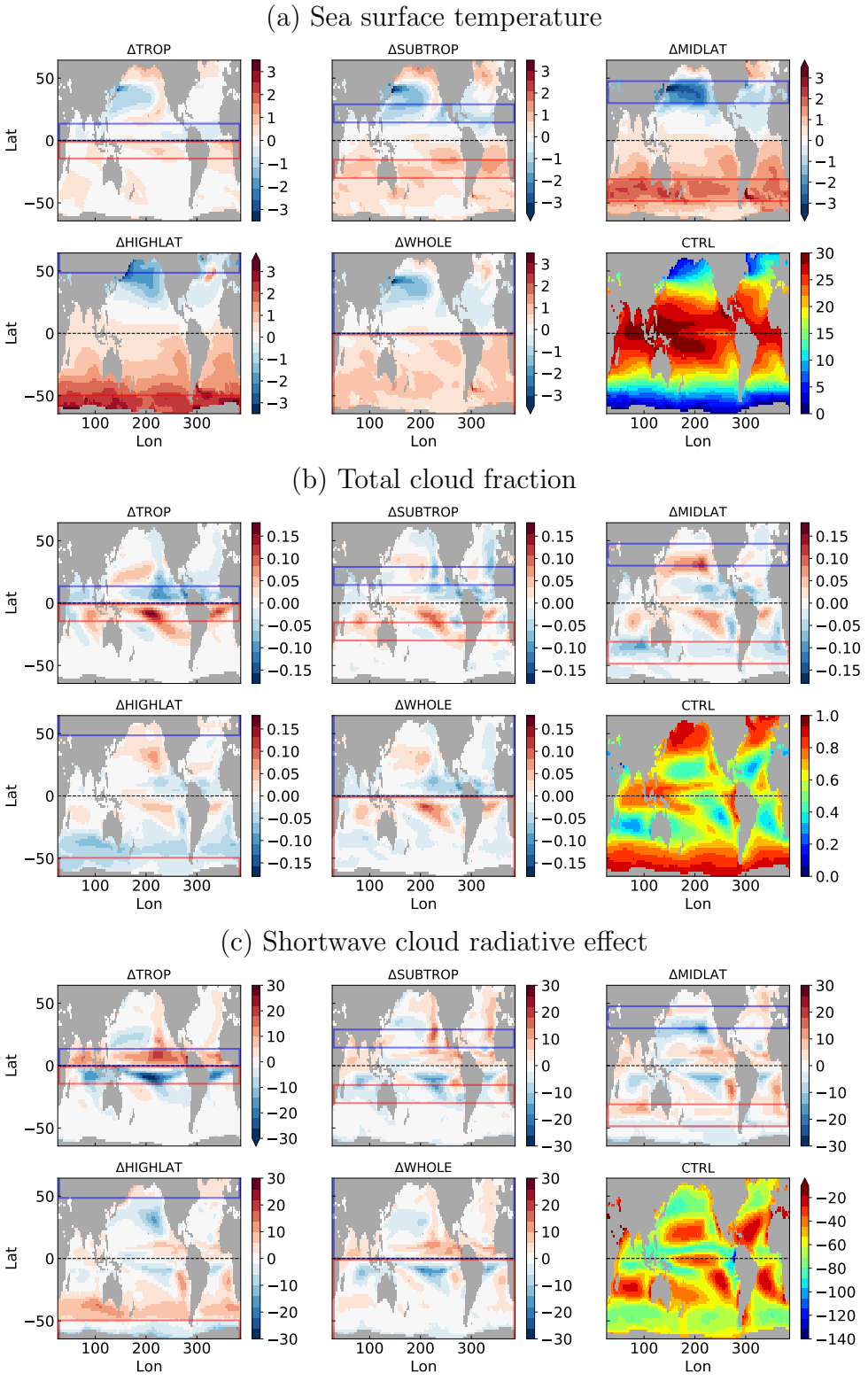

Figure 4.14: Annual-mean (a) surface temperature, (b) total cloud fraction, and (c) TOA shortwave cloud radiative effect responses (experiment minus control; except for CTRL) during years 51-200.

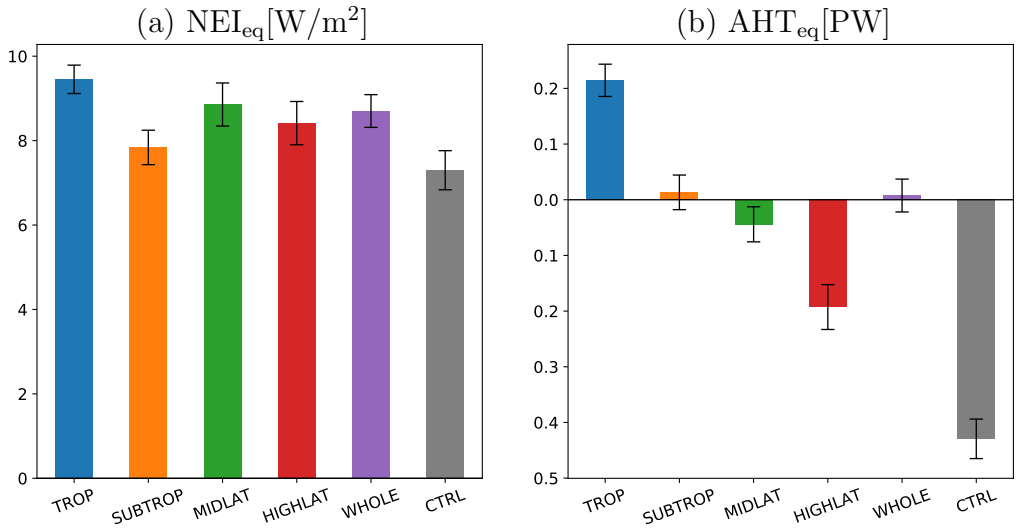

Figure 4.15: Annual-mean (a) NEI$_{eq}$and (b) AHT$_{eq}$. Errorbar is showing ± 1 standard deviation of 15-year running-averaged time-series. The averaging period is year 51–200.

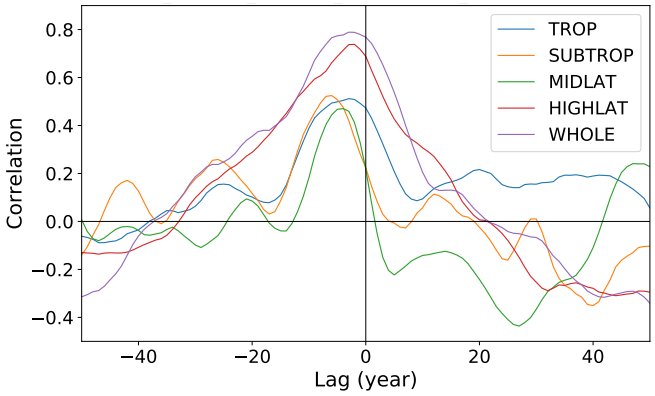

Figure 4.16: Cross correlation between time series of Labrador Sea upper ocean (0–200m) density and Atlantic meridional overturning circulation (AMOC) strength, smoothed with a 5-year running mean, with negative values indicating Labrador Sea density leading.

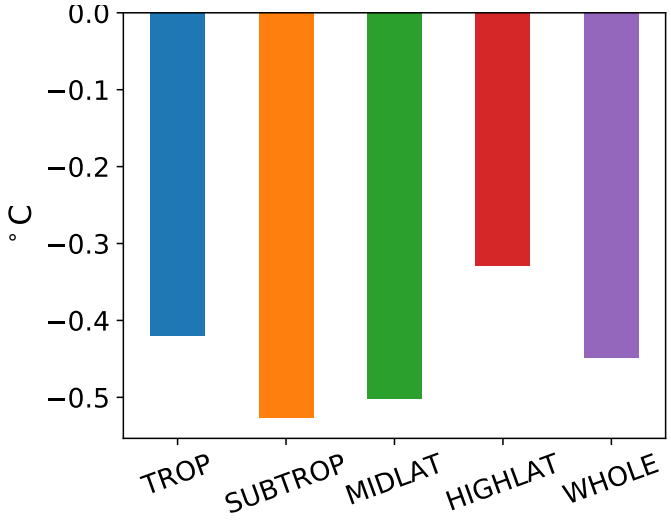

Figure 4.17: The hemispheric asymmetry of annual-mean tropical sea surface temperature (SST) near the equator calculated as the difference of mean SST [0°, 14.5°] minus mean SST [-14.5°, 0°] during years 51 to 200.

Chapter 5

Conclusion

The overarching motivation of this dissertation was to better understand the underlying physical processes of tropical precipitation biases in modern GCMs. While this dissertation is not a comprehensive study on tropical precipitation biases, novel methods uncovering new facets of tropical biases in modern GCMs were presented. Chapter 2 investigated the role of scale coupling frequency (or time step) in a superparameterized GCM. Chapter 3 employed a *short*, fully-coupled, hindcast experiments to examine the double ITCZ bias problems. Chapter 4 surveyed the sensitivity of tropical precipitation to the forcing location in a fully-coupled GCM with an explicit focus the AMOC as an oceanic buffering mechanism. The results presented in these chapters lay some important foundations for future modeling efforts and understanding of tropical precipitation. The lessons learned from this dissertation would inform the research community to better modeling and understanding. In the following concluding sections, these results are summarized, and suggestions for future research are offered.

5.1 Summary of Results

In Chapter 2, I examined the effect of the scale coupling frequency (or large-scale model time step) to simulated climatology in a superparameterized Community Atmospheric Model 3.0. There were a handful of interesting monotonic sensitivities: with a higher scale coupling frequency, (a) top-of-atmosphere cloud radiative forcing biases (both shortwave and longwave components) decrease, (b) the extreme tropical rainfall events become more frequent, (c) tropical deep convection becomes more bottom-heavy, and (d) topical temperature gradients becomes weaker. Interestingly, the time step sensitivities are not entirely consistent to a conventional GCM counterpart (e.g. opposite sensitivities in cloud forcing responses, but similar sensitivities in extreme precipitation). While the causes of the rest sensitivities (a–c) are still unclear, the first two sensitivities (a and b) can be explained by the convective organization sensitivity (c). The last sensitivity (d) can be explained by a dynamical adjustment that a local (sub-grid) energy build-up is removed by large-scale dynamics. The findings have some practical implications. For example, when one designs a model experiment, a superparameterized model time step can be used as an adjuster to modulate the vertical profile of deep convections and/or the weak temperature gradient conformity. For a model tuning strategy, a model time step may be utilized as a tuning knob for cloud forcing and/or tropical precipitation extremes.

In Chapter 3, I investigated the effect of explicit deep convection in the initial development of the double ITCZ bias in the superparameterized Community Earth System Model (CESM) 1.1. First, the fast bias evolution (e.g. a few days for precipitation and a few weeks for sea surface temperature) was shown to validate our novel experiment strategy of using short, ensemble hindcast simulations—as opposed to the traditional approach that focuses on equilibrium responses obtained from long simulations. Then, I showed the double ITCZ bias was weaker in the superparameterized simulations than in the non-superparameterized simulations, e.g. the cold tongue SST was warmer due to weaker easterlies and the ITCZ

precipitation maxima was close to the equator in the central Pacific. However, the bias reduction in SP simulations was based on a nonphysical reason: the lack of convective momentum transport in the superparameterized model caused insufficient mixing in the boundary layer. Such insufficient mixing caused surface wind stress to be weaker although the 850-hPa easterlies were stronger—which was caused by the enhanced zonal surface pressure gradient—in the superparaemterized simulation than in non-superparatmerized simulation. Such effect of convective momentum transport was also confirmed in a perturbed convective parameterization simulation by our collaborators at the University of Washington. Finally, one representative set of ensemble hindcast simulations was performed with the uncoupled (but still superparameterized) CESM 1.1, and its results showed similar low-level wind shear responses, indicating that the low-level wind shear was indeed coming from the atmospheric component of the coupled model. The finding demonstrated the importance of convective momentum transport in the double ITCZ bias development, which has received relatively less attention, and of the role of deep convection in setting a zonal pressure gradient along the equator.

In Chapter 4, using the dynamic ocean-coupled Community Earth System Model 1.2, I explored how the cross-equatorial energy transport partitions into atmospheric and oceanic components when a top-of-atmosphere solar forcing was present at different latitudinal bands. A specific focus was given to heat transport by AMOC since I initially hypothesized the oceanic heat transport response associate with AMOC would impact the partitioning more effectively than that associate with subtropical cells. The total heat transport responses were surprisingly insensitive to the solar forcing location as a result of compensating radiative feedbacks, but the partitioning responses clearly exhibited a monotonic sensitivity. The heat transport partitioning became more ocean-centric as forcing was located at higher latitudes, while the total (atmospheric plus oceanic) energy transport responses were rather similar regardless of forcing locations. Further examination revealed that the Pacific-Indian energy transport was insensitive, but the Atlantic energy transport was monotonically sensitive

to the forcing location, driving the partitioning sensitivity, e.g. Atlantic energy transport increased with a higher latitude forcing case. AMOC responses were monotonic—even when the forcing pairs were located away from the deep water forming regions. On the other hand, subtropical cells responded to the forcing, but the circulation strength and depth responses compensate each other, making the resulting heat transport rather insensitive to the forcing location. Finally, a correlation analysis using different time filters showed that the Atlantic heat transport was responsible for the long-term response of the ITCZ position (positively covarying between the ITCZ shift and the oceanic heat transport response) while Pacific-Indian heat transport was responsible for the short-term response of ITCZ position (negatively covarying). The opposite sign of correlation reveals the fundamental difference of ITCZ buffering mechanisms of two basins (i.e. whether mechanically coupled to the atmospheric circulation or not), and confirms our initial hypothesis about the efficacy of the buffering mechanisms. While these results demand the inclusion of AMOC in the current ITCZ energetic framework, one practical implication (from the ITCZ shift sensitivity to the solar forcing location) would be that fixing the tropical bias rather than the extratropical bias would be more effective to alleviate the double ITCZ bias in a coupled model. More generally, these results suggest that caution should be taken when interpreting the slab ocean based simulation results.

5.2 Future Research Suggestions

Future work suggestion for Chapter 2

The sensitivity of convective organization (i.e. the vertical structure of convective updraft) to a GCM time step was found to be a key to modulate other sensitivities (e.g. precipitation and cloud radiative effects) but the underlying physical causes are still left unknown. I pointed out the potential physical mechanism based on the long gravity wave's constraint on

a vertical updraft profile (*Kuang*, 2011), however testing the idea has not been conducted yet since a clear diagnostic way of testing was not obvious. A new set of experiments specifically targeting this problem will be a worthy task to further improve our understanding of the superparameterized model physics and tropical dynamics in general.

Future work suggestion for Chapter 3

While the convective momentum transport was found to be a potentially important process that leads to the double ITCZ bias, it is unclear if such convective momentum transport (CMT) mechanism exists in other models. Accordingly, an inter-model verification would be helpful to see if this is a common mechanism. Some preliminary analysis of Coupled Model Intercomparison Project phase 5 models is presented in Appendix B. Both coupled and uncoupled GCMs show too strong low-level zonal-wind shear in the central Pacific, suggesting the possibility that the CMT mechanism might be common across GCMs, however, the in-depth analysis will be necessary to further confirm if the common zonal-wind shear problem in different GCMs is associated with the CMT mechanism.

Future work suggestion for Chapter 4

The investigation of the mechanistic pathway of AMOC responses to the TOA forcing will be an important task to understand further about the ITCZ buffering mechanism by AMOC. Unlike high latitude forcing which may directly perturb the surface energy budget at the deep water formation sites, the linkage between low-latitude TOA forcing and AMOC response is less obvious. Another important potential work is investigating the relative insensitiveness of TOA radiative feedback to forcing location. Answering if this is an intrinsic feature of the current climate system would have an important implication not only in the ITCZ dynamics but also in climate sensitivity. Such studies will require a holistic approach because

of the many compensating radiative feedbacks in addition to feedbacks from the large-scale atmospheric and oceanic circulations (e.g. gyre circulation and low cloud interaction).

Bibliography

Adam, O., T. Schneider, F. Brient, and T. Bischoff (2016), Relation of the doubleITCZ bias to the atmospheric energy budget in climate models, *Geophys Res Lett*, doi:10.1002/2016GL069465.

Adam, O., T. Schneider, and F. Brient (2017), Regional and seasonal variations of the double-ITCZ bias in CMIP5 models, *Clim. Dyn.*, pp. 1–17, doi:10.1007/s00382-017-3909-1.

Adler, R., G. Huffman, and C. A. of (2003), The version-2 global precipitation climatology project (GPCP) monthly precipitation analysis (1979present), *Journal of* , doi:10.1175/1525-7541(2003)004⟨1147:TVGPCP⟩2.0.CO;2.

Allan, R. P., and B. J. Soden (2008), Atmospheric warming and the amplification of precipitation extremes, *Science*, *321*(5895), 1481–1484, doi:10.1126/science.1160787.

Allen, M. R., and W. J. Ingram (2002), Constraints on future changes in climate and the hydrologic cycle, *Nature*, *419*(6903), 224, doi:10.1038/nature01092.

Allen, R. J. (2015), A 21st century northward tropical precipitation shift caused by future anthropogenic aerosol reductions, *Journal of Geophysical Research: Atmospheres*, doi:10.1002/2015JD023623.

Bacmeister, J., M. Suarez, and F. R. Robertson (2006), Rain reevaporation, boundary layer-convection interactions, and pacific rainfall patterns in an AGCM, *Journal of the* , *63*, 3383–3403, doi:10.1175/JAS3791.1.

Bellucci, A., S. Gualdi, and A. Navarra (2010), The double-ITCZ syndrome in coupled general circulation models: the role of large-scale vertical circulation regimes, *Journal of Climate*, *23*(5), 1127–1145, doi:10.1175/2009JCLI3002.1.

Benedict, J. J., and D. A. Randall (2009), Structure of the Madden–Julian Oscillation in the Superparameterized CAM, *Journal of the Atmospheric Sciences*, *66*(11), 3277–3296.

Bischoff, T., and T. Schneider (2014), Energetic constraints on the position of the intertropical convergence zone, *Journal of Climate*, *27*(13), 4937–4951, doi:10.1175/JCLI-D-13-00650.1.

Boyer, T., J. Antonov, O. Baranova, H. Garcia, D. Johnson, R. Locarnini, A. Mishonov, O. TD, D. Seidov, I. Smolyar, M. Zweng, and L. E. S (2009), *World Ocean Database 2009*, vol. NOAA Atlas NESDIS 66, U.S. Gov. Printing Office.

Bretherton, C., and S. Park (2009), A new moist turbulence parameterization in the community atmosphere model, *Journal of Climate*, *22*, 3422–3449, doi:10.1175/2008JCLI2556.1.

Broccoli, A., K. Dahl, and R. Stouffer (2006), Response of the ITCZ to northern hemisphere cooling, *Geophys. Res. Lett.*, *33*, L01,702, doi:10.1029/2005GL024546.

Buckley, M., and J. Marshall (2016), Observations, inferences, and mechanisms of the atlantic meridional overturning circulation: A review, *Rev. Geophys.*, *54*, 5–63, doi:10.1002/2015RG000493.

Burls, N., and A. Fedorov (2014), What controls the mean eastwest sea surface temperature gradient in the equatorial pacific: The role of cloud albedo, *Journal of Climate*, doi:10.1175/JCLI-D-13-00255.1.

Carton, J., and B. Giese (2008), A reanalysis of ocean climate using simple ocean data assimilation (SODA), *Mon Weather Rev*, *136*(8), 2999–3017, doi:10.1175/2007MWR1978.1.

Ceppi, P., Y. Hwang, X. Liu, D. M. Frierson, and D. L. Hartmann (2013), The relationship between the ITCZ and the southern hemispheric eddydriven jet, *J Geophys Res Atmospheres*, *118*(11), 5136–5146, doi:10.1002/jgrd.50461.

Chang, P., R. Zhang, W. Hazeleger, C. Wen, X. Wan, L. Ji, R. J. Haarsma, W. Breugem, and H. Seidel (2008), Oceanic link between abrupt changes in the north atlantic ocean and the african monsoon, *Nature Geoscience*, *1*(7), 444–448, doi:10.1038/ngeo218.

Cheng, W., J. C. H. Chiang, and D. Zhang (2013), Atlantic meridional overturning circulation (AMOC) in CMIP5 models: RCP and historical simulations, *Journal of Climate*, *26*(18), 7187–7197, doi:10.1175/JCLI-D-12-00496.1.

Chiang, J., and A. Friedman (2012), Extratropical cooling, interhemispheric thermal gradients, and tropical climate change, *Annu. Rev. Earth Planet. Sci.*, *40*, 383–412, doi:10.1146/annurev-earth-042711-105545.

Chiang, J. C., and C. M. Bitz (2005), Influence of high latitude ice cover on the marine intertropical convergence zone, *Clim Dynam*, *25*(5), 477–496, doi:10.1007/s00382-005-0040-5.

Chiang, J. C., M. Biasutti, and D. S. Battisti (2003), Sensitivity of the atlantic intertropical convergence zone to last glacial maximum boundary conditions, *Paleoceanography*, *18*(4), doi:10.1029/2003PA000916.

Chikira, M. (2010), A cumulus parameterization with state-dependent entrainment rate. part II: impact on climatology in a general circulation model, *Journal of the Atmospheric Sciences*, doi:10.1175/2010JAS3317.1.

Cowan, T., and W. Cai (2013), The response of the largescale ocean circulation to 20th century asian and nonAsian aerosols, *Geophys Res Lett*, *40*(11), 2761–2767, doi:10.1002/grl.50587.

Cvijanovic, I., P. L. Langen, E. Kaas, and P. D. Ditlevsen (2013), Southward intertropical convergence zone shifts and implications for an atmospheric bipolar seesaw, *J Climate*, *26*(12), 4121–4137, doi:10.1175/JCLI-D-12-00279.1.

de Szoeke, S. P., Y. Wang, S. Xie, and T. Miyama (2006), Effect of shallow cumulus convection on the eastern pacific climate in a coupled model, *Geophysical Research Letters*, *33*(17), L17,713, doi:10.1029/2006GL026715.

Dee, D., S. Uppala, A. Simmons, P. Berrisford, P. Poli, S. Kobayashi, U. Andrae, M. Balmaseda, G. Balsamo, P. Bauer, P. Bechtold, A. Beljaars, L. van de Berg, J. Bidlot, N. Bormann, C. Delsol, R. Dragani, M. Fuentes, A. Geer, L. Haimberger, S. Healy, H. Hersbach, E. Hólm, L. Isaksen, P. Kållberg, M. Köhler, M. Matricardi, M. AP, M. BM, J. Morcrette, B. Park, C. Peubey, P. de Rosnay, C. Tavolato, J. Thépaut, and F. Vitart (2011), The ERAInterim reanalysis: configuration and performance of the data assimilation system, *Q J Roy Meteor Soc*, *137*(656), 553–597, doi:10.1002/qj.828.

Delworth, T. L., and K. W. Dixon (2006), Have anthropogenic aerosols delayed a greenhouse gas-induced weakening of the north atlantic thermohaline circulation?, *Geophys. Res. Lett.*, *33*(2), doi:10.1029/2005GL024980.

Ding, Y., J. A. Carton, G. A. Chepurin, G. Stenchikov, A. Robock, L. T. Sentman, and J. P. Krasting (2014), Ocean response to volcanic eruptions in coupled model intercomparison project 5 simulations, *J. Geophys. Res. Ocean*, *119*(9), 5622–5637, doi:10.1002/2013JC009780.

Donohoe, A., J. Marshall, and D. Ferreira (2013), The relationship between ITCZ location and cross-equatorial atmospheric heat transport: From the seasonal cycle to the last glacial maximum, *Journal of Climate*.

Drijfhout, S. S. (2010), The atmospheric response to a thermohaline circulation collapse: Scaling relations for the hadley circulation and the response in a coupled climate model, *J Climate*, *23*(3), 757–774, doi:10.1175/2009JCLI3159.1.

Dunstone, N., D. Smith, B. Booth, L. Hermanson, and R. Eade (2013), Anthropogenic aerosol forcing of atlantic tropical storms, *Nat Geosci*, *6*(7), 534–539, doi:10.1038/ngeo1854.

Fedorov, A. V., N. J. Burls, K. T. Lawrence, and L. C. Peterson (2015), Tightly linked zonal and meridional sea surface temperature gradients over the past five million years, *Nature Geoscience*, *8*, 975–980, doi:10.1038/ngeo2577.

Frierson, D. M., and Y. Hwang (2012), Extratropical influence on ITCZ shifts in slab ocean simulations of global warming, *Journal of Climate*, *25*(2), 720–733, doi:10.1175/JCLI-D-11-00116.1.

Frierson, D. M. W., Y. Hwang, N. S. Fukar, R. Seager, S. M. Kang, A. Donohoe, E. E. Maroon, X. Liu, and D. S. Battisti (2013), Contribution of ocean overturning circulation to tropical rainfall peak in the northern hemisphere, *Nat. Geosci*, *6*, doi:10.1038/ngeo1987.

Fučkar, N. S., S. Xie, R. Farneti, E. A. Maroon, and D. M. Frierson (2013), Influence of the extratropical ocean circulation on the intertropical convergence zone in an idealized coupled general circulation model, *J. Climate*, *26*(13), 4612–4629, doi:10.1175/JCLI-D-12-00294.1.

Giese, B., and S. Ray (2011), El niño variability in simple ocean data assimilation (SODA), 18712008, *Journal of Geophysical Research: Oceans*, *116*, C02,024, doi:10.1029/2010JC006695.

Goswami, B. B., N. J. Mani, P. Mukhopadhyay, D. E. Waliser, J. J. Benedict, E. D. Maloney, M. Khairoutdinov, and B. N. Goswami (2011), Monsoon intraseasonal oscillations as simulated by the superparameterized Community Atmosphere Model, *Journal of Geophysical Research*, *116*(D22).

Grabowski, W. W. (2001), Coupling cloud processes with the large-scale dynamics using the cloud-resolving convection parameterization (CRCP), *Journal of the Atmospheric Sciences*, *58*(9), 978–997.

Grabowski, W. W., and P. K. Smolarkiewicz (1999), CRCP: A cloud resolving convection parameterization for modeling the tropical convecting atmosphere, *Physica D: Nonlinear Phenomena*, *133*, 171–178.

Green, B., and J. Marshall (2017), Coupling of trade winds with ocean circulation damps ITCZ shifts, *J Climate*, doi:10.1175/JCLI-D-16-0818.1.

Gregory, J., K. Dixon, R. Stouffer, A. Weaver, E. Driesschaert, M. Eby, T. Fichefet, H. Hasumi, A. Hu, J. Jungclaus, I. Kamenkovich, A. Levermann, M. Montoya, S. Murakami, S. Nawrath, A. Oka, A. Sokolov, and R. Thorpe (2005), A model intercomparison of changes in the atlantic thermohaline circulation in response to increasing atmospheric CO2 concentration, *Geophys. Res. Lett.*, *32*(12), L12,703, doi:10.1029/2005GL023209.

Guilyardi, E., P. Braconnot, F. Jin, S. Kim, M. Kolansinski, T. Li, and I. Musat (2009), Atmosphere feedbacks during ENSO in a coupled GCM with a modified atmospheric convection scheme, *J. Clim.*, *22*, 5698–5718, doi:10.1175/2009JCLI2815.1.

Hawcroft, M., J. Haywood, M. Collins, and A. Jones (2016), Southern ocean albedo, interhemispheric energy transports and the double ITCZ: global impacts of biases in a coupled model, *Climate Dynamics*, doi:10.1007/s00382-016-3205-5.

Hawcroft, M., J. M. Haywood, M. Collins, and A. Jones (2018), The contrasting climate response to tropical and extratropical energy perturbations, *Climate Dynamics*, doi:10.1007/s00382-018-4076-8.

Haywood, J. M., A. Jones, N. Dunstone, S. Milton, M. Vellinga, A. Salcedo, M. Hawcroft, B. Kravitz, J. Cole, and S. Watanabe (2016), The impact of equilibrating hemispheric albedos on tropical performance in the HadGEM2 ES coupled climate model, *Geophys. Res. Lett.*, *43*(1), 395–403, doi:10.1002/2015GL066903.

Held, I. (2001), The partitioning of the poleward energy transport between the tropical ocean and atmosphere, *Journal of the atmospheric sciences*, doi:10.1175/1520-0469(2001)058⟨0943:TPOTPE⟩2.0.CO;2.

Held, I. M., and B. J. Soden (2006), Robust responses of the hydrological cycle to global warming, *J Climate*, *19*(21), 5686–5699, doi:10.1175/JCLI3990.1.

Hill, S. A., Y. Ming, and I. M. Held (2015), Mechanisms of forced tropical meridional energy flux change, *J. Clim.*, *28*(5), 1725–1742, doi:10.1175/JCLI-D-14-00165.1.

Hirota, N., Y. N. Takayabu, M. Watanabe, and M. Kimoto (2011), Precipitation reproducibility over tropical oceans and its relationship to the double ITCZ problem in CMIP3 and MIROC5 climate models, *J Climate*, *24*(18), 4859–4873, doi:10.1175/2011JCLI4156.1.

Huffman, G., R. Adler, D. Bolvin, and G. Gu (2009), Improving the global precipitation record: GPCP version 2.1, *Geophysical Research Letters*, doi:10.1029/2009GL040000.

Huffman, G. J., R. F. Adler, M. M. Morrissey, D. T. Bolvin, S. Curtis, R. Joyce, B. McGavock, and J. Susskind (2001), Global precipitation at one-degree daily resolution from multisatellite observations, *Journal of Hydrometeorology*, *2*(1), 36–50.

Huffman, G. J., D. T. Bolvin, E. J. Nelkin, D. B. Wolff, R. F. Adler, G. Gu, Y. Hong, K. P. Bowman, and E. F. Stocker (2007), The TRMM Multisatellite Precipitation Analysis (TMPA): Quasi-Global, Multiyear, Combined-Sensor Precipitation Estimates at Fine Scales, *Journal of Hydrometeorology*, *8*(1), 38–55.

Hurrell, J. W., J. J. Hack, D. Shea, J. M. Caron, and J. Rosinski (2008), A New Sea Surface Temperature and Sea Ice Boundary Dataset for the Community Atmosphere Model, *Journal of Climate*, *21*(19), 5145–5153.

Hurrell, J. W., M. Holland, P. Gent, S. Ghan, J. E. Kay, P. Kushner, J. Lamarque, W. Large, D. Lawrence, K. Lindsay, W. Lipscomb, M. Long, N. Mahowald, D. Marsh, R. Neale, P. Rasch, S. Vavrus, M. Vertenstein, D. Bader, W. Collins, J. Hack, J. Kiehl, and S. Marshall (2013), The community earth system model: A framework for collaborative research, *Bulletin of the American Meteorological Society*, *94*(9), 1339–1360, doi:10.1175/BAMS-D-12-00121.1.

Hwang, Y., and D. Frierson (2013), Link between the double-Intertropical convergence zone problem and cloud biases over the southern ocean, *Proceedings of the National Academy of Sciences*, *10*(13), 4935–4940, doi:10.1073/pnas.1213302110.

Hwang, Y., D. Frierson, and S. Kang (2013), Anthropogenic sulfate aerosol and the southward shift of tropical precipitation in the late 20th century, *Geophysical Research Letter*, doi:10.1002/grl.50502.

Hwang, Y., S. Xie, C. Deser, and S. M. Kang (2017), Connecting tropical climate change with southern ocean heat uptake, *Geophysical Research Letters*, doi:10.1002/2017GL074972.

Iles, C., and G. Hegerl (2014), The global precipitation response to volcanic eruptions in the CMIP5 models, *Environmental Research Letters*, *9*, 104,012 (10pp).

IPCC (2013), *Climate Change 2013: The Physical Science Basis. Contribution of Working Group I to the Fifth Assessment Report of the Intergovernmental Panel on Climate Change*, 1535 pp., Cambridge University Press, Cambridge, United Kingdom and New York, NY, USA, doi:10.1017/CBO9781107415324.

JP, M., and P. Lu (1994), Interaction between the subtropical and equatorial ocean circulations: The subtropical cell, *Journal of Physical Oceanography*, *24*, 466–497, doi:10.1175/1520-0485(1994)024⟨0466\:IBTSAE⟩2.0.CO.

Kang, S., I. Held, D. Frierson, and M. Zhao (2008), The response of the ITCZ to extratropical thermal forcing: Idealized slab-ocean experiments with a GCM, *Journal of Climate*.

Kang, S. M., D. M. Frierson, and I. M. Held (2009), The tropical response to extratropical thermal forcing in an idealized GCM: the importance of radiative feedbacks and convective parameterization, *Journal of the atmospheric* , *66*(9), 2812–2827, doi:10.1175/2009JAS2924.1.

Kang, S. M., B. Kim, D. M. Frierson, S. Jeong, J. Seo, and Y. Chae (2015), Seasonal dependence of the effect of arctic greening on tropical precipitation, *J Climate*, *28*(15), 6086–6095, doi:10.1175/JCLI-D-15-0079.1.

Kang, S. M., Y. Shin, and S. Xie (2018), Extratropical forcing and tropical rainfall distribution: energetics framework and ocean ekman advection, *npj Climate and Atmospheric Science*, *1*(1), doi:10.1038/s41612-017-0004-6.

Kay, J. E., C. Wall, V. Yettella, B. Medeiros, C. Hannay, P. Caldwell, and C. Bitz (2016), Global climate impacts of fixing the southern ocean shortwave radiation bias in the community earth system model (CESM), *Journal of Climate*, *29*(12), 4617–4636, doi:10.1175/JCLI-D-15-0358.1.

Khairoutdinov, M., and D. Randall (2001), A cloud resolving model as a cloud parameterization in the NCAR community climate system model: Preliminary results, *Geophysical Research Letters*, *28*(18), 3617–3620, doi:10.1029/2001GL013552.

Khairoutdinov, M., D. Randall, and C. DeMott (2005), Simulations of the atmospheric general circulation using a cloud-resolving model as a superparameterization of physical processes, *Journal of the Atmospheric Sciences*, pp. 2136–2154.

Khairoutdinov, M., C. DeMott, and D. Randall (2008), Evaluation of the Simulated Interannual and Subseasonal Variability in an AMIP-Style Simulation Using the CSU Multiscale Modeling Framework, *Journal of Climate*, *21*(3), 413–431.

Khairoutdinov, M. F., and D. A. Randall (2003), Cloud resolving modeling of the ARM summer 1997 IOP: Model formulation, results, uncertainties, and sensitivities, *Journal of the Atmospheric Sciences*, *60*, 607–624.

Kooperman, G., M. Pritchard, and M. Burt (2016), Robust effects of cloud superparameterization on simulated daily rainfall intensity statistics across multiple versions of the community earth system model, *Journal of Advances* .

Kuang, Z. (2011), The wavelength dependence of the gross moist stability and the scale selection in the instability of Column-Integrated moist static energy, *J Atmos Sci*, *68*(1), 61–74, doi:10.1175/2010JAS3591.1.

Large, W., and G. Danabasoglu (2006), Attribution and impacts of upper-ocean biases in CCSM3, *Journal of Climate*, *19*, 2325–2346, doi:10.1175/JCLI3740.1.

Large, W., and S. Yeager (2009), The global climatology of an interannually varying airsea flux data set, *Climate dynamics*, *33*, 341–364.

Li, C., L. Wu, and S. Xie (2013), Impacts of interhemispheric asymmetric thermal forcing on tropical pacific climate: Surface Air-Sea coupling and subduction, *J. Clim.*, *26*(2), 575–582, doi:10.1175/JCLI-D-11-00743.1.

Li, F., W. D. Collins, W. M. F, D. L. Williamson, J. G. Olson, and C. Algieri (2011), Impact of horizontal resolution on simulation of precipitation extremes in an aqua-planet version of community atmospheric model (CAM3), *Tellus A*, *63*(5), 884892, doi:10.1111/j.1600-0870.2011.00544.x.

Li, G., and S. Xie (2014), Tropical biases in CMIP5 multimodel ensemble: The excessive equatorial pacific cold tongue and double ITCZ problems*, *Journal of Climate*.

Li, G., Y. Du, H. Xu, and B. Ren (2015), An intermodel approach to identify the source of excessive equatorial pacific cold tongue in CMIP5 models and uncertainty in observational datasets, *Journal of Climate*, *28*(19), 7630–7640, doi:10.1175/JCLI-D-15-0168.1.

Lin, J. (2007), The Double-ITCZ problem in IPCC AR4 coupled GCMs: OceanAtmosphere feedback analysis, *Journal of Climate*, *20*(18), 4497–4525, doi:10.1175/JCLI4272.1.

Lin, Y., M. Zhao, Y. Ming, J. Golaz, L. J. Donner, S. A. Klein, V. Ramaswamy, and S. Xie (2013), Precipitation partitioning, tropical clouds, and intraseasonal variability in GFDL AM2, *J Climate*, p. 130206114111004, doi:10.1175/JCLI-D-12-00442.1.

Lindzen, R. S., and S. Nigam (1987), On the role of sea surface temperature gradients in forcing Low-Level winds and convergence in the tropics, *J Atmos Sci*, *44*(17), 2418–2436, doi:10.1175/1520-0469(1987)044⟨2418:OTROSS⟩2.0.CO;2.

Liu, C., and R. P. Allan (2012), Multisatellite observed responses of precipitation and its extremes to interannual climate variability, *Journal of Geophysical Research*, *117*(D3), D03,101.

Liu, H., M. Zhang, and W. Lin (2012), An investigation of the initial development of the double-ITCZ warm SST biases in the CCSM, *Journal of Climate*, *25*(1), 140–155.

Liu, Z., and S. G. H. Philander (1995), How different wind stress patterns affect the tropical-subtropical circulations of the upper ocean, *Journal of Physical Oceanography*, doi:10.1175/1520-0485(1995)025⟨0449:HDWSPA⟩2.0.CO;2.

Loeb, N. G., B. A. Wielicki, D. R. Doelling, G. L. Smith, D. F. Keyes, S. Kato, N. Manalo-Smith, and T. Wong (2009), Toward optimal closure of the earth's top-of-atmosphere radiation budget, *Journal of Climate*, *22*(3), 748–766.

Ma, C., C. Mechoso, A. Robertson, and A. Arakawa (1996), Peruvian stratus clouds and the tropical pacific circulation: A coupled ocean-atmosphere GCM study, *J. Clim.*, *9*, 1635–1645.

Manabe, S., and R. Stouffer (1995), Simulation of abrupt climate change induced by freshwater input to the north atlantic ocean, *Nature*, *378*.

Marshall, J., A. Donohoe, D. Ferreira, and M. D (2014), The ocean's role in setting the mean position of the Inter-Tropical convergence zone, *Climate Dynamics*, doi:10.1007/s00382-013-1767-z.

McFarlane, A., and D. W. Frierson (2017), The role of ocean fluxes and radiative forcings in determining tropical rainfall shifts in RCP8.5 simulations, *Geophysical Research Letters*, doi:10.1002/2017GL074473.

Mechoso, C., A. Robertson, N. Barth, M. Davey, P. Delecluse, P. Gent, S. Ineson, B. Kirtman, M. Latif, L. H. Treut, T. Nagai, J. Neelin, S. Philander, J. Polcher, P. Schopf, T. Stockdale, M. Suarez, L. Terray, O. Thual, and J. Tribbia (1995), The seasonal cycle over the tropical pacific in coupled OceanAtmosphere general circulation models, *Mon Weather Rev*, *123*(9), 2825–2838, doi:10.1175/1520-0493(1995)123⟨2825:TSCOTT⟩2.0.CO;2.

Mechoso, C., T. Losada, S. Koseki, M. Elsa, N. Keenlyside, C. Antonio, T. Myers, R. Belen, and T. Toniazzo (2016), Can reducing the incoming energy flux over the southern ocean in a CGCM improve its simulation of tropical climate?, *Geophys Res Lett*, *43*(20), doi:10.1002/2016GL071150.

Medhaug, I., and T. Furevik (2011), North atlantic 20th century multidecadal variability in coupled climate models: sea surface temperature and ocean overturning circulation, *Ocean Sci.*, *7*(3), 389–404, doi:10.5194/os-7-389-2011.

Menary, M., C. Roberts, M. Palmer, P. Halloran, L. Jackson, R. Wood, W. Muller, D. Matei, and S. Lee (2013), Mechanisms of aerosolforced AMOC variability in a state of the art climate model, *Journal of* , *118*, 2087–2096, doi:10.1002/jgrc.20178.

Merlis, T. M., M. Zhao, and I. M. Held (2013), The sensitivity of hurricane frequency to ITCZ changes and radiatively forced warming in aquaplanet simulations, *Geophys Res Lett*, *40*(15), 4109–4114, doi:10.1002/grl.50680.

Mishra, S. K., and S. Sahany (2011a), Effects of time step size on the simulation of tropical climate in NCAR-CAM3, *Climate Dynamics*, *37*(3-4), 689–704, doi:10.1007/s00382-011-0994-4.

Mishra, S. K., and S. Sahany (2011b), Effects of time step size on the simulation of tropical climate in NCAR-CAM3, *Climate Dynamics*, *37*(3-4), 689–704.

Mishra, S. K., J. Srinivasan, and R. S. Nanjundiah (2008a), The impact of the time step on the intensity of ITCZ in an aquaplanet GCM, *Monthly Weather Review*, *136*(11), 40774091, doi:10.1175/2008MWR2478.1.

Mishra, S. K., J. Srinivasan, and R. S. Nanjundiah (2008b), The Impact of the Time Step on the Intensity of ITCZ in an Aquaplanet GCM, *Monthly Weather Review*, *136*(11), 4077–4091.

Mitchell, T. P., and J. M. Wallace (1992), The annual cycle in equatorial convection and sea surface temperature, *Journal of Climate*, *5*(10), 1140–1156, doi:10.1175/1520-0442(1992)005⟨1140:TACIEC⟩2.0.CO;2.

Miyama, T., M. Julian, T. Jensen, J. Loschnigg, S. Godfrey, and A. Ishida (2003), Structure and dynamics of the Indian-Ocean cross-equatorial cell, *Deep Sea Res Part Ii Top Stud Oceanogr*, *50*(12-13), 2023–2047, doi:10.1016/S0967-0645(03)00044-4.

Möbis, B., and B. Stevens (2012), Factors controlling the position of the intertropical convergence zone on an aquaplanet, *Journal of Advances in Modeling Earth* , doi:10.1029/2012MS000199.

Morrison, H., J. Curry, and V. Khvorostyanov (2005), A new double-moment microphysics parameterization for application in cloud and climate models. part i: Description, *Journal of the Atmospheric Sciences*, *62*, 1665–1677, doi:10.1175/JAS3446.1.

MP, M., J. Sanjay, B. Booth, K. Kumar, and R. Betts (2012), The influence of vegetation on the ITCZ and south asian monsoon in HadCM3, *Earth Syst Dynam*, *3*, 87–96.

Muir, L., and A. Fedorov (2015), How the AMOC affects ocean temperatures on decadal to centennial timescales: the north atlantic versus an interhemispheric seesaw, *Clim Dynam*, *45*(1-2), 151–160, doi:10.1007/s00382-014-2443-7.

Neale, R., J. Richter, and M. Jochum (2008), The impact of convection on ENSO: from a delayed oscillator to a series of events, *Journal of Climate*, *21*, 5904–5924, doi:10.1175/2008JCLI2244.1.

Neelin, D. J., I. M. Held, and K. H. Cook (1987), Evaporation-Wind feedback and Low-Frequency variability in the tropical atmosphere, *J Atmos Sci*, *44*(16), 2341–2348, doi:10.1175/1520-0469(1987)044⟨2341:EWFALF⟩2.0.CO;2.

O'Gorman, P. A., R. P. Allan, M. P. Byrne, and M. Previdi (2012), Energetic constraints on precipitation under climate change, *Surveys in Geophysics*, *33*(3-4), 585–608, doi:10.1007/s10712-011-9159-6.

Oort, A. H. (1971), The observed annual cycle in the meridional transport of atmospheric energy, *J. Atmospheric Sci.*, pp. 325–339, doi:10.1175/1520-0469(1971)028⟨0325:TOACIT⟩2.0.CO;2.

Oueslati, B., and G. Bellon (2013), Tropical precipitation regimes and mechanisms of regime transitions: Contrasting two aquaplanet general circulation models, *Climate dynamics*, doi:10.1007/s00382-012-1344-x.

Oueslati, B., and G. Bellon (2015), The double ITCZ bias in CMIP5 models: interaction between SST, large-scale circulation and precipitation, *Climate Dynamics*, doi:10.1007/s00382-015-2468-6.

Park, S., and C. Bretherton (2009), The university of washington shallow convection and moist turbulence schemes and their impact on climate simulations with the community atmosphere model, *Journal of Climate*, *22*, 3449–3469, doi:10.1175/2008JCLI2557.1.

Pendergrass, A. G., and D. L. Hartmann (2014a), Changes in the distribution of rain frequency and intensity in response to global warming, *Journal of Climate*, *27*(22), 83728383, doi:10.1175/JCLI-D-14-00183.s1.

Pendergrass, A. G., and D. L. Hartmann (2014b), Changes in the Distribution of Rain Frequency and Intensity in Response to Global Warming, *Journal of Climate*, *27*(22), 8372–8383.

Pendergrass, A. G., and D. L. Hartmann (2014c), Two Modes of Change of the Distribution of Rain, *Journal of Climate*, *27*(22), 8357–8371.

Pritchard, M. S., M. W. Moncrieff, and R. C. J. Somerville (2011), Orogenic Propagating Precipitation Systems over the United States in a Global Climate Model with Embedded Explicit Convection, *Journal of the Atmospheric Sciences*, *68*(8), 1821–1840.

Pritchard, M. S., C. S. Bretherton, and C. A. DeMott (2014), Restricting 32–128 km horizontal scales hardly affects the MJO in the Superparameterized Community Atmosphere Model v. 3.0 but the number of cloudresolving grid columns constrains vertical mixing, *Journal of Advances in Modeling Earth Systems*, *6*(3), 723–739.

Qian, T., A. Dai, and K. Trenberth (2006), Simulation of global land surface conditions from 1948 to 2004. part i: Forcing data and evaluations, *Journal of* , doi:10.1175/JHM540.1.

Raymond, D. J., S. L. Sessions, A. H. Sobel, and Ž. Fuchs (2009), The Mechanics of Gross Moist Stability, *Journal of Advances in Modeling Earth Systems*, *1*(3).

Richter, J., and P. Rasch (2008), Effects of convective momentum transport on the atmospheric circulation in the community atmosphere model, version 3, *Journal of Climate*, *21*(7), 1487–1499, doi:10.1175/2007JCLI1789.1.

Roberts, W. G., P. Valdes, and J. Singarayer (2016), Can energy fluxes be used to interpret glacial/interglacial precipitation changes in the tropics?, *Geophys. Res. Lett.*, *44*, 63736382, doi:10.1002/2017GL073103.

Rossow, W. B., A. Mekonnen, C. Pearl, and W. Goncalves (2013), Tropical Precipitation Extremes, *Journal of Climate*, *26*(4), 1457–1466.

Rotstayn, L., M. Collier, and J. Luo (2015), Effects of declining aerosols on projections of zonally averaged tropical precipitation, *Environmental Research* , *10*, 044,018, doi: 10.1088/1748-9326/10/4/044018.

Schneider, T. (2017), Feedback of AtmosphereOcean coupling on shifts of the intertropical convergence zone, *Geophysical Research Letters*, doi:10.1002/2017GL075817.

Schneider, T., T. Bischoff, and G. Haug (2014), Migrations and dynamics of the intertropical convergence zone, *Nature*, doi:10.1038/nature13636.

Seo, J., S. Kang, and D. Frierson (2014), Sensitivity of intertropical convergence zone movement to the latitudinal position of thermal forcing, *J Climate*, *27*(8), 3035–3042, doi: 10.1175/JCLI-D-13-00691.1.

Seo, J., S. Kang, and T. Merlis (2017), A model intercomparison of the tropical precipitation response to a CO2 doubling in aquaplanet simulations, *Geophysical Research Letters*, pp. 993–1000, doi:10.1002/2016GL072347.

Sobel, A. H., J. Nilsson, and L. M. Polvani (2001), The Weak Temperature Gradient Approximation and Balanced Tropical Moisture Waves, *Journal of the Atmospheric Sciences*, *58*(23), 3650–3665.

Song, S., and B. Mapes (2012), Interpretations of systematic errors in the NCEP climate forecast system at lead times of 2, 4, 8, ..., 256 days, *J. Adv. Model. Earth Syst.*, *4*(3), n/a–n/a, doi:10.1029/2011MS000094.

Song, X., and G. Zhang (2009), Convection parameterization, tropical pacific double ITCZ, and upper-ocean biases in the NCAR CCSM3. part i: Climatology and atmospheric feedback, *Journal of Climate*.

Stan, C., M. Khairoutdinov, C. A. DeMott, V. Krishnamurthy, D. M. Straus, D. A. Randall, J. L. Kinter, and J. Shukla (2010), An ocean-atmosphere climate simulation with an embedded cloud resolving model, *Geophys Res Lett*, *37*(1), L01,702, doi: 10.1029/2009GL040822.

Stevens, B., J. Duan, J. McWilliams, M. Münnich, and J. Neelin (2002), Entrainment, rayleigh friction, and boundary layer winds over the tropical pacific, *Journal of Climate*, *15*(1), 30–44.

Swann, A. L., I. Y. Fung, and J. C. Chiang (2012), Mid-latitude afforestation shifts general circulation and tropical precipitation, *Proc. Natl. Acad. Sci.*, *109*(3), 712–716, doi:10.1073/pnas.1116706108.

Tan, M., A. Ibrahim, Z. Duan, A. Cracknell, and V. Chaplot (2015), Evaluation of Six High-Resolution Satellite and Ground-Based Precipitation Products over Malaysia, *Remote Sensing*, *7*(2), 1504–1528.

Taylor, K., R. Stouffer, and G. Meehl (2012), An overview of CMIP5 and the experiment design, *Bulletin of the American* , *93*(4), 485–498, doi:10.1175/BAMS-D-11-00094.1.

Thayer-Calder, K., and D. A. Randall (2009), The Role of Convective Moistening in the Madden–Julian Oscillation, *Journal of the Atmospheric Sciences*, *66*(11), 3297–3312.

Thomas, M., and A. Fedorov (2017), The eastern subtropical pacific origin of the equatorial cold bias in climate models: A lagrangian perspective, *Journal of Climate*, *30*, 5885–5900, doi:10.1175/JCLI-D-16-0819.1.

Tomas, R. A., C. Deser, and L. Sun (2016), The role of ocean heat transport in the global climate response to projected arctic sea ice loss, *Journal of Climate*, *29*(19), 6841–6859, doi:10.1175/JCLI-D-15-0651.1.

Trenberth, K. E., and D. P. Stepaniak (2003), Covariability of components of poleward atmospheric energy transports on seasonal and interannual timescales, *J. Clim.*, *16*(22), 3691–3705, doi:10.1175/1520-0442(2003)016⟨3691:COCOPA⟩2.0.CO;2.

Tseng, Y., H. Lin, H. Chen, K. Thompson, M. Bentsen, C. Böning, A. Bozec, C. Cassou, E. Chassignet, C. Chow, G. Modelling, S. Danilov, R. Farneti, P. Fogli, Y. Fujii, S. Griffies, M. Ilicak, T. Jung, S. Masina, A. Navarra, L. Patara, B. Samuels, M. Scheinert, D. Sidorenko, C. Sui, H. Tsujino, S. Valcke, A. Voldoire, Q. Wang, and S. Yeager (2016), North and equatorial pacific ocean circulation in the CORE-II hindcast simulations, *Ocean Modelling*, *104*, 143–170.

Tulich, S. N. (2015), A strategy for representing the effects of convective momentum transport in multiscale models: Evaluation using a new superparameterized version of the Weather Research and Forecast model (SP-WRF), *Journal of Advances in Modeling Earth Systems*, *7*(2), 938–962.

Vannière, B., E. Guilyardi, T. Toniazzo, G. Madec, and S. Woolnough (2014), A systematic approach to identify the sources of tropical SST errors in coupled models using the adjustment of initialised experiments, *Clim Dynam*, *43*(7-8), doi:10.1007/s00382-014-2051-6.

Vellinga, M., and R. Wood (2002), Global climatic impacts of a collapse of the atlantic thermohaline circulation, *Climatic change*, *54*, 251–267.

Waliser, D., and C. Gautier (1993), A satellite-derived climatology of the ITCZ, *Journal of Climate*, *6*(11), 216–2174.

Wang, C., W. Lee, Y. Chen, and H. Hsu (2015), Processes leading to double intertropical convergence zone bias in CESM1/CAM5, *Journal of Climate*.

Wang, M., S. Ghan, R. Easter, M. Ovchinnikov, X. Liu, E. Kassianov, Y. Qian, G. W. Jr., V. Larson, D. Schanen, M. Khairoutdinov, and H. Morrison (2011), The multi-scale aerosol-climate model PNNL-MMF: model description and evaluation, *Geoscientific Model Development*, *4*(1), 137–168, doi:10.5194/gmd-4-137-2011.

Wentz, F. J., L. Ricciardulli, K. Hilburn, and C. Mears (2007), How much more rain will global warming bring?, *Science*, *317*(5835), 233–235, doi:10.1126/science.1140746.

Wheeler, M., and G. N. Kiladis (1999), Convectively coupled equatorial waves: Analysis of clouds and temperature in the wavenumber-frequency domain, *Journal of the Atmospheric Sciences*, *56*(3), 374–399.

Williamson, D. L. (2008), Convergence of aqua-planet simulations with increasing resolution in the community atmospheric model, version 3, *Tellus Series a-Dynamic Meteorology and Oceanography*, *60*(5), 848–862, doi:10.1111/j.1600-0870.2008.00339.x.

Williamson, D. L. (2013), The effect of time steps and time-scales on parametrization suites, *Quarterly Journal of the Royal Meteorological Society*, *139*(671), 548560, doi:10.1002/qj.1992.

Williamson, D. L., and J. G. Olson (2003), Dependence of aqua-planet simulations on time step, *Quarterly Journal of the Royal Meteorological Society*, *129*(591), 2049–2064.

Woelfle, M., S. Yu, C. Bretherton, and M. Pritchard (2018), Sensitivity of coupled tropical pacific model biases to convective parameterization in CESM1, *J. Adv. Model. Earth. Syst.*, *10*(1), 126–144, doi:10.1002/2017MS001176.

Wolff, D. B., and B. L. Fisher (2009), Assessing the Relative Performance of Microwave-Based Satellite Rain-Rate Retrievals Using TRMM Ground Validation Data, *Journal of Applied Meteorology and Climatology*, *48*(6), 1069–1099.

Woodruff, S., S. Worley, S. Lubker, and J. Z. journal (2011), ICOADS release 2.5: extensions and enhancements to the surface marine meteorological archive, *International journal* , doi:10.1002/joc.2103.

Wu, X., X. Liang, and G. Zhang (2003), Seasonal migration of ITCZ precipitation across the equator: Why can't GCMs simulate it?, *Geophysical Research Letters*, *30*(15), doi:10.1029/2003GL017198.

Wyant, M. C., M. Khairoutdinov, and C. S. Bretherton (2006), Climate sensitivity and cloud response of a GCM with a superparameterization, *Geophysical Research Letters*, *33*(6), L06,714.

Xiang, B., M. Zhao, I. Held, and J. Golaz (2017), Predicting the severity of spurious 'double ITCZ'problem in CMIP5 coupled models from AMIP simulations, *Geophysical Research* , doi:10.1002/2016GL071992.

Yeager, S. (2015), Topographic coupling of the atlantic overturning and gyre circulations, *Journal of Physical Oceanography*, *45*, 1258–1284, doi:10.1175/JPO-D-14-0100.1.

Yeager, S., and G. Danabasoglu (2014), The origins of late-twentieth-century variations in the large-scale north atlantic circulation, *Journal of Climate*, *27*, 3222–3247.

Yoshimori, M., and A. Broccoli (2008), Equilibrium response of an atmospheremixed layer ocean model to different radiative forcing agents: Global and zonal mean response, *J. Clim.*

Yu, J., and C. Mechoso (1999), Links between annual variations of peruvian stratocumulus clouds and of SST in the eastern equatorial pacific, *Journal of Climate*, doi:10.1175/1520-0442(1999)012⟨3305:LBAVOP⟩2.0.CO;2.

Yu, S., and M. S. Pritchard (2015), The effect of largescale model time step and multiscale coupling frequency on cloud climatology, vertical structure, and rainfall extremes in a superparameterized GCM, *J. Adv. Model. Earth. Syst.*, doi:10.1002/2015MS000493.

Zermeño-Diaz, D. M., and C. Zhang (2013), Possible root causes of surface westerly biases over the equatorial atlantic in global climate models, *J. Clim.*, *26*(20), 8154–8168, doi:10.1175/JCLI-D-12-00226.1.

Zhang, G. (2002), Convective quasiequilibrium in midlatitude continental environment and its effect on convective parameterization, *Journal of Geophysical Research: Atmospheres*, *107*(D14), 4220, doi:10.1029/2001JD001005.

Zhang, G., and N. A. McFarlane (1995), Sensitivity of climate simulations to the parameterization of cumulus convection in the canadian climate centre general circulation model, *Atmosphere-ocean*, *33*(3), 407–446, doi:10.1080/07055900.1995.9649539.

Zhang, L., and C. Wang (2013), Multidecadal north atlantic sea surface temperature and atlantic meridional overturning circulation variability in CMIP5 historical simulations, *J. Geophys. Res.: Oceans*, *118*, 5772–5791, doi:10.1002/jgrc.20390.

Zhang, R., and T. Delworth (2005), Simulated tropical response to a substantial weakening of the atlantic thermohaline circulation, *Journal of Climate*, doi:10.1175/JCLI3460.1.

Zhang, R., S. Kang, and I. Held (2010), Sensitivity of climate change induced by the weakening of the atlantic meridional overturning circulation to cloud feedback, *Journal of Climate*, *23*(2), 378–389, doi:10.1175/2009JCLI3118.1.

Zhang, X., F. W. Zwiers, G. C. Hegerl, H. F. Lambert, N. P. Gillett, S. Solomon, P. A. Stott, and T. Nozawa (2007a), Detection of human influence on twentieth-century precipitation trends, *Nature*, *448*(7152), 461, doi:10.1038/nature06025.

Zhang, X., W. Lin, and M. Zhang (2007b), Toward understanding the double intertropical convergence zone pathology in coupled oceanatmosphere general circulation models, *J. Geophys. Res.*, *112*(D12), doi:10.1029/2006JD007878.

Zhang, X., H. Liu, and M. Zhang (2015), Double ITCZ in coupled OceanAtmosphere models: From CMIP3 to CMIP5, *Geophysical Research Letters*, doi:10.1002/2015GL065973.

Zhu, J., A. Kumar, W. Wang, and H. Z. Geophysical (2017), Importance of convective parameterization in ENSO predictions, *Geophysical* , doi:10.1002/2017GL073669.

Zuidema, P., P. Chang, and M. B. of the (2016), Challenges and prospects for reducing coupled climate model SST biases in the eastern tropical atlantic and pacific oceans: The US CLIVAR eastern tropical , *Bulletin of the* , doi:10.1175/BAMS-D-15-00274.1.

Appendix A

Sensitivities of the double ITCZ / cold tongue bias to varying the orientation and extent of embedded cloud resolving models in the SuperParameterized CESM

Prior to the hindcast simulation shown in Chapter 3, a series of SPCESM sensitivity tests to an embedded cloud resolving model (CRM) configuration were performed as a pilot test. The objectives were to:

- test if superparameterization (SP) can improve the double-ITCZ bias;
- test if any sensitivities of the SP ITCZ are indicative of physics that produce a dITCZ in conventional GCMs; and
- select a most realistic CRM configuration for following hindmost simulations.

A.1 Experimental setup and methods

Model. The superparameterized Community Earth System Model 1.1 is used. The model setup is identical to SP-CESM setup in Section 3.2, except that the sensitivity simulations are initialized with climatological present-day conditions (CESM compset: B_2000). Refer to Section 3.2 for the details of the model.

Sensitivity simulations. The tested CRM configurations include the CRM orientation, domain size, resolution, and dimensionality. A whole set of sensitivity simulations are listed in table A.1. Each simulation is one-year long. After evaluating a whole set of the sensitivity simulations, the simulation with a most valid CRM configuration is extended two more years to assess if its 1-year results were affected by ENSO and if the double ITCZ bias further amplifies in the following years.

Table A.1: Sensitivity simulation list.

Experiment ID	CRM orientaion	CRM columns	CRM Δx
1	N–S	64×1	4km
2	N–S	32×1	4km
3	N–S	8×1	4km
4	E–W	64×1	4km
5	E–W	32×1	4km
6	E–W	8×1	4km
7	3-dimensional	8×8	4km
8	E–W	32×1	2km
9	E–W	32×1	1km
10	No superparameterization		

Internal variability. 90% confidence interval is harvested from a separate 7-year SP-CESM

simulation (figure A.1), to discriminate detectable zonal mean sensitivities for the analysis region above in our short 1-year sensitivity tests. The confidence interval is applied to all CRM sensitivity simulations, assuming the internal variability of the SP-CESM is not sensitive to the CRM configurations.

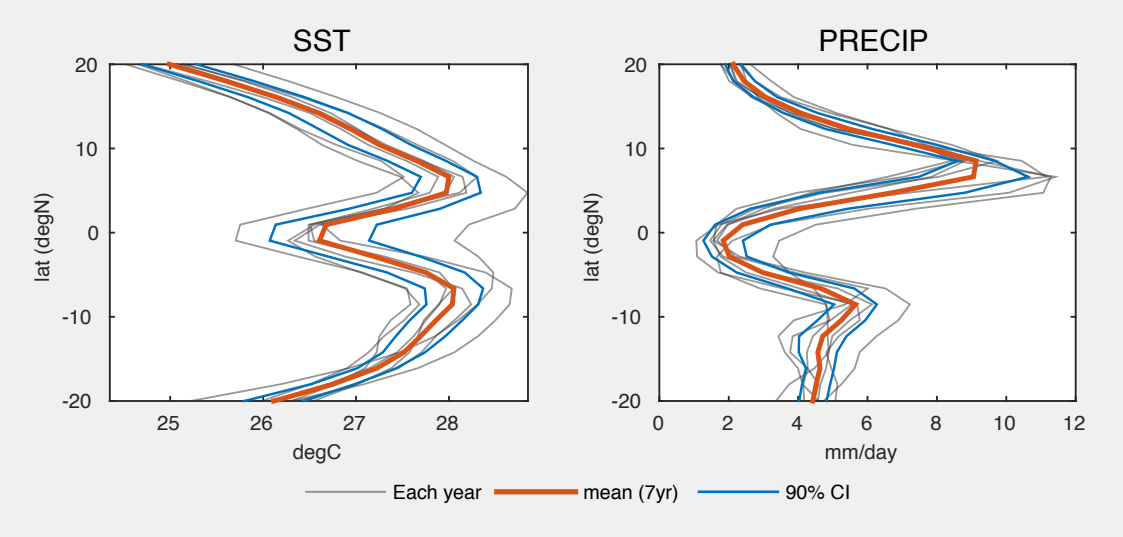

Figure A.1: Zonal-mean, annual-mean sea surface temperature (left) and precipitation (right) of a reference 7-year SP-CESM simulation. An annual mean of each year is shown in grey, an annual-mean of a full 7-year simulation is shown in red, and 90% confidence interval (estimated using t-statistic) is shown in blue.

A.2 Results

- Both annual-mean sea surface temperature (SST) and precipitation responses in the tropical Pacific are sensitive to the configuration of CRM (figure A.2) in the SP-CESM. The standard deviation across the SP-CESM runs with varying CRM configurations shows that the largest CRM sensitivity to the double ITCZ bias symptoms (e.g. the cold tongue SST and the artificial southern ITCZ band) is found in the central Pacific (figure A.3). Accordingly, further analysis focuses on the central Pacific (20°S–20°N, 170°E–240°E).

- The zonal-mean profiles of SST over the central Pacific show that certain CRM con-

figurations can reduce the degree of the double ITCZ bias (figure A.4a). In addition, a few monotonic sensitivities to the CRM configurations are found. First, the SP-CESM simulations with the north–south (N–S) CRM orientation produce a warmer cold tongue SST than that with east–west (E–W) CRM orientation (figure A.4a). The CRM orientation sensitivity is not affected by the CRM extent (or the number of columns) (figure A.4c). Second, the simulations with a larger CRM extent produce a warmer cold tongue SST that that with a smaller CRM extent (figure A.4b). However, the CRM extent sensitivity seems to exist only when the CRM extent is very small, e.g. the cold tongue SST responses are very similar between the SP simulations with 32x1 and 64x1 CRM extents. On the other hand, the CRM grid resolution does return a detectable sensitivity (not shown).

- Unlike the cold tongue SST responses, the effects of superparameterization is less detectable. Less precipitation occurs over the southern rainfall maxima around 10°S over the central Pacific in SP simulations (figure A.4d), but a time series of the area-mean precipitation rate over the southeastern equatorial Pacific (10°S–0°S, 210°E–270°E), where the spurious double ITCZ rain band appears, shows that the double ITCZ precipitation bias of SP-CESM still exists (figure A.5) and is as poor as the normal CESM (not shown).

- The double ITCZ bias develops fast and becomes noticeable within the first year of simulations in the SP-CESM, as found in other models (*Liu et al.*, 2012; *Song and Mapes*, 2012). For example, the precipitation bias structure of year 1 looks very similar to those of the following years (figure A.5).

A.3 Findings

- Superparameterization seems to improve the dITCZ bias in the CESM with certain CRM configurations (e.g. 2D 32×1 N–S CRM). The SST bias is less in the SP-CESM than the CESM, but the precipitation bias in the SP-CESM is comparable to that in the CESM.

- Both precipitation and SST biases show fast evolutions in SP-CESM. Short coupled simulations would be an efficient way to further understand and improve the double ITCZ bias in current climate models.

- Superparameterization is a new, useful tool to study the double ITCZ dynamics. New aspects of the double ITCZ can be revealed by further investigating the model dynamics underlying the double ITCZ bias sensitivity to CRM configurations and the SST bias improvement in the SP-CESM.

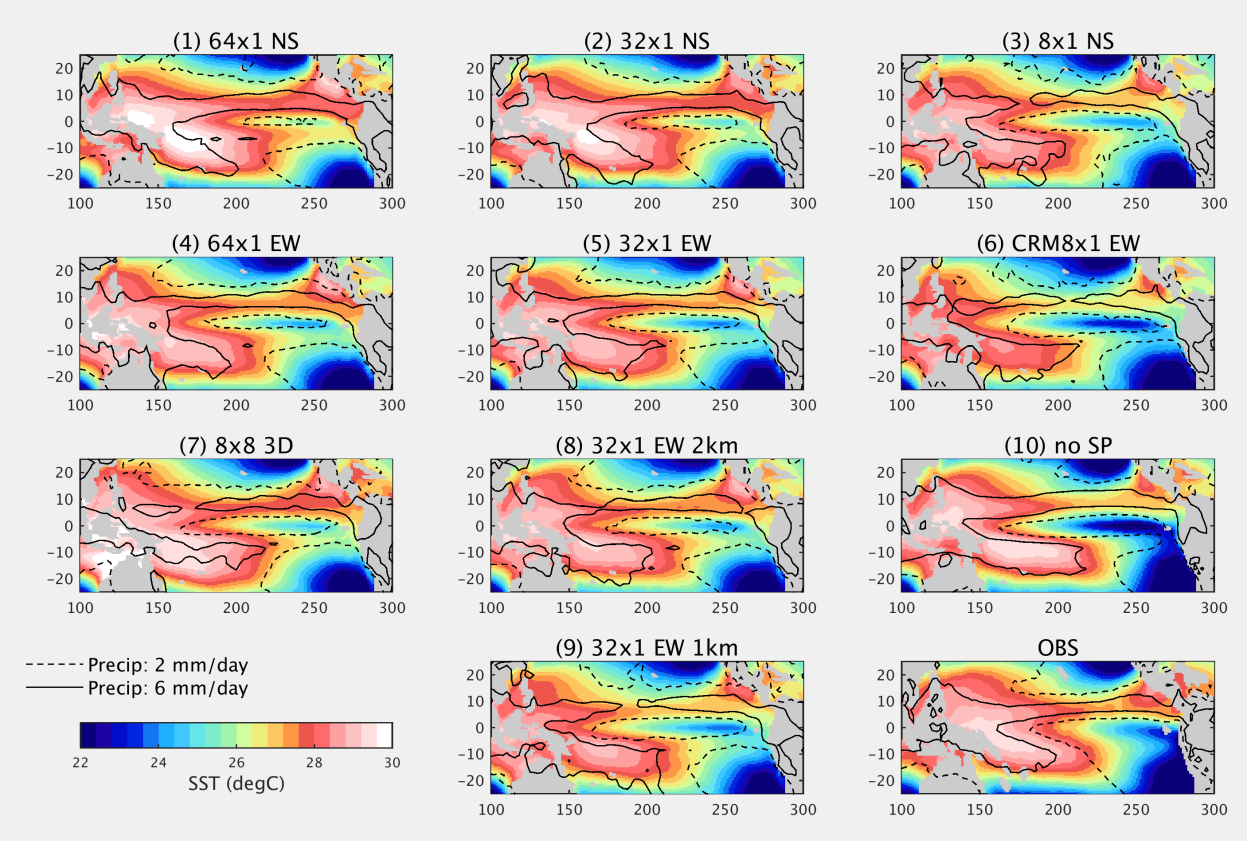

Figure A.2: Annual-mean sea surface temperature (shading) and precipitation (contour) of the first simulated year. Observation dataset is World Ocean Atlas 2009 for sea surface temperature (year 1955–2006) and TRMM 3B42 for precipitation (year 1998–2013).

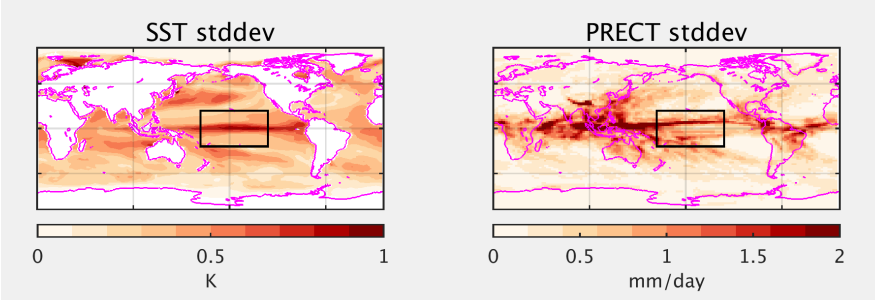

Figure A.3: Standard deviation of sea surface temperature (left) and precipitation (right). The black box shows the analysis region for figure A.4.

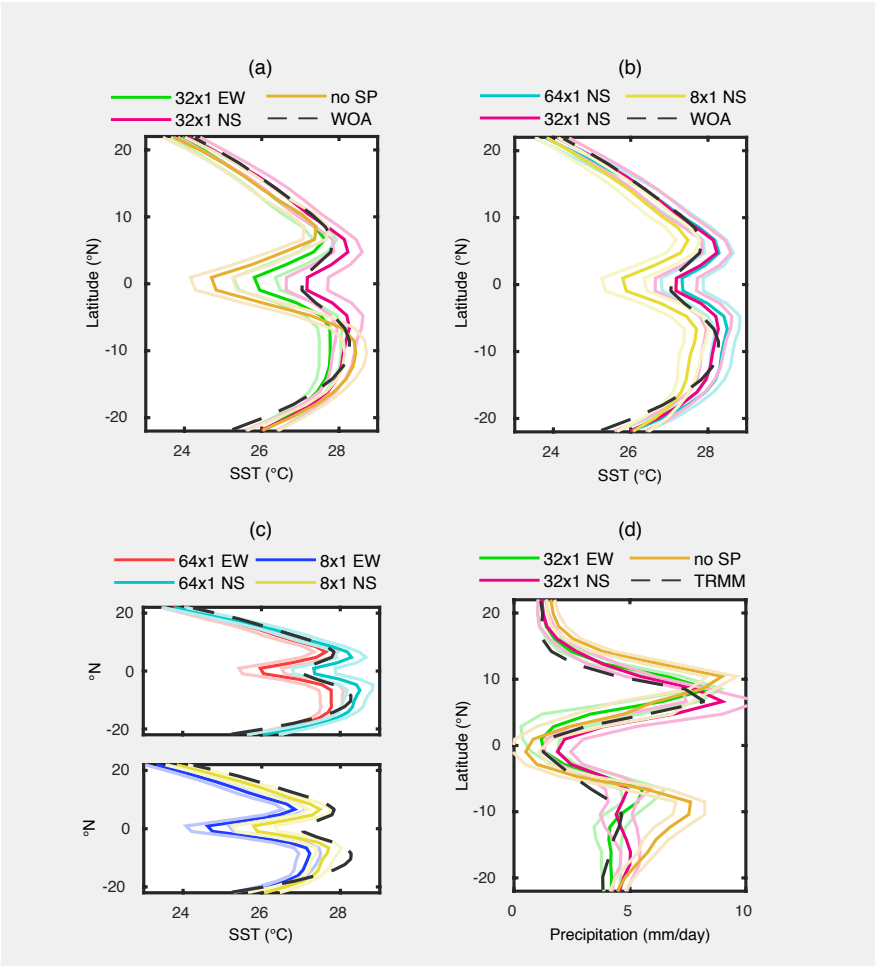

Figure A.4: Annual-mean, zonal-mean sea surface temperature (a, b, c) and precipitation (d). Dark colors are zonal mean, and light colors are 90% confidence interval (figure A.1). Refer to a legend of each figure for the plotted dataset.

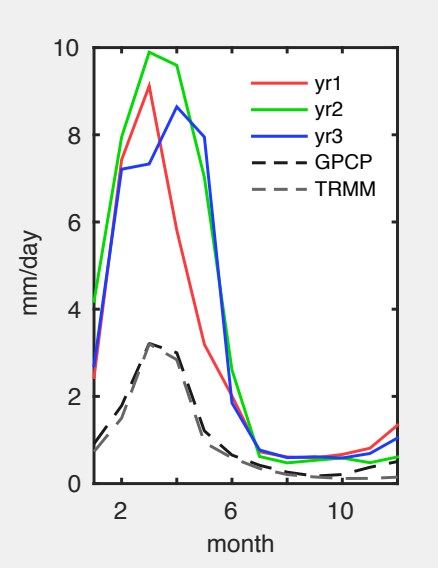

Figure A.5: A time series of central–south equatorial pacific precipitation [10°S–0°S, 210°E–270°E] of 3-year 32x1 NS simulation.

Appendix B

Central Pacific zonal wind profile analysis across CMIP5 models

Chapter 3 showed unrealistic zonal wind shear in the low level in the equatorial Central Pacific, regardless of convective parameterization used. While a stronger surface easterlies bias was predicted by an enhanced zonal surface pressure gradient, insufficient convective momentum transport (CMT) was identified as a factor controlling the zonal surface wind stress in Community Earth System Model (CESM) simulations. Here, a preliminary analysis is presented to see if the CMT mechanism is also present in other coupled global climate models (GCMs).

B.1 Method

The "historical" and "AMIP" simulations of GCMs participated in the Coupled Model Intercomparison Project phase 5 (CMIP5) (*Taylor et al.*, 2012) were downloaded from https://esgf-node.llnl.gov/projects/cmip5/. Only one ensemble member of each model was

downloaded. Some models participating in CMIP5 were omitted due to server errors. The models in this analysis are listed in table B.1.

The annual time average was taken from 1979 to 2005, the period that overlaps the reanalysis dataset (ERA-Interim; *Dee et al.* (2011)) used as observation. Then, all models were regridded both horizontally (2.8° longitude and latitude) and vertically (22 levels).

Table B.1: CMIP5 model used

Model	Modeling Institution
ACCESS1-0	Commonwealth Scientific and Industrial Research Organisation and Bureau of Meteorology
ACCESS1-3	”
bcc-csm1-1	Beijing Climate Center
bcc-csm1-1m	”
BNU-ESM	Beijing Normal University
CanCM4	Canadian Centre for Climate Modelling and Analysis
CanESM2	”
CCSM4	National Center for Atmospheric Research
CMCC-CESM	Centro Euro-Mediterraneo per I Cambiamenti Climatici
CMCC-CM	”
CMCC-CMS	”
CNRM-CM5	Centre National de Recherches Meteorologiques
CSIRO-Mk3-6-0	Commonwealth Scientific and Industrial Research Organisation and the Queensland Climate Change Centre of Excellence
FGOALS-g2	Chinese Academy of Sciences and Tsinghua University
GFDL-CM3	Geophysical Fluid Dynamics Laboratory
GFDL-ESM2G	”
GFDL-ESM2M	”

GISS-E2-H-CC	NASA Goddard Institute for Space Studies
GISS-E2-H	”
GISS-E2-R-CC	”
GISS-E2-R	”
HadCM3	Met Office Hadley Centre
HadGEM2-AO	”
HadGEM2-CC	”
HadGEM2-ES	”
inmcm4	Institute for Numerical Mathematics
IPSL-CM5A-LR	Institut Pierre-Simon Laplace
IPSL-CM5A-MR	”
IPSL-CM5B-LR	”
MIROC5	The University of Tokyo, National Institute for Environmental Studies, and Japan Agency for Marine-Earth Science and Technology
MIROC-ESM-CHEM	”
MIROC-ESM	”
MPI-ESM-LR	Max Planck Institute for Meteorology
MPI-ESM-MR	”
MRI-CGCM3	Meteorological Research Institute
MRI-ESM1	”
NorESM1-ME	Norwegian Climate Centre
NorESM1-M	”

B.2 Results

In this section, multi-model means (MMMs) are mainly analyzed for the sake of conciseness, assuming they are representing overall characteristics of the models participated in the CMIP5. Accordingly, one must consider the possibility that there are compensating multi-model errors or outlier models that are driving the MMM.

- Nearly all coupled CMIP5 GCMs show excessive low-level wind shear compared to ERA-Interim, implying that the erroneous CMT is possibly a common problem across different GCMs (figure B.1a). Similarly, atmospheric-only simulations (AMIP simulations) showing the same symptom of unrealistically too strong wind shear corroborate Chapter 3 results that showed the wind shear problem originates in the atmospheric model component (figure B.1b). However, the effect of ocean coupling is evident in the upper troposphere; the coupled simulations exhibit a much larger spread than the atmosphere-only simulations.

- The effects of ocean coupling on 850-hPa zonal wind and low-level wind shear vary across the models (figure B.2).

- The MMM zonal surface gradient of the coupled (atmosphere-only) models show weaker (stronger) east-west pressure difference than ERA-Interim (figure B.3a and figure B.4a). Such different zonal pressure gradients between coupled and atmosphere-only simulations seem responsible for the difference in the 850-hPa zonal wind (U850) over the Central Pacific, e.g. the atmosphere-only models have stronger easterlies than the coupled models (figure B.3b and figure B.4b).

- Although the MMM zonal surface wind stress (τ_x) of the atmosphere-only models (figure B.4c) is largely dictated by the MMM U850 (figure B.4b), the relationship between τ_x and U850 seems more complicated in the coupled models. For example,

the MMM U850 of the coupled models is more easterly than that of ERA-Interim over the Central and Eastern Pacific, but the MMM τ_x of the coupled models is less easterly than that of ERA-Interim (figure B.3b and figure B.3c).

- Unlike the relationship between the MMM and ERA-Interim (shown in the previous point), the relationship between U850 and τ_x across the models shows that they are better correlated in the coupled model than in the atmosphere-only models (figure B.5). The weak correlation in the coupled models and nearly zero correlation in the atmosphere-only models might be indicative of wrong atmospheric vertical mixing (which can be related to the CMT bias).

- Locally in the Central Pacific, the cold tongue index (as defined in Section 3.3.1) correlates slightly better with U850 than with τ_x (figure B.6). In addition, the cold tongue index correlates better with non-local (east of the CT-index region towards the ascending branch of the Walker circulation) U850 than local U850 (figure B.7). These correlations indicate the importance of non-local, large-scale contributors controlling the cold tongue bias.

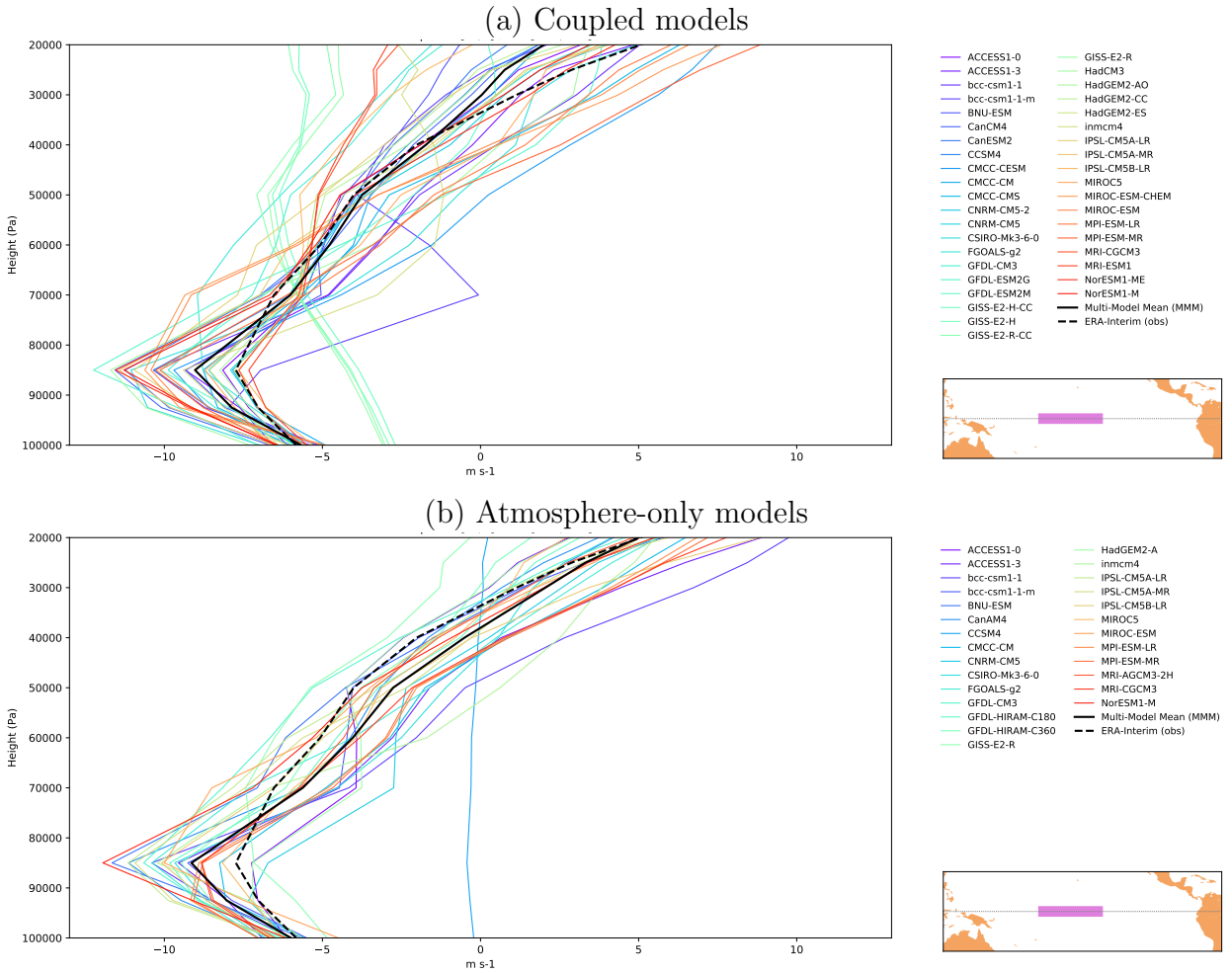

Figure B.1: Annual-mean zonal wind profile over the equatorial Central Pacific [180°E–180°E, 3°S–3°N] of (a) the coupled models and (b) the atmosphere-only models from CMIP5 historical simulation. Averaging period is 1979 to 2005.

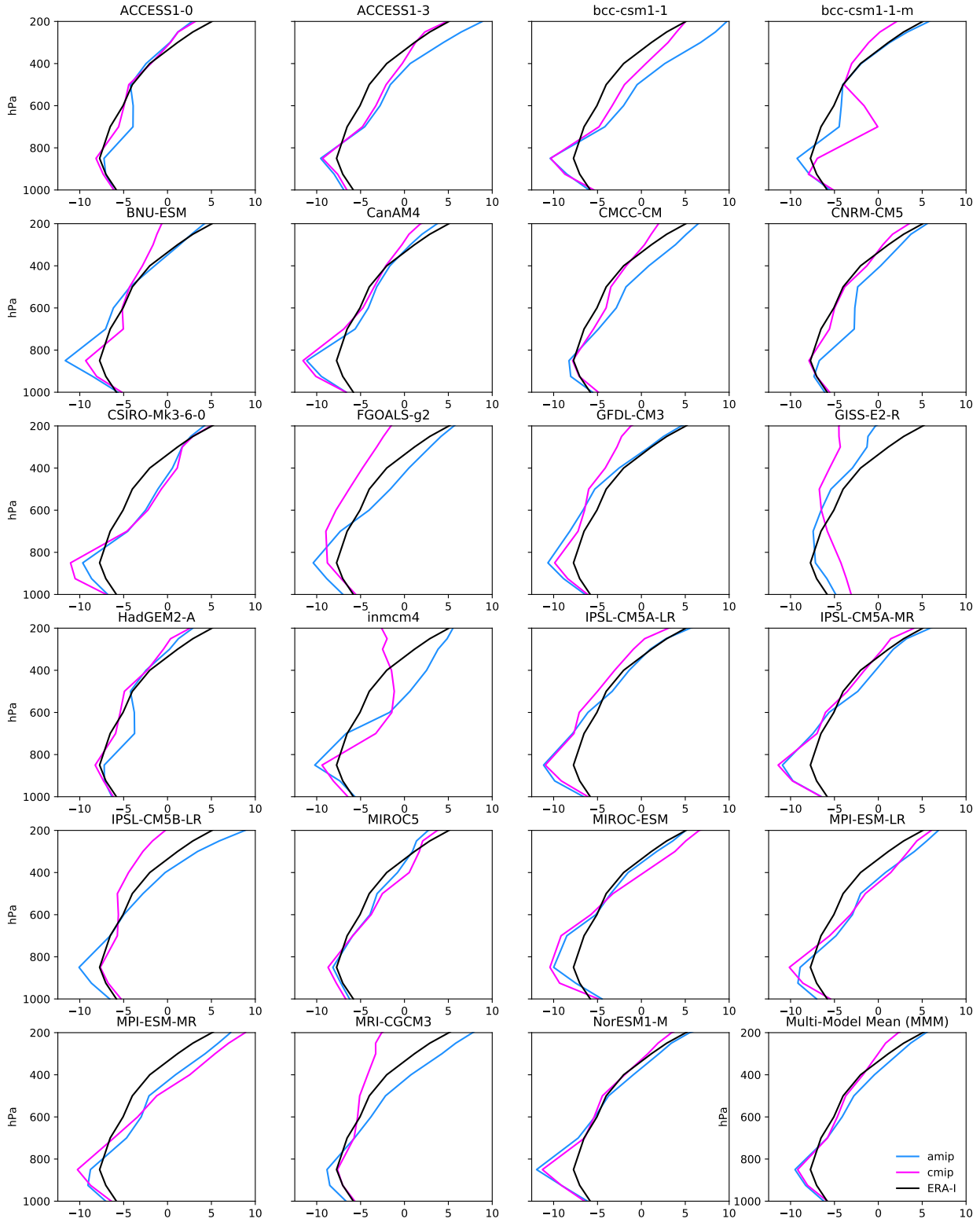

Figure B.2: Same as figure B.1, but the corresponding coupled and atmosphere-only simulations of each model are plotted separately. Only models that have both coupled ("historical") and atmosphere-only ("AMIP") simulations are plotted. The unit of abscissa is m/s.

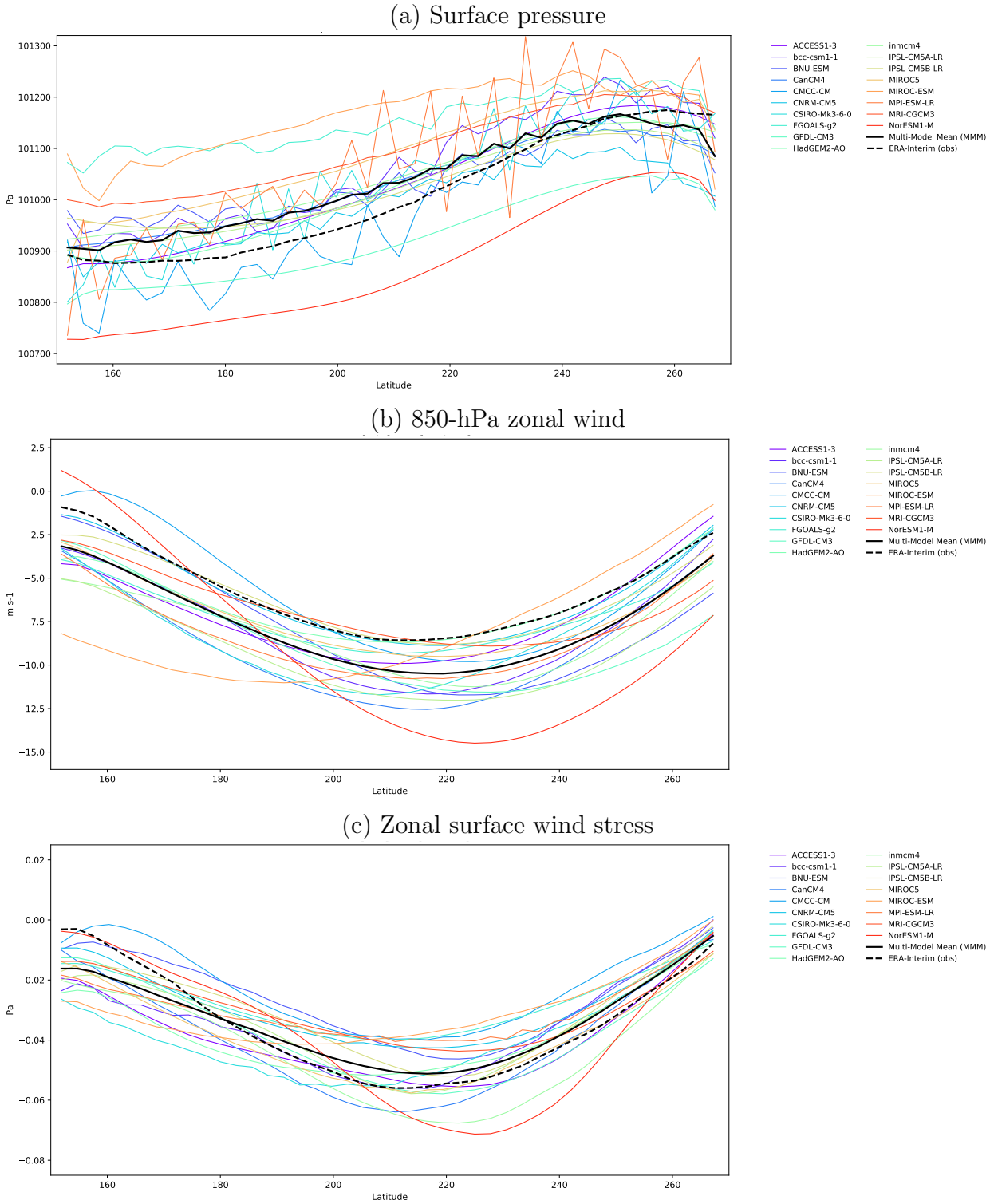

Figure B.3: Annual-mean equatorial Pacific [3°S–3°N] profiles of (a) surface pressure, (b) 850-hPa zonal wind, and (c) zonal surface wind stress of the coupled CMIP5 models. The models shown in this figures are a subset of the models shown in figure B.1a that has an atmosphere-only model counterpart. Averaging period is 1979 to 2005.

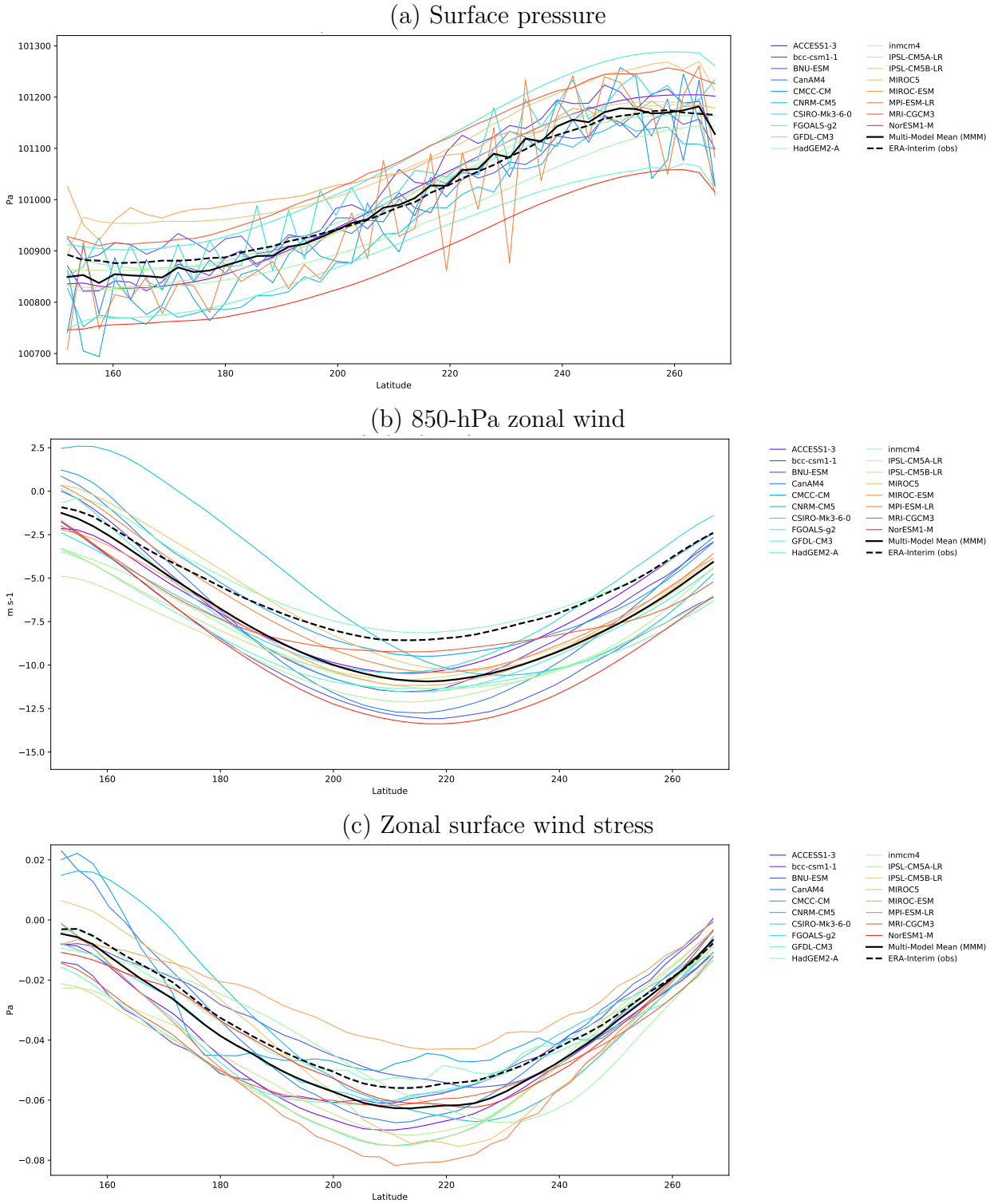

Figure B.4: Annual-mean equatorial Pacific [3°S–3°N] profiles of (a) surface pressure, (b) 850-hPa zonal wind, and (c) zonal surface wind stress of the atmosphere-only CMIP5 models. The models shown in this figures are a subset of the models shown in figure B.1b that has a coupled model counterpart. Averaging period is 1979 to 2005.

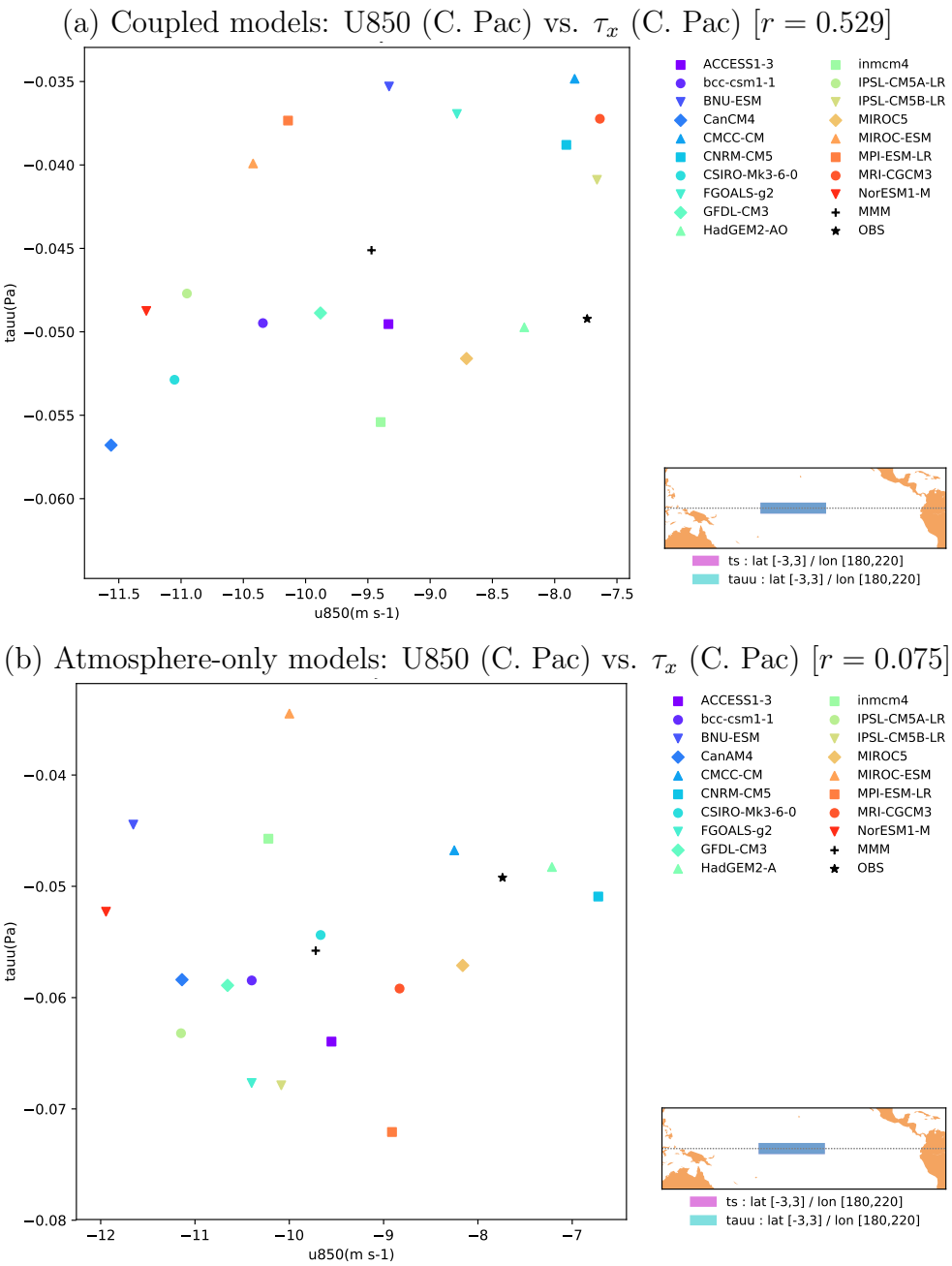

Figure B.5: Climatological annual-mean inter-model scatter plot over the Central Pacific [3°S–3°N, 180°E–220°E] between 850-hPa zonal wind and the cold-tongue index in (a) the coupled models and (b) the atmosphere-only models. The area-weighted averaging domain is showing in the map at the bottom right corner. Averaging period is 1979 to 2005. The Pearson correlation coefficient (r) is shown in the figure title.

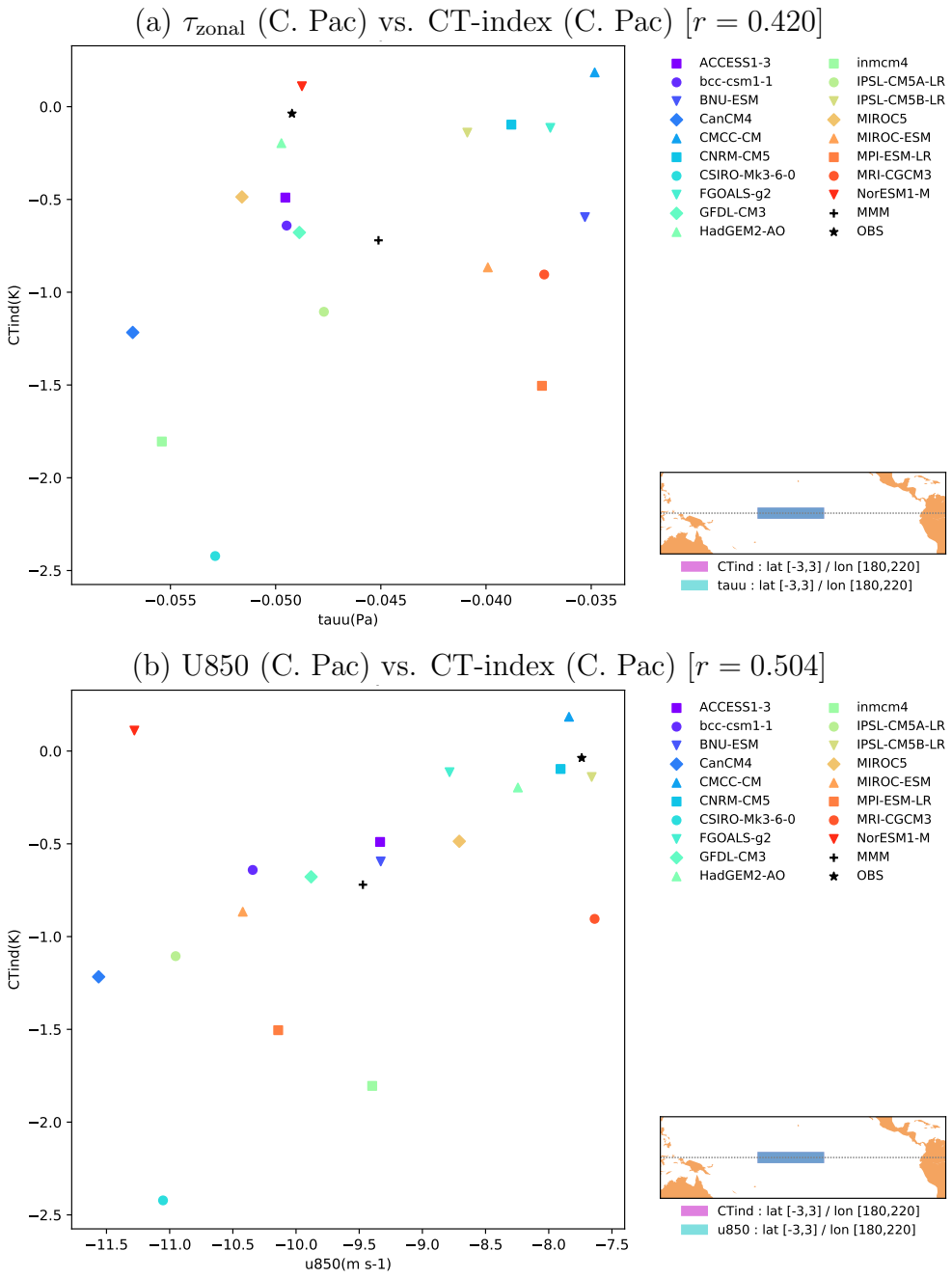

Figure B.6: Climatological annual-mean inter-model scatter plot over the Central Pacific [3°S–3°N, 180°E–220°E] between (a) zonal surface wind stress and the cold-tongue index and (b) 850-hPa zonal wind and the cold-tongue index in the coupled models. The area-weighted averaging domain is showing in the map at the bottom right corner. Averaging period is 1979 to 2005. The Pearson correlation coefficient (r) is shown in the figure title.

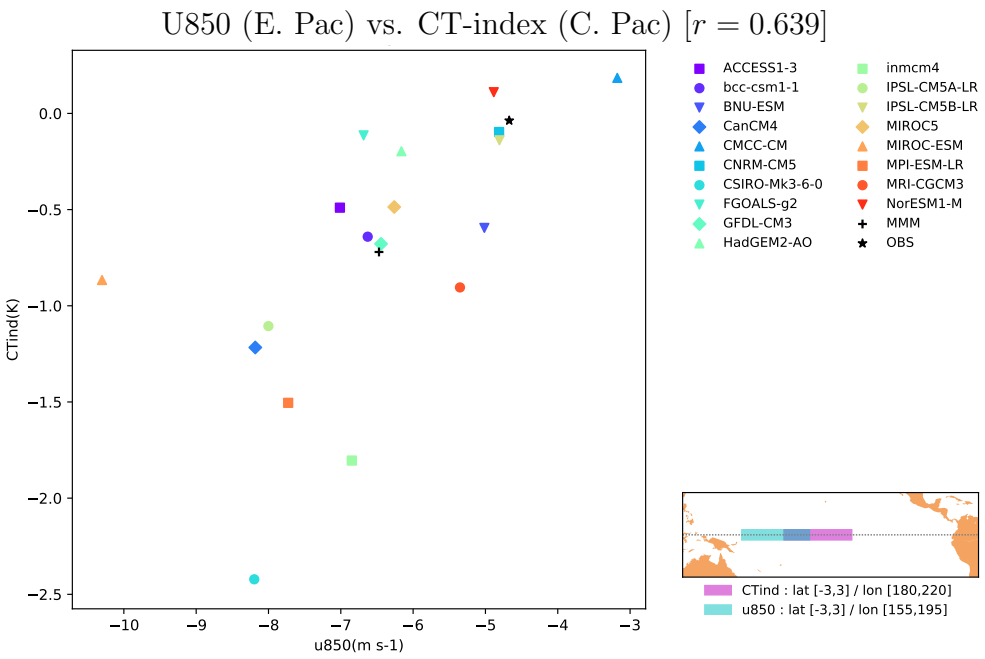

Figure B.7: Identical to figure B.6b, but the averaging domain for 850-hPa is shifted westward. The Pearson correlation coefficient (r) is shown in the figure title.